

Electronic structure calculations using dynamical mean field theory

K. HELD*

Max-Planck-Institut für Festkörperforschung, D-70569 Stuttgart, Germany

(Received 00 Month 200x; In final form 00 Month 200x)

The calculation of electronic properties of materials is an important task of solid state theory, albeit particularly difficult if electronic correlations are strong, for example in transition metals, their oxides and in f -electron systems. The standard approach to material calculations, the density functional theory in its local density approximation (LDA), incorporates electronic correlations only very rudimentarily and fails if the correlations are strong. Encouraged by the success of dynamical mean field theory (DMFT) in dealing with strongly correlated model Hamiltonians, physicists from the bandstructure and the many-body community have joined forces and developed a combined LDA+DMFT method recently. Depending on the strength of electronic correlations, this new approach yields a weakly correlated metal as in LDA, a strongly correlated metal, or a Mott insulator. By now, this approach is widely regarded as a breakthrough for electronic structure calculations of strongly correlated materials.

The author will review this LDA+DMFT method and also discuss alternative approaches to employ DMFT in electronic structure calculations, for example, by replacing the LDA part by the so-called GW approximation. Different methods to solve the DMFT equations are introduced with a focus on those that are suitable for realistic calculations with many orbitals. An overview of the successful application of LDA+DMFT to a wide variety of materials, ranging from Pu and Ce, to Fe and Ni, to numerous transition metal oxides, is given.

Contents

1	Introduction	2
2	Conventional electronic structure calculations	8
2.1	Ab initio Hamiltonian	8
2.2	Density functional theory (DFT)	8
2.3	Local density approximation (LDA)	10
3	Dynamical mean field theory (DMFT)	13
3.1	Derivation of the DMFT equations	15
3.2	Extensions of DMFT	21
4	Merging conventional bandstructure approaches with DMFT	25
4.1	LDA+DMFT	25
4.1.1	Hamiltonian formulation	25
4.1.2	Self-consistent LDA+DMFT calculations	29
4.1.3	Constrained LDA calculations of the interaction parameters	31
4.1.4	Spectral density functional theory formulation	36
4.1.5	Simplifications for transition metal oxides	40
4.2	Hartree+DMFT and Hartree-Fock+DMFT	41
4.3	GW+DMFT	44

* E-mail: k.held@fkf.mpg.de

5 DMFT solvers suitable for material calculations	49
5.1 Polarised Hartree-Fock (HF) approximation (LDA+U)	51
5.2 Hubbard-I, Hubbard-III and alloy-analogy approximation	54
5.3 Iterated perturbation theory (IPT) and extensions	57
5.4 Non-crossing approximation (NCA)	60
5.5 Quantum Monte Carlo (QMC) simulations	62
5.5.1 Hirsch-Fye algorithm	63
5.5.2 Projective quantum Monte Carlo simulations for $T=0$	70
5.5.3 Fourier transformation from τ to $i\omega_\nu$	72
5.5.4 Maximum entropy method	74
5.6 Comparing different DMFT solvers for $\text{La}_{1-x}\text{Sr}_x\text{TiO}_3$	75
6 Realistic material calculations with DMFT	78
6.1 f electron systems	78
6.1.1 Volume collapse transition in cerium	79
6.2 Transition metals	84
6.2.1 Ferromagnetism in Fe and Ni	84
6.3 Transition metal oxides	86
6.3.1 Ferro-orbital order in LaTiO_3	87
6.3.2 Mott-Hubbard transition in V_2O_3	87
6.3.3 Peierls transition in VO_2	90
6.3.4 Orbital selective Mott-Hubbard transition in $\text{Ca}_{2-x}\text{Sr}_x\text{RuO}_4$	90
6.3.5 'Kinks' in SrVO_3	91
6.3.6 e'_g hole pockets in Na_xCO_2	95
6.3.7 Heavy-Fermion behaviour in LiV_2O_4	96
6.3.8 Colossal magnetoresistance in manganites	96
6.4 Other Materials	98
6.4.1 Half-metallic ferromagnetism in Heussler alloys	98
6.4.2 Superconductivity in A_xC_{60}	99
6.4.3 Mott-insulating zeolites	100
7 Summary and outlook	101
References	104

1 Introduction

One of the most important challenges of theoretical physics is the development of reliable methods for the quantitative calculation of material properties. In solid state theory, we know the Hamiltonian to do these material calculations. For example, if we neglect relativistic corrections and employ the Born-Oppenheimer (1) approximation, this Hamiltonian consists of three terms: the kinetic energy, the lattice potential and the Coulomb interaction between the electrons:

$$H = \sum_i \left[-\frac{\hbar^2 \Delta_i}{2m_e} + \sum_l \frac{-e^2}{4\pi\epsilon_0} \frac{Z_l}{|\mathbf{r}_i - \mathbf{R}_l|} \right] + \frac{1}{2} \sum_{i \neq j} \frac{e^2}{4\pi\epsilon_0} \frac{1}{|\mathbf{r}_i - \mathbf{r}_j|}. \quad (1)$$

Here, \mathbf{r}_i and \mathbf{R}_l denote the position of electron i and ion l with charge $-e$ and $Z_l e$, respectively; Δ_i is the Laplace operator for the kinetic energy of electrons with mass m_e ; ϵ_0 and \hbar are the vacuum dielectric and Planck constant.

The three terms of Hamiltonian [1] describe the movement of the electrons,

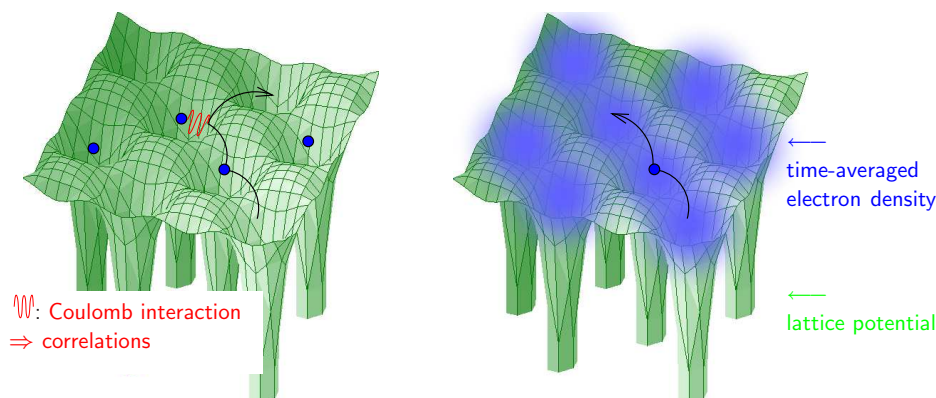


Figure 1.

Solid State Hamiltonian:

To calculate the physical properties of a given material, one has to take into account three terms (Hamiltonian [1]): The kinetic energy due to which the electrons move (arrow), the lattice potential of the ions and the Coulomb interaction between the electrons. Due to the latter, the moving electron is repelled by the electron already located at this site. It is energetically favourable if the depicted electron hops somewhere else, as indicated by the arrow. Hence, the movement of every electron is correlated with that of every other.

LDA approximation:

LDA is an approximation which allows for calculating material properties, but dramatically simplifies the electronic correlations: The LDA bandstructure corresponds to the simplification that every electron moves independently, i.e. uncorrelated, within a time-averaged local density of the other electrons (visualised as static clouds in the figure).

the attractive lattice potential of the (fixed) ions and the mutual Coulomb repulsion of the electrons, see Fig. 1 for an illustration. But while we know the Hamiltonian, we cannot solve it, even not numerically, if more than a very few [$\mathcal{O}(10)$] electrons are involved. This problem is due to the last term, the Coulomb interaction, which correlates the movement of every electron i with every other electron j . The numerical effort to solve Eq. [1] quantum-mechanically grows exponentially with the number of correlated electrons. Such an exponential problem cannot be solved for significantly many electrons, even if computer power continued to grow rapidly.

In this situation, we have two possibilities: Either we dramatically simplify the Hamiltonian [1], hoping that the simplified model allows for a qualitative

understanding including electronic correlation. Or we employ equally dramatic approximations to deal with Eq. [1] directly. These two strategies have been followed by the two large communities of solid state theory: the many-body model Hamiltonian and the density functional community.

Within the density functional theory (DFT) introduced by Hohenberg and Kohn (2), the local density approximation (LDA) turned out to be unexpectedly successful, and established itself as *the* method for realistic solid state calculations in the last century; for reviews see e.g. Refs. (3; 4; 5; 6). This is surprising because LDA represents a substantial approximation to the Coulomb interaction. Basically, an electron at \mathbf{r}_i sees a time-averaged *local* density $\rho(\mathbf{r}_i)$ of the other electrons, with a corresponding *local* LDA potential $V_{\text{LDA}}(\rho(\mathbf{r}_i))$, as visualised in Fig. 1. This reduces the many-body problem to a single electron calculation in a *local* potential.

The success of LDA shows that this treatment is actually sufficient for many materials, both for calculating ground state energies and bandstructures, implying that electronic correlations are rather weak in these materials. But, there are important classes of materials where LDA fails, such as transition metal oxides or heavy Fermion systems. For example, LDA predicts La_2CuO_4 , Cr-doped V_2O_3 and NiO to be metals above the antiferromagnetic ordering temperature whereas, in reality, these materials are insulators (7; 8; 9; 10; 11). Similarly, the LDA bandstructure is in strong disagreement with experiment for *f*-electron systems. In these two classes of materials, the valence electrons partially occupy the *d* or *f* orbitals. If there are two electrons in these narrow orbitals on the same lattice site, the distance $|\mathbf{r}_i - \mathbf{r}_j|$ is particularly short, and electronic correlations are thus particularly strong. Hence, the approximate LDA treatment of Hamiltonian [1] fails.

To describe these *d*- and *f*-electron systems correctly, genuine many-body effects have to be taken into account. The transition metal oxides mentioned above are, for example, Mott insulators (12; 13; 14). Since the *d* orbitals are only partially filled the LDA bandstructure predicts metallic behaviour, see the left panel of Fig. 2. But instead, the on-(lattice-)site Coulomb repulsion U splits the metallic LDA bands into two sets of Hubbard (15) bands, as in the right panel of Fig. 2. Let us for a moment assume that the average number of *d* or *f* electrons is one per lattice site ('integer filling'). Then, one can envisage the lower Hubbard band as consisting of all states with exactly one electron on every lattice site and the upper Hubbard band as those states where two electrons are in *d* or *f* orbitals on the same lattice site. Since it costs an energy U to have two electrons on the same lattice sites, the latter states are completely empty and the former completely filled with a gap of size U in between. Such kind of Mott-Hubbard physics and the associated energy gain is completely missing in the LDA.

This shortcoming can be overcome by the self interaction correction (SIC)

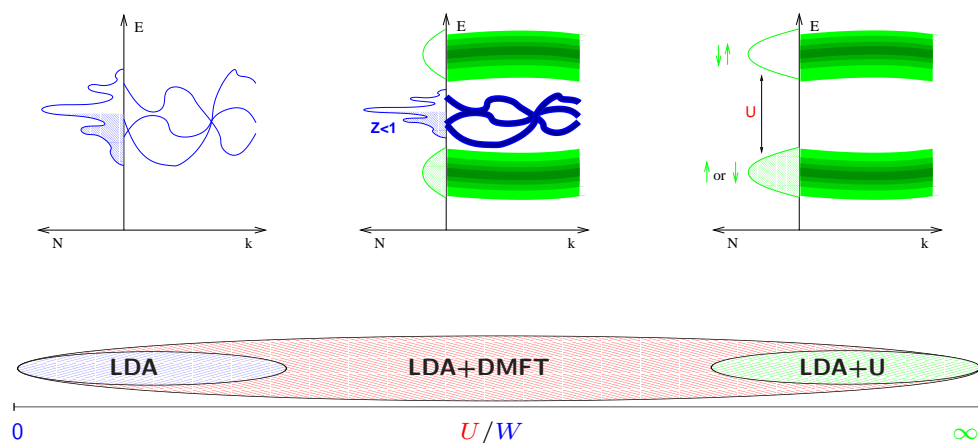


Figure 2.

Weakly

correlated metal:

The on-site Coulomb interaction is weak compared to the LDA bandwidth: $U \ll W$; and LDA gives the correct answer, typically a (weakly correlated) metal for which we schematically draw a density of states N at energies E and the bandstructure, i.e. E vs. wave vector \mathbf{k} .

Strongly

correlated metal:

In this intermediate regime, one has already Hubbard bands, like for $U/W \gg 1$ (right hand side), but at the same time a remainder of the weakly correlated LDA metal (left hand side), in form of a quasiparticle peak: The ($U=0$) LDA bandstructure is reproduced, albeit with its width and weight reduced by a factor Z and life time effects which result in a Lorentzian broadening of the quasiparticle levels.

Mott insulator:

If the Coulomb interaction U becomes large ($U \gg W$), the LDA band splits into two Hubbard bands, and we have a Mott insulator with only the lower band occupied (at integer fillings). Such a splitting can be described by the so-called LDA+U method with the drawbacks discussed in the text.

The entire parameter regime is described by LDA+DMFT.

to LDA by Perdew and Zunger (16; 17; 18) or by the LDA+U method of Anisimov *et al.* (19) which we will discuss in Section 5.1. In the presence of orbital or magnetic ordering these approaches yield insulating spectra, similar to that of the paramagnetic Mott insulator displayed in the right panel of Fig. 2. Important differences are that the LDA+U spectra are completely coherent and that the LDA+U solution has not the high entropy of the finite temperature paramagnetic solution, because of the orbital or magnetic ordering. For

ordered systems on the other hand, polarons (20; 21; 22; 23; 24) result in additional peaks in the Hubbard bands. As was noted by Sangiovanni *et al.* (25) these polaron peaks are present in dynamical mean field theory (26) but not in the static LDA+U mean field theory. Another drawback is that SIC-LDA and LDA+U almost automatically yield localised electrons with split (Hubbard) bands, even if this is not correct.

Missing in both LDA and LDA+U is also the strongly correlated metallic phase found in many transition metal oxides and heavy Fermion systems either at intermediate values of U or at a non-integer number of d or f electrons per site so that the Mott insulator is doped and becomes metallic. This strongly correlated metal already has Hubbard bands as the Mott insulator, but the low-energy behaviour is dominated by *quasiparticle* physics, see the central panel of Fig. 2. We can think of these quasiparticles as dressed electrons which move independently from each other, although with a larger effective mass m since the quasiparticle consists of the initial electron plus the electron-electron interaction with its environment. The mass enhancement m/m_e becomes more pronounced with increasing U , and the weight of the quasiparticle peak $Z = (m/m_e)^{-1}$ is reduced correspondingly until it vanishes completely at the Mott-Hubbard transition where the system becomes insulating.

A modern, non-perturbative technique to describe these many-body effects is the dynamical mean field theory (DMFT) developed primarily by Metzner and Vollhardt (27), Müller-Hartmann (28), Georges and Kotliar (29), and Jarrell (30); for more details see Section 3. One of the strong points of DMFT is that it can describe such strongly correlated metals and Mott insulators in a single framework.

Recently, physicists from the many-body and DFT community have developed a new approach to correlated materials which merges two of the most successful approaches of the two communities: LDA+DMFT. The initial work by Anisimov *et al.* (31) and Lichtenstein and Katsnelson (32) was followed by a rapid development which is the subject of this Review. Shorter LDA+DMFT summaries have already been published in the form of conference proceedings, lecture notes and a Psi-k Highlight, see Refs. (33; 34; 35; 36; 37; 38; 39); a full review was submitted by Kotliar *et al.* (40) during the completion of this work. Instead of LDA, one can also use the so-called GW approximation of Hedin (41), resulting in the related GW+DMFT approach formulated by Biermann *et al.* (42) and presented in more detail in Ref. (43) and Ref. (44).

The LDA+DMFT approach does not only contain the correct quasiparticle physics and energy of the strongly correlated metallic phase, but also reproduces the correct results in the limit of small and large U , see Fig. 2. Hence, LDA+DMFT correctly accounts for the main contributions of electronic correlations (there are corrections due to the \mathbf{k} -dependence of the self energy as discussed in Section 3.2). In contrast, LDA yields an uncorrelated metal even

for strongly-correlated metals or Mott insulators. LDA+U on the other hand typically predicts an insulator for the *ab-initio* calculated U values of 3d transition metal oxides, even for materials which are metallic. Considering this, it might not be so astonishing that LDA+DMFT turned out to be a breakthrough for the calculation of materials with strong electronic correlations.

In the following, we will review these recent developments at the former borderline between DFT and many-body theory. Thereby we take a Hamiltonian point of view which allows us to understand physically what LDA+DMFT describes, and what it does not. Complementarily, the review of Kotliar *et al.* (40) focuses on the spectral density functional theory for which LDA+DMFT is the standard approximation just as LDA is for DFT.

We start, in Section 2, with a brief recapitulation of conventional DFT/LDA band structure calculation. For more LDA and DFT details, we advise the reader to consult the excellent review by Jones and Gunnarsson (3) or the books Refs. (3; 4; 5; 6). In the present Review, we will not elaborate on how to construct an optimal set of wave functions within LDA and how to choose maximally localised orbitals for the further many-body DMFT calculation. To this end, the linearised muffin tin orbitals (LMTO) of Andersen (45), for example, in the third generation (46; 47), or the Wannier (48) function projection by Marzari and Vanderbilt (49) can be employed; also see Refs. (50; 51; 52; 53; 54; 55). We refer the reader to these original and review publications for the full specification of the orbital basis sets whose construction is a science on its own.

In Section 3, we give a compendious introduction to DMFT, without discussing all derivations of the DMFT equations and the physics of the Mott transition since this has been reviewed by Georges *et al.* (56). The central part of this review is Section 4 in which the recently proposed methods employing DMFT for realistic material calculations are introduced. In particular, we will discuss the LDA+DMFT method in Section 4.1, a combination of the Hartree approximation and DMFT in Section 4.2, and the GW+DMFT approach in Section 4.3. For more details on the GW approximation itself, we recommend the review by Aryasetiawan and Gunnarsson (57). Section 5 is devoted to several methods, numerically exact and approximate ones, for solving the DMFT equations. The respective advantages and disadvantages are discussed.

In Section 6, we review the successful electronic structure calculations with DMFT accomplished for f -electron systems, transition metals and their oxides. Finally in Section 7 we give a summary and outlook.

2 Conventional electronic structure calculations

2.1 *Ab initio* Hamiltonian

Let us start by rewriting the *ab initio* Hamiltonian [1] in second, instead of first, quantised form:

$$\begin{aligned} \hat{H} = & \sum_{\sigma} \int d^3r \, \hat{\Psi}^+(\mathbf{r}, \sigma) \left[-\frac{\hbar^2}{2m_e} \Delta + \underbrace{\sum_l \frac{-e^2}{4\pi\epsilon_0} \frac{Z_l}{|\mathbf{r} - \mathbf{R}_l|}}_{\equiv V_{\text{ion}}(\mathbf{r})} \right] \hat{\Psi}(\mathbf{r}, \sigma) \\ & + \frac{1}{2} \sum_{\sigma\sigma'} \int d^3r d^3r' \, \hat{\Psi}^+(\mathbf{r}, \sigma) \hat{\Psi}^+(\mathbf{r}', \sigma') \underbrace{\frac{e^2}{4\pi\epsilon_0} \frac{1}{|\mathbf{r} - \mathbf{r}'|}}_{\equiv V_{\text{ee}}(\mathbf{r}-\mathbf{r}')} \hat{\Psi}(\mathbf{r}', \sigma') \hat{\Psi}(\mathbf{r}, \sigma), \end{aligned} \quad (2)$$

where now $\hat{\Psi}^+(\mathbf{r}, \sigma)$ and $\hat{\Psi}(\mathbf{r}, \sigma)$ are field operators that create and annihilate an electron at position \mathbf{r} with spin σ ; $V_{\text{ion}}(\mathbf{r})$ and $V_{\text{ee}}(\mathbf{r})$ denote the lattice potential and the electron-electron interaction, respectively; for the other symbols see Eq. [1].

Not included in Eq. [2] are the kinetic energy of the lattice ions (phonons) and relativistic corrections, in particular, the spin-orbit coupling. Both are known to be important in some materials. For example, the electron-phonon coupling plays an important role in Jahn-Teller distorted manganites according to Millis *et al.* (58). The spin-orbit coupling on the other hand is important for *f*-electron systems.

2.2 *Density functional theory (DFT)*

The basic idea of density functional theory (DFT) is to work with a simple quantity, i.e. the electron density $\rho(\mathbf{r})$, instead of trying to solve the *ab initio* Hamiltonian [1,2] through complicated many-body wave functions. This is possible, at least for the ground state energy and its derivatives, thanks to the Hohenberg-Kohn (2) theorem, which states that the ground state energy is a functional of the electron density $E[\rho(\mathbf{r})]$ which is minimised at the ground state density $\rho(\mathbf{r}) = \rho_0(\mathbf{r})$. Following Levy (59), this theorem can be easily proven and the functional even be constructed by a two-step minimisation process, see Fig. 3. In a first step, we select all many-body wave functions $\varphi(\mathbf{r}_1\sigma_1, \dots, \mathbf{r}_N\sigma_N)$ for a fixed number of electrons N which yield a certain electron density $\rho(\mathbf{r})$, and minimise the energy expectation value for these wave

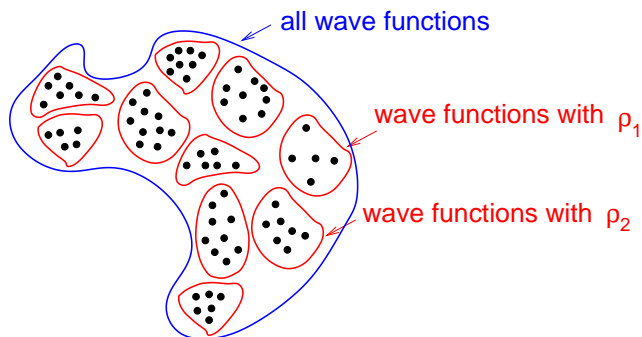


Figure 3. Construction of the DFT functional according to Levy (59). The DFT energy functional for a given electron density $\rho_1(\mathbf{r})$ is the minimal expectation value of all wave functions yielding $\rho_1(\mathbf{r})$.

functions

$$E[\rho] = \min \left\{ \langle \varphi | \hat{H} | \varphi \rangle \mid \langle \varphi | \sum_{i=1}^N \delta(\mathbf{r} - \mathbf{r}_i) | \varphi \rangle = \rho(\mathbf{r}) \right\}. \quad (3)$$

This is exactly the DFT functional for the ground state energy: A second minimisation yields the ground state energy $E_0 = \min_{\rho} E[\rho]$ at the ground state density ρ_0 , since for the ground state density $E[\rho_0]$ includes the energy expectation value w.r.t the ground state wave function, see Fig. 3 for an illustration.

While this construction proves the Hohenberg-Kohn theorem, we did actually not gain anything: For obtaining $E[\rho]$ we have to calculate the expectation value $\langle \varphi | \hat{H} | \varphi \rangle$ for complicated many-body wave functions φ . Only the ionic potential $E_{\text{ion}}[\rho] = \int d^3r V_{\text{ion}}(\mathbf{r}) \rho(\mathbf{r})$ and the Hartree term $E_{\text{Hartree}}[\rho] = \frac{1}{2} \int d^3r' d^3r V_{\text{ee}}(\mathbf{r} - \mathbf{r}') \rho(\mathbf{r}') \rho(\mathbf{r})$ can be expressed easily through the electron density. Denoting by $E_{\text{kin}}[\rho]$ the kinetic energy functional, we can hence write

$$E[\rho] = E_{\text{kin}}[\rho] + E_{\text{ion}}[\rho] + E_{\text{Hartree}}[\rho] + E_{\text{xc}}[\rho], \quad (4)$$

where all the difficulty is now hidden in the exchange and correlation term $E_{\text{xc}}[\rho]$. This term is unknown. An important aspect of DFT is however that the functional $E[\rho] - E_{\text{ion}}[\rho]$ does not depend on the material investigated; for a prove see e.g. Ref. (3). Hence, if we knew the DFT functional for one material, we could calculate all materials by simply adding $E_{\text{ion}}[\rho]$.

For calculating the ground state energy and density, we have to minimise $\delta\{E[\rho] - \mu(\int d^3r \rho(\mathbf{r}) - N)\} / \delta \rho(\mathbf{r}) = 0$ where the Lagrange parameter μ fixes the number of electrons to N . To avoid the difficulty of expressing the kinetic energy $E_{\text{kin}}[\rho]$ through $\rho(\mathbf{r})$, Kohn and Sham (60) introduced an (at this point

auxiliary) set of one-particle wave functions φ_i yielding the density

$$\rho(\mathbf{r}) = \sum_{i=1}^N |\varphi_i(\mathbf{r})|^2, \quad (5)$$

and minimised w.r.t. the φ_i 's instead of $\rho(\mathbf{r})$. That is, we minimise $\delta\{E[\rho] - \varepsilon_i[\int d^3r |\varphi_i(\mathbf{r})|^2] - 1\}/\delta\varphi_i(\mathbf{r}) = 0$ where the Lagrange parameters ε_i guarantee the normalisation of the φ_i 's. This minimisation leads us to the Kohn-Sham (60) equations

$$\left[-\frac{\hbar^2}{2m_e}\Delta + V_{\text{ion}}(\mathbf{r}) + \int d^3r' V_{\text{ee}}(\mathbf{r}-\mathbf{r}')\rho(\mathbf{r}') + \frac{\delta E_{\text{xc}}[\rho]}{\delta\rho(\mathbf{r})} \right] \varphi_i(\mathbf{r}) = \varepsilon_i \varphi_i(\mathbf{r}). \quad (6)$$

These Kohn-Sham equations are Schrödinger equations, describing single electrons moving in a time-averaged potential

$$V_{\text{eff}}(\mathbf{r}) = V_{\text{ion}}(\mathbf{r}) + \int d^3r' V_{\text{ee}}(\mathbf{r}-\mathbf{r}')\rho(\mathbf{r}') + \frac{\delta E_{\text{xc}}[\rho]}{\delta\rho(\mathbf{r})} \quad (7)$$

of all electrons. The Kohn-Sham equations and the electron density have to be calculated self-consistently, see the flow diagram Fig. 4.

Let us note that the one-particle Kohn-Sham equations serve, in principle, only the purpose of minimising the DFT energy, and have no physical meaning. If we knew the exact E_{xc} , which is non-local in $\rho(\mathbf{r})$, we would obtain the exact ground state energy and density. However, in practise, one has to make approximations to E_{xc} such as the local density approximation discussed in the next Section. We can then think of these approximations as describing single electrons moving in an approximated potential $\delta E_{\text{xc}}[\rho]/\delta\rho(\mathbf{r})$, as illustrated in the Introduction, Fig. 1.

Let us also note that the kinetic energy in Eq. [7], $E_{\text{kin}}[\rho_{\text{min}}] = -\sum_{i=1}^N \langle \varphi_i | \hbar^2 \Delta / (2m_e) | \varphi_i \rangle$, is that of independent (uncorrelated) electrons. The true kinetic energy functional for the many-body problem is different. We hence have to add the difference between the true kinetic energy functional for the many-body problem and the above uncorrelated kinetic energy to E_{xc} , so that all many-body difficulties are buried in E_{xc} .

2.3 Local density approximation (LDA)

Since we do not know E_{xc} exactly, we have to make approximations, and the most widely employed approximation is the local density approximation (LDA). In LDA, the complicated non-local functional $E_{\text{xc}}[\rho]$ is replaced by a

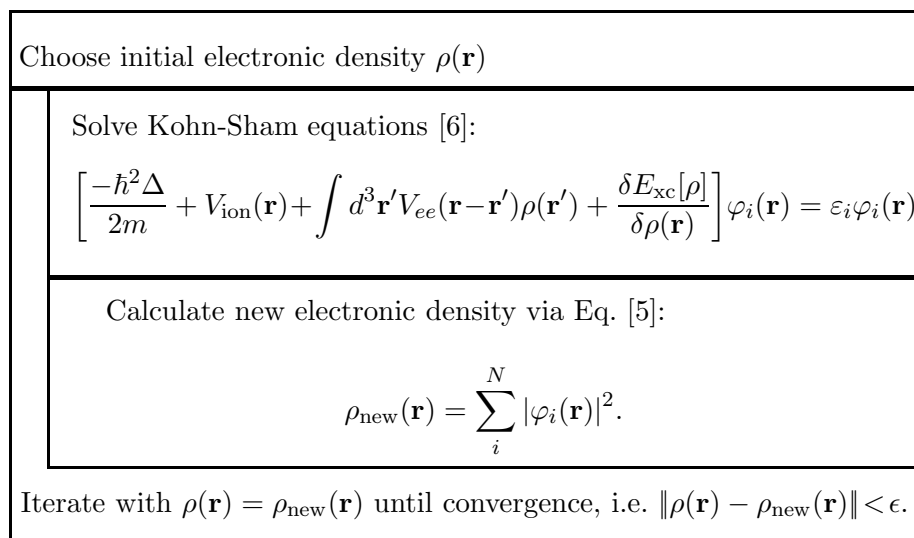


Figure 4. Flow diagram of the DFT/LDA calculations.

local (LDA) exchange energy density¹ which is a function of the local density only:

$$E_{\text{xc}}[\rho] \overset{\text{LDA}}{\approx} \int d^3 r E_{\text{xc}}^{\text{LDA}}(\rho(\mathbf{r})). \quad (8)$$

In practise, $E_{\text{xc}}^{\text{LDA}}(\rho(\mathbf{r}))$ is calculated from the perturbative solution (61; 62) or the numerical simulation (63) of the jellium model which is defined by $V_{\text{ion}}(\mathbf{r}) = \text{const}$. Due to translational symmetry, the jellium model has a constant electron density $\rho(\mathbf{r}) = \rho_0$. Hence, with the correct jellium $E_{\text{xc}}^{\text{LDA}}$, we could calculate the energy of any material with a constant electron density exactly. However, for real materials $\rho(\mathbf{r})$ is varying, less so for s and p valence electrons but strongly for d and f electrons. While LDA turned out to be unexpectedly successful for many materials, it fails for materials with strong electronic correlations between the d or f electrons. In this paper, we will review recent advances to improve on LDA for such correlated materials by using DMFT.

To understand these advances physically, let us now turn to the LDA calculation of band structures, one of the main applications of LDA. If we calculate a LDA band structures we will leave the firm ground of DFT, which strictly

¹Note that in the literature, e.g. in (3), often the exchange energy density *per particle* $\epsilon_{\text{xc}}^{\text{LDA}}(\rho(\mathbf{r})) = E_{\text{xc}}^{\text{LDA}}(\rho(\mathbf{r}))/\rho(\mathbf{r})$ is used.

speaking only allows for calculating the ground state energy and its derivatives. Instead, for the LDA bandstructure, we interpret the Lagrange parameters ε_i as the physical (one-particle) energies of the system. This corresponds exactly to the picture Fig. 1 of Section 1. Physically, the one-particle LDA bandstructure corresponds to approximating the *ab initio* many-body Hamiltonian by

$$\hat{H}_{\text{LDA}} = \sum_{\sigma} \int d^3r \hat{\Psi}^+(\mathbf{r}, \sigma) \left[-\frac{\hbar^2}{2m_e} \Delta + V_{\text{ion}}(\mathbf{r}) + \int d^3r' \rho(\mathbf{r}') V_{\text{ee}}(\mathbf{r} - \mathbf{r}') + \frac{\partial E_{\text{xc}}^{\text{LDA}}(\rho(\mathbf{r}))}{\partial \rho(\mathbf{r})} \right] \hat{\Psi}(\mathbf{r}, \sigma). \quad (9)$$

In practise, one solves the three-dimensional one-electron Kohn-Sham equations given by Hamiltonian [9] through expanding the wave functions in sophisticatedly chosen basis sets. These basis sets use either the atom and so called muffin tin potentials, or free electrons in, e.g. ultrasoft (64), pseudopotentials as a starting point; for a detailed discussion see (4). An important aspect for merging LDA with DMFT is that we need to identify the correlated *d* or *f* orbitals. For the linearised muffin-tin orbital (LMTO) basis of Andersen (45), and its *N*th order extension (NMTO) (46; 47), these orbitals are inherently defined. For other basis sets, e.g. plane waves, one has first to project onto Wannier orbitals (49) before doing the DMFT calculation.

Let us now transform our \mathbf{r} -basis to such a basis with localised *d* or *f* orbitals:

$$\hat{\Psi}^+(\mathbf{r}, \sigma) = \sum_{il} \hat{c}_{il}^{\sigma\dagger} \varphi_{il}^*(\mathbf{r}). \quad (10)$$

Here, *l* denotes the orbital index (which, for problems with more than one atom in the unit cell, will also index orbitals on different sites in this unit cell.) Transforming the Hamiltonian [9] to this orbital basis, we obtain

$$\hat{H}_{\text{LDA}} = \sum_{iljm\sigma} t_{iljm} \hat{c}_{il}^{\sigma\dagger} \hat{c}_{jm}^{\sigma}, \quad (11)$$

where t_{iljm} denotes the tight-binding hopping matrix elements

$$t_{iljm} = \int d^3r \varphi_{il}^*(\mathbf{r}) \left[-\frac{\hbar^2}{2m_e} \Delta + V_{\text{ion}}(\mathbf{r}) + \int d^3r' \rho(\mathbf{r}') V_{\text{ee}}(\mathbf{r} - \mathbf{r}') + \frac{\partial E_{\text{xc}}^{\text{LDA}}(\rho(\mathbf{r}))}{\partial \rho(\mathbf{r})} \right] \varphi_{jm}(\mathbf{r}). \quad (12)$$

According to the Bloch theorem, we can diagonalise Hamiltonian [11] by

Fourier transforming to $\hat{c}_{\mathbf{k}l} = \frac{1}{\sqrt{L}} \sum_i \hat{c}_{il} e^{-i\mathbf{k}\mathbf{R}_i}$ (L denotes the number of lattice sites \mathbf{R}_i):

$$\hat{H}_{\text{LDA}} = \sum_{\mathbf{k}\sigma lm} \epsilon_{lm}^{\text{LDA}}(\mathbf{k}) \hat{c}_{\mathbf{k}l}^{\sigma\dagger} \hat{c}_{\mathbf{k}m}^{\sigma}. \quad (13)$$

Here,

$$\epsilon_{lm}^{\text{LDA}}(\mathbf{k}) = \frac{1}{L} \sum_{ij} t_{iljm} e^{i\mathbf{k}(\mathbf{R}_i - \mathbf{R}_j)} \quad (14)$$

is still a matrix in our orbital indices which can be fully diagonalized by a simple orbital rotation. This orbital rotation yields the Kohn-Sham eigenvalues, i.e. the LDA bandstructure. Let us emphasise that this rotation is different one for every \mathbf{k} point.

As already mentioned, LDA is highly successful for calculating both, static physical properties and bandstructures. But LDA is not reliable when applied to correlated materials and can even be completely wrong because it treats electronic *correlations* only very rudimentarily: The exchange correlation functional has been approximated by a functional which depends only on the *local* density. It has been calculated from the jellium problem, a weakly correlated model with extended orbitals. Basically, LDA is a one-electron approach where the effect of the other electrons is through a static (time independent) mean field. In the following, we will discuss how to treat electronic correlations in a better way with dynamical mean field theory (DMFT).

3 Dynamical mean field theory (DMFT)

The conventional approach to strongly correlated electron systems is perturbation theory, either starting from the limit of zero Coulomb interaction ($U = 0$; weak coupling) or from the opposite limit of zero kinetic energy ($W = 0$; strong coupling). Such a treatment is, however, not appropriate for the important ‘in-between’ regime where we have a strongly correlated metal and possibly a Mott-Hubbard transition between this correlated metal and a Mott insulator (see Fig. 2).

Metzner and Vollhardt (27) introduced a new limit to correlated electron systems, the limit of infinite dimensions $d \rightarrow \infty$ or equivalently an infinite number of neighbouring lattice sites. In this limit, the competition between kinetic energy W and Coulomb interaction U is maintained, albeit resulting in a simplified, momentum-independent self energy: $\Sigma_{\mathbf{k}}(\omega) \xrightarrow{d \rightarrow \infty} \Sigma(\omega)$. The work by

Metzner and Vollhardt (27) initiated a rapid development: Müller-Hartmann (28; 65; 66) showed only the local Coulomb interaction yields dynamic (ω -dependent) correlations whereas the non-local density-density interactions are reduced to the Hartree contribution which is ω -independent. Some models like the Falicov-Kimball model (67) and the Kondo lattice model for classical spins could even be solved exactly by Brandt and Mielsch (68; 69; 70; 71; 72; 73) and Furukawa (74; 75), respectively. The next important step was to put the initial ideas on the footings of a mean field theory, coined *dynamical* mean field theory (DMFT) because of the frequency dependence of $\Sigma(\omega)$. For the Falicov-Kimball model, Brandt and Mielsch (68; 69; 70) already succeeded in this respect, and Janiš and Vollhardt (76; 77) generalised the coherent potential approximation (CPA) to include the dynamics of correlated electron models in the $d \rightarrow \infty$ limit. But the breakthrough represents the work by Georges and Kotliar (29) (also see Ref. (30) and Ref. (78; 79)) who showed that a many-body model like the Hubbard model is mapped onto the self-consistent solution of an auxiliary Anderson impurity model for $d \rightarrow \infty$ (for the physics of this Anderson impurity model see e.g. (80; 81)). This mapping was crucial for the following development since physicists were thenceforth able to employ well-known solvers for the Anderson impurity model to deal now with lattice many-body models in the DMFT framework: Approximate solvers like iterated perturbation theory (29), self-consistent perturbation theory (66; 82), and the non-crossing approximation (83; 84; 85; 86); and numerically exact solvers like quantum Monte Carlo simulations (30; 87; 88), exact diagonalisation (89) and the numerical renormalisation group (90; 91).

The DMFT results turned out to be a big step forward for our understanding of, for example, the Hubbard model and the periodic Anderson model, and improved our insight, particularly into the Mott-Hubbard transition; see Georges *et al.* (56) for a review and Kotliar and Vollhardt (92) for a first reading.

Since DMFT is central to this review, which addresses readers from different communities, we feel a self-contained derivation of DMFT is helpful. In Section 3.1, we present such a derivation based on the local nature of the weak-coupling perturbation theory, as first noticed by Metzner and Vollhardt (27) and Müller-Hartmann (28). Alternative derivations of the DMFT equations have used the cavity method (56), the expansion around the atomic limit (93) and a generalisation of the coherent potential approximation (76; 77). The reader who is not interested in this derivation might directly turn to the DMFT self-consistency scheme summarised on p. 21 ff. Shortcomings and extensions of DMFT by non-local correlations are discussed in Section 3.2.

3.1 Derivation of the DMFT equations

Let us in the following consider a generalised many-body Hamiltonian

$$\hat{H} = \sum_{iljm\sigma} t_{iljm} \hat{c}_{il}^{\sigma\dagger} \hat{c}_{jm}^{\sigma} + \sum_{ilmno\sigma\sigma'} U_{lmno} \hat{c}_{il}^{\sigma\dagger} \hat{c}_{im}^{\sigma'\dagger} \hat{c}_{in}^{\sigma'} \hat{c}_{io}^{\sigma}, \quad (15)$$

where $\hat{c}_{il}^{\sigma\dagger}$ (\hat{c}_{il}^{σ}) creates (annihilates) an electron with spin σ and orbital index l at lattice site i ; t_{iljm} is a hopping amplitude between lattice sites i and j and orbitals l and m [of the same form as in Eq. [11]]; finally, U_{lmno} denotes a general local Coulomb interaction.

Proper scaling in the limit $d \rightarrow \infty$ —Let us consider an extension of the lattice at hand so that we have a large number $\mathcal{Z}_{\|i-j\|}$ of equivalent (neighbouring) sites, with the same ‘distance’ $\|i-j\|$ to site i . Later, we will consider the limit $\mathcal{Z}_{\|i-j\|} \rightarrow \infty$. The reader might envisage, for example, the generalisation of the cubic lattice to a d -dimensional hypercubic lattice. This hypercubic lattice has $\mathcal{Z}_1 = 2d$ (6 for $d = 3$) nearest neighbours and, in general, $\mathcal{Z}_{\|i-j\|} \sim d^{\|i-j\|}$ equivalent sites at distance $\|i-j\|$ (to leading order in $1/d$). For the cubic lattice, $\|\dots\|$ is the so-called Manhattan norm. The advantage of the notation $\mathcal{Z}_{\|i-j\|}$ is that all classes of equivalent sites and different lattice topologies can be treated on the same footings. The reader will however realise that these $\mathcal{Z}_{\|i-j\|}$ ’s are in general not independent.

How do the two terms of Hamiltonian [15] scale with increasing $\mathcal{Z}_{\|i-j\|}$ in the limit $\mathcal{Z}_{\|i-j\|} \rightarrow \infty$? Obviously, the purely local interaction U_{lmno} and the associated potential energy per site scales like

$$\left\langle \sum_{ilmno\sigma\sigma'} U_{lmno} \hat{c}_{il}^{\sigma\dagger} \hat{c}_{im}^{\sigma'\dagger} \hat{c}_{in}^{\sigma'} \hat{c}_{io}^{\sigma} \right\rangle \xrightarrow{\mathcal{Z}_{\|i-j\|} \rightarrow \infty} \text{const.}, \quad (16)$$

i.e. stays at a finite constant, neither going to zero nor infinity. Here and in the following,

$$\langle \hat{\mathcal{O}} \rangle = \frac{\text{Tr } \hat{\mathcal{O}} e^{-\beta \hat{H}}}{\text{Tr } e^{-\beta \hat{H}}} \quad (17)$$

denotes the thermal expectation value at inverse temperature $\beta = 1/T$; Tr is the trace.

For the first term of Hamiltonian [15], the kinetic energy, we have $\mathcal{Z}_{\|i-j\|}$ equivalent j terms in the sum. Hence, the kinetic energy per site i diverges unless we rescale t_{iljm} in the limit $\mathcal{Z}_{\|i-j\|} \rightarrow \infty$. To avoid this divergence, let

us consider the following ansatz for the scaling of these hopping amplitudes:

$$t_{iljm} = \frac{t_{iljm}^*}{\sqrt{\mathcal{Z}_{\parallel i-j\parallel}}} \quad (18)$$

with t_{iljm}^* staying constant upon increasing $\mathcal{Z}_{\parallel i-j\parallel}$. Since the non-interacting ($U = 0$) Green function¹ $G_{iljm}^0(\omega)$ is directly connected to t_{iljm} it scales exactly in the same way²:

$$G_{iljm}^0(\omega) = [(\omega \underline{\mathbf{1}} - \underline{\mathbf{t}})^{-1}]_{iljm} \sim \frac{1}{\sqrt{\mathcal{Z}_{\parallel i-j\parallel}}}. \quad (19)$$

Here, bold symbols with double underlines denote matrices w.r.t. orbital and site indices ($\underline{\mathbf{1}}$ is the unit and $\underline{\mathbf{t}}$ the hopping matrix). Let us assume for a moment that the very same scaling also holds for the interacting Green function

$$G_{iljm}(\omega) \sim \frac{1}{\sqrt{\mathcal{Z}_{\parallel i-j\parallel}}}. \quad (20)$$

Later, we will see that indeed all Feynman diagrams for $\mathbf{G}(\omega)$ scale like Eq. [20] or fall off even faster.

With the scaling Eq. [20], the kinetic energy per site scales properly, i.e. stays finite:

$$\sum_{ljm\sigma} t_{iljm} \langle \hat{c}_{il}^{\sigma\dagger} \hat{c}_{jm}^{\sigma} \rangle \xrightarrow{\mathcal{Z}_{\parallel i-j\parallel} \rightarrow \infty} \text{const.} \quad (21)$$

To see this, note that there are $\mathcal{Z}_{\parallel i-j\parallel}$ terms in the sum for every class of equivalent sites j . This factor is however canceled by a factor $\frac{1}{\sqrt{\mathcal{Z}_{\parallel i-j\parallel}}}$ for t_{iljm}

¹Depending on the problem at hand, we will work with Green functions for real time/frequencies or imaginary time/Matsubara frequencies [$\omega_\nu = (2\nu + 1)\pi/\beta$]; see Ref. (94) for an introduction. Both representations are connected via the analytical continuation in the complex plane. Let us define for completeness the real time Green function

$$G_{iljm}(t - t') = -i\Theta(t - t') \langle T c_{il}(t) c_{jm}^\dagger(t') \rangle$$

and the imaginary time (thermal) Green function

$$G_{iljm}(\tau - \tau') = -\langle T c_{il}(-i\tau) c_{jm}^\dagger(-i\tau') \rangle.$$

Here, T is the Wick time-ordering operator w.r.t. t or τ and $c_{il}(t) = \exp(i\hat{H}t)c_{il}\exp(-i\hat{H}t)$ in both cases. The corresponding frequency-dependent Green functions follow by Fourier transformation.

²Expressing the matrix elements of the inversion in Eq. [19] in terms of minors one directly sees that the off-diagonal elements are a factor $t_{iljm}/(\omega - t_{iljm})$ smaller than the diagonal elements.

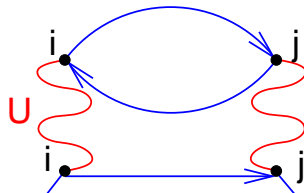


Figure 5. A second-order diagram for the Green function (or the self energy if the legs are amputated). A simple power counting of the three Green functions connecting i and j shows that the contribution of this diagram vanishes in the $d \rightarrow \infty$ limit. Only the local contribution with $i = j$ survives.

and another factor $\frac{1}{\sqrt{\mathcal{Z}_{\parallel i-j \parallel}}}$ for $\langle \hat{c}_{il}^{\sigma\dagger} \hat{c}_{jm}^{\sigma} \rangle$ which is directly connected to the Green function

$$G_{ilm}(\tau = 0+) = -\delta_{ij}\delta_{lm} + \langle \hat{c}_{il}^{\sigma\dagger} \hat{c}_{jm}^{\sigma} \rangle. \quad (22)$$

Only the scaling of Eq. [18] provides a non-trivial limit in which the interplay between kinetic and Coulomb interaction energy remains intact.

Locality of diagrams– Now, let us consider the Feynman diagram for the Green function depicted in Fig. 5. The contribution of this diagram, but generally every diagram where two sites $i \neq j$ are connected by three independent lines (\mathbf{G}_{ij}^0 's)¹ scales like $1/\sqrt{\mathcal{Z}_{\parallel i-j \parallel}}^3$ for individual i 's and j 's. This is a factor $1/\mathcal{Z}_{\parallel i-j \parallel}$ smaller than the direct contribution Eq. [19], i.e., a Green function line without interaction. Hence, such non-local diagrams for the Green function (or self energy) become *irrelevant* in the limit $\mathcal{Z}_{\parallel i-j \parallel} \rightarrow \infty$.

There are also Feynman diagrams as in Fig. 6, where $i \neq j$ are connected by only two lines. Taking into account a factor $\mathcal{Z}_{\parallel i-j \parallel}$ for the sum over different j , we see that the overall contribution of this diagram scale like $\mathcal{Z}_{\parallel i-j \parallel}^0$. However, if we write the Feynman diagrams in terms of the interacting (full) Green function \mathbf{G}_{ij} instead of the non-interacting \mathbf{G}_{ij}^0 this diagram is already contained in the *local* diagram on the right hand side of Fig. 6. This is because \mathbf{G}_{ij} includes self-energy inclusions as on the left hand side of Fig. 6.

Generally, the relation between \mathbf{G}_{ij} (double lines) and \mathbf{G}_{ij}^0 (single lines) is given by the Dyson equation which reads

$$\mathbf{G}_{ij}(\tau) = \mathbf{G}_{ij}^0(\tau) + \sum_{i'j'} \int_0^\beta d\tau' \int_0^\beta d\tau'' \mathbf{G}_{ii'}^0(\tau') \Sigma_{i'j'}(\tau'' - \tau') \mathbf{G}_{j'j}(\tau - \tau'') \quad (23)$$

¹Here and in the following, bold symbols denote matrices in the orbital index.

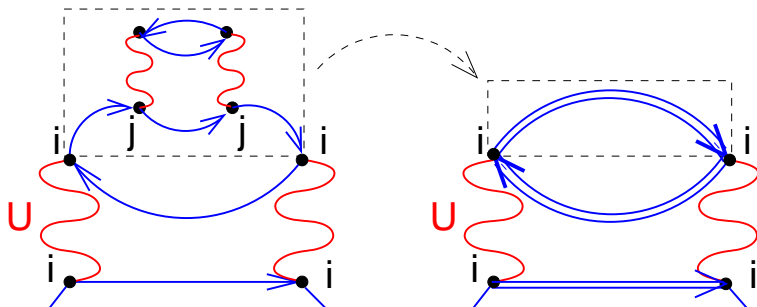
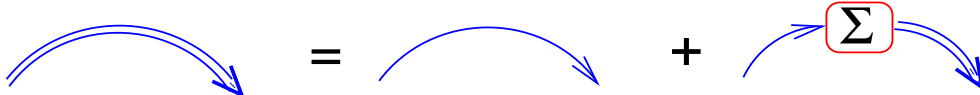


Figure 6. Left hand side: A diagram for the Green function or self energy which contributes in the $d \rightarrow \infty$ limit since i and j are connected only by two Green function lines. However, this diagram is contained in the *local* diagram on the right hand side in terms of the full (interacting) Green function (double line), since it includes interaction or self energy parts as the one on the left side. For $d \rightarrow \infty$, all (*skeleton*) diagrams in terms of the interacting Green function are *purely local*, i.e. only involve one site i .

or graphically



Fourier transformed, Eq. [23] simplifies to

$$\mathbf{G}_{\mathbf{k}}(i\omega_{\nu})^{-1} = \mathbf{G}_{\mathbf{k}}^0(i\omega_{\nu})^{-1} - \Sigma_{\mathbf{k}}(i\omega_{\nu}). \quad (24)$$

If we now write our diagrams in terms of \mathbf{G}_{ij} , we have to restrict ourselves to a subset of all Feynman diagrams, the so-called *skeleton* diagrams which do not contain any part connected to the rest of the diagram by only two \mathbf{G}_{ij} lines because such diagrams are generated if \mathbf{G}_{ij} is expanded in terms of \mathbf{G}_{ij}^0 . If these were included in the *skeleton* diagrams they would be counted twice.

How do the *skeleton* diagrams scale with $Z_{\parallel i-j \parallel}$? If there are two sites $i \neq j$, both sites have to be connected by three Green function lines (directly or indirectly via additional sites), which follows directly from the definition of the *skeleton* diagrams. Therefore, the scaling for individual sites $j \neq i$ goes at least like $1/\sqrt{Z_{\parallel i-j \parallel}}^3$ as in Fig. 5. These contributions become irrelevant for $Z_{\parallel i-j \parallel} \rightarrow \infty$. Consequently, all *skeleton* diagrams are purely local. An electron may still leave site i , interact on other sites, and return to site i retardedly. But these processes are entirely described by the local interacting Green function \mathbf{G}_{ii} , containing self energy inclusions as in Fig. 6.

As a result, the self energy itself is *purely local*:

$$\Sigma_{ij}(\omega) \xrightarrow{Z_{\parallel i-j \parallel} \rightarrow \infty} \delta_{ij} \Sigma(\omega) \quad (25)$$

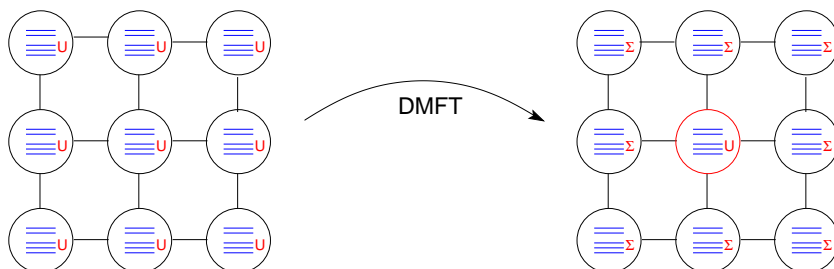


Figure 7. DMFT maps the lattice many-body problem with interactions U on every site (left side) onto a single site problem where the interaction has been replaced by the self energy Σ except for a single site (right side). All irreducible Feynman diagrams are hence local: electrons, leaving and returning to this single interacting site, are dressed by Σ (double line in Fig. 6). The DMFT mapping becomes exact for $d \rightarrow \infty$ and is an approximation in finite dimensions.

or Fourier-transformed \mathbf{k} -independent: $\Sigma_{\mathbf{k}}(\omega) = \Sigma(\omega)$. From this and the Dyson equation [23], it follows that $G_{iljm}(\omega) \sim 1/\sqrt{\mathcal{Z}_{\parallel i-j\parallel}}$, *a posteriori* confirming our assumption Eq. [20].

To conclude this scaling analysis, we can say that DMFT represents the local contribution of all *skeleton* Feynman diagrams, thereby replacing the lattice many-body problem by a local (single site) problem, see Fig. 7. This simplification becomes exact for $d \rightarrow \infty$ and is an approximation if applied to a finite dimensional problem.

Mapping onto the Anderson impurity model—Diagrammatically, DMFT corresponds to the local contribution of all topologically distinct Feynman diagrams. Exactly the same diagrams can be obtained via an Anderson impurity model if its on-site interaction has the same form as the original Hamiltonian [15]:

$$\hat{H}_{\text{AIM}} = \sum_{\mathbf{k}l\sigma} \epsilon_l(\mathbf{k}) \hat{a}_{\mathbf{k}l}^{\sigma\dagger} \hat{a}_{\mathbf{k}l}^{\sigma} + \sum_{\mathbf{k}l\sigma} [V_{lm}(\mathbf{k}) \hat{a}_{\mathbf{k}l}^{\sigma\dagger} \hat{c}_m^{\sigma} + \text{h.c.}] + \sum_{lmno\sigma\sigma'} U_{lmno} \hat{c}_l^{\sigma\dagger} \hat{c}_m^{\sigma\dagger} \hat{c}_n^{\sigma'} \hat{c}_o^{\sigma}. \quad (26)$$

Here, $\hat{a}_{\mathbf{k}l}^{\sigma\dagger}$ ($\hat{a}_{\mathbf{k}l}^{\sigma}$) are creation and annihilation operators for non-interacting conduction electrons at wave vector \mathbf{k} which have a dispersion $\epsilon_l(\mathbf{k})$ and hybridise with the localised interacting electrons $\hat{c}_m^{\sigma\dagger}$ via $V_{lm}(\mathbf{k})$.

Let us now switch to the language of functional integrals in terms of Grassmann variables ψ and ψ^* , see e.g. Ref. (95). By a simple Gaussian integration we can get rid of the conduction electrons since these only enter quadratically in Hamiltonian [26] and, hence, in the functional integral. Integrating out these conduction electrons, we arrive at an effective problem for the interacting elec-

trons $\hat{c}_m^{\sigma\dagger}$ whose Green function reads

$$G_{lm}^{\sigma}(i\omega_{\nu}) = -\frac{1}{\mathcal{Z}} \int \mathcal{D}[\psi] \mathcal{D}[\psi^*] \psi_{\nu l}^{\sigma} \psi_{\nu m}^{\sigma*} e^{\mathcal{A}[\psi, \psi^*, (\mathcal{G}^0)^{-1}]}. \quad (27)$$

Here, ν denotes imaginary Matsubara frequencies $\omega_{\nu} = \pi(2\nu + 1)/\beta$;

$$\mathcal{Z} = \int \mathcal{D}[\psi] \mathcal{D}[\psi^*] e^{\mathcal{A}[\psi, \psi^*, (\mathcal{G}^0)^{-1}]} \quad (28)$$

is the partition function and the single-site action \mathcal{A} has the form

$$\begin{aligned} \mathcal{A}[\psi, \psi^*, (\mathcal{G}^0)^{-1}] = & \sum_{\nu\sigma lm} \psi_{\nu m}^{\sigma*} [\mathcal{G}_{mn}^{\sigma 0}(i\omega_{\nu})]^{-1} \psi_{\nu n}^{\sigma} \\ & - \sum_{lmno\sigma\sigma'} U_{lmno} \int_0^{\beta} d\tau \psi_l^{\sigma*}(\tau) \psi_n^{\sigma'}(\tau) \psi_m^{\sigma'*}(\tau) \psi_o^{\sigma}(\tau). \end{aligned} \quad (29)$$

In Eq. [29], the interaction part of \mathcal{A} is in terms of τ , the Fourier transform of the Matsubara frequencies ω_{ν} . The non-interacting Green function of the effective problem is given by

$$[\mathcal{G}_{mn}^{\sigma 0}(i\omega_{\nu})]^{-1} = i\omega_{\nu} + t_{im in} + \mu - \sum_{\mathbf{k}l} \frac{V_{lm}(\mathbf{k})^* V_{ln}(\mathbf{k})}{i\omega_{\nu} + \mu - \epsilon_l(\mathbf{k})}, \quad (30)$$

with the same local term $t_{im in}$ as the original many body Hamiltonian [15].

The topology of the *irreducible* diagrams of this effective Anderson impurity model is exactly the same as the DMFT single site problem: simply the local contribution of all Feynman diagrams. If also the lines of the diagrams are the same we will hence obtain the same self energy. For the local *irreducible* diagrams, this is achieved if the interacting Green function $\mathbf{G}(\omega)$ of the Anderson impurity model also equals the local DMFT Green function $\mathbf{G}_{ii}(\omega)$.

Which Anderson impurity model has now this $\mathbf{G}(\omega)$ as its interacting Green function?¹ Given its interacting Green function $\mathbf{G}(\omega)$ and self energy $\mathbf{\Sigma}(\omega)$, the impurity model's *non-interacting* Green function \mathcal{G}^0 has to fulfil

$$[\mathcal{G}^0(\omega)]^{-1} = [\mathbf{G}(\omega)]^{-1} + \mathbf{\Sigma}(\omega). \quad (31)$$

¹Since Green function $\mathbf{G}(\omega)$ and self energy $\mathbf{\Sigma}(\omega)$ are the same for DMFT and the Anderson impurity model we employ the same symbols.

This is the analogy to the Dyson equation [23], but now for the auxiliary Anderson impurity model. Note, that if we expand the $\mathbf{G}(\omega)$ of the *irreducible* diagrams in terms of $\mathbf{G}^0(\omega)$, we will get *reducible* inclusions and all local Feynman diagrams. While the reducible diagrams for the Anderson impurity model are different from the (non-local) reducible DMFT diagrams, the irreducible diagrams are exactly the same. Hence, we can calculate the interacting DMFT Green function or self energy by solving an Anderson impurity model.

Self consistency scheme— Building upon these considerations, we can now formulate the self-consistent DMFT scheme, which is summarised in the DMFT flow diagram Fig. 8. We start with a trial self energy $\mathbf{\Sigma}(\omega)$, which might just be zero. Then, we calculate the local Green function $\mathbf{G}(\omega)$ by \mathbf{k} -integration of the Dyson equation [24]:

$$\mathbf{G}(\omega) = \frac{1}{V_{\text{BZ}}} \int_{\text{BZ}} d^3k [\omega \mathbf{1} + \mu \mathbf{1} - \epsilon(\mathbf{k}) - \mathbf{\Sigma}(\omega)]^{-1}. \quad (32)$$

Here, we have made use of $\mathbf{G}^0(\mathbf{k})^{-1} = \omega \mathbf{1} + \mu \mathbf{1} - \epsilon(\mathbf{k})$ where $\epsilon(\mathbf{k})$ is the Fourier transform of t_{iljm} like in Eq. [14], $\mathbf{1}$ the orbital unit matrix, and V_{BZ} the volume of the Brillouin zone (BZ).

Given $\mathbf{G}(\omega)$ and $\mathbf{\Sigma}(\omega)$, we define the effective non-interacting Green function of the Anderson model $\mathbf{G}^0(\omega)$ via Eq. [31]. Now comes the difficult part: We have to solve the Anderson impurity model and calculate its Green function $\mathbf{G}(\omega)$. Different methods to this end are presented in Section 5. Using Eq. [31] a second time, we obtain a new self energy. (Sometimes, in particular in perturbation theory, it is more convenient to calculate the self energy of the Anderson impurity model directly, like in our diagrammatic presentation in Section 3.1.) With this new self energy $\mathbf{\Sigma}(\omega)$, the algorithm is iterated until a convergence criterion ε in some norm $\|\dots\|$, e.g. the maximum or sum norm, is met.

3.2 Extensions of DMFT

DMFT accounts for a major, local part of electronic correlations. This part is responsible for the strong quasiparticle renormalisation and the Mott-Hubbard transition in materials with strong electronic correlations such as transition metal oxides and heavy Fermion systems, see the discussion in Section 1. But also many other physical phenomena have been described by DMFT: the crossover from Slater (96) to Heisenberg (97) antiferromagnetism (30) and associated metamagnetism (98; 99), the influence of the lattice (100; 101) and Hund's exchange on ferromagnetism (102), scattering at impurities (103; 104; 105; 106) or spins (74; 75), the effect of phonons (107; 108; 109),

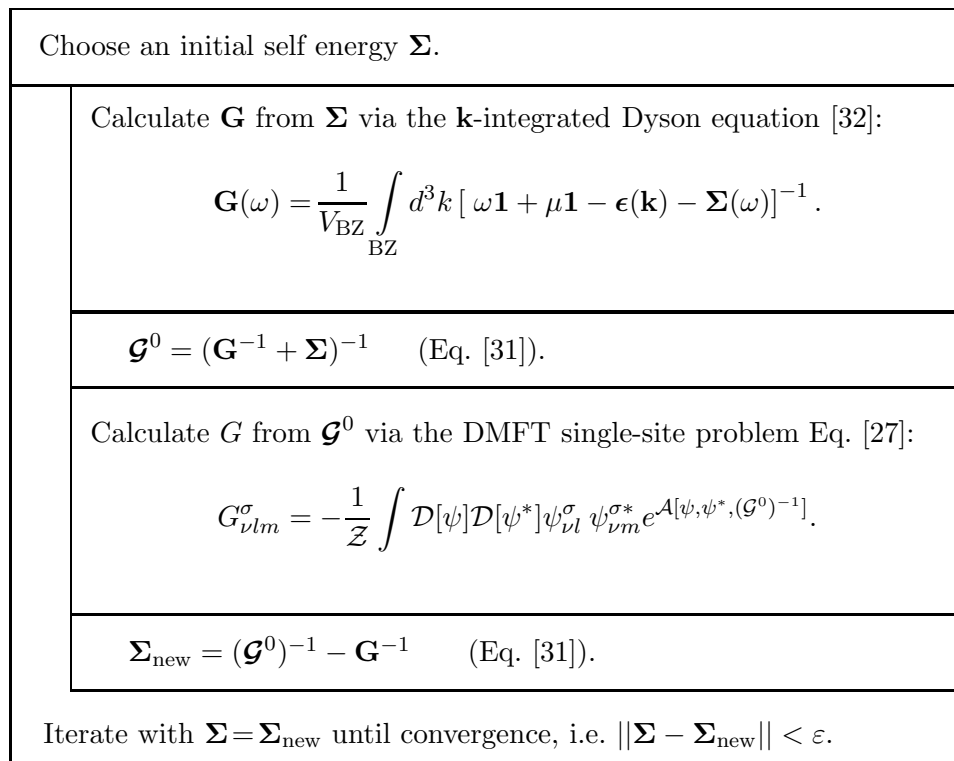


Figure 8. Flow diagram of the DMFT self-consistency cycle, also see Ref. (35).

particularly on the ‘colossal magnetoresistance’ in manganites (110; 111; 112) and superconductivity (113; 114). This list is far from complete, with only a bare minimum of references. Nonetheless, it shows that DMFT yields a wide variety of physical phenomena, posing the question: What does DMFT not describe?

What DMFT neglects completely are non-local correlations. Such non-local correlations are responsible for a variety of physical phenomena, ranging from valence bonds, pseudo gaps and (possibly) d -wave superconductivity to (para-)magnons, quantum critical behaviour, and generally the critical behaviour in the vicinity of phase transitions. All these effects are not included in DMFT. Some of these effects stem from rather short range correlations, e.g. the valence bond formation of pairs of spins into singlets; others require long-range correlations, e.g. quantum criticality.

There have been various attempts to include non-local correlations beyond DMFT. Most successfully and widely employed are cluster extensions of DMFT. Since these have been reviewed recently by Maier *et al.* (115), we

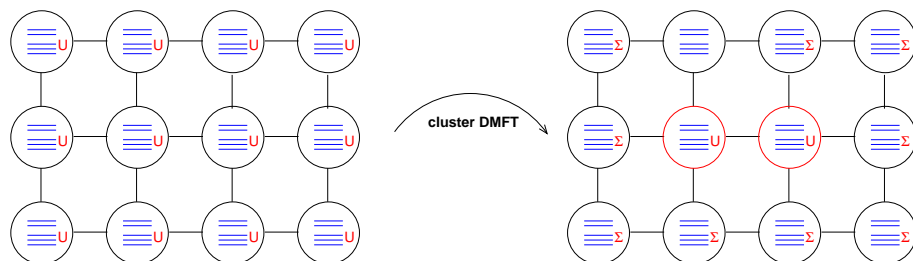


Figure 9. In cluster DMFT the lattice many-body problem (left side) is mapped onto a DMFT cluster (right hand side) which consists of several (here two) interacting sites. Nonlocal correlations between the cluster sites are taken into account. The DMFT field couples to the border of the cluster.

will only briefly discuss the basic ideas and different cluster schemes, without giving referenced to all applications to model systems.

The idea of these cluster extensions is to treat, instead of the single DMFT site, a whole cluster of sites, see Fig. 9. A natural choice for the cluster is a super cell in real space, or the LDA unit cell if it contains more than one site with interacting d or f orbitals. Then the DMFT basis block is not a single site but this super cell. Non-local correlations within the super cell are taken into account, whereas such correlations between different super cells are neglected. Beyond the local DMFT self energy, there are now also off-diagonal elements $\Sigma_{ij}(\omega)$ for two sites $i \neq j$ within the cluster. This path is followed in the so-called cluster DMFT approaches (56; 116; 117; 118). Cluster DMFT turned out to yield surprisingly precise results for the one-dimensional Hubbard model (119). With the number of cluster-sites, the numerical effort grows considerably, in particular if realistic calculations require the inclusion of several orbitals. Such realistic LDA+cluster DMFT calculation have been employed so-far by Poteryaev *et al.* (120) for studying Ti_2O_3 , by Mazurenko *et al.* (121) for NaV_2O_5 , and by Biermann *et al.* (122), who found VO_2 to be insulating because spins form non-local singlets so that a Peierls gap opens. In both cases the LDA unit cell provided for a natural choice of a two-site cluster.

Another scheme, named dynamical cluster approximation (DCA), has been proposed by Hettler *et al.* (123). While cluster DMFT can be best understood in real space, the idea of DCA is to patch the self energy in \mathbf{k} -space. To this end, the first Brillouin zone is divided into N_c patches around \mathbf{k} -vectors \mathbf{K} . In contrast to the constant DMFT self energy, the DCA self energy $\Sigma_{\mathbf{K}}$ is only constant within the patch, but varying from patch to patch. This way, \mathbf{k} -dependencies of the self energy are taken into account. The basic differences between DCA and cluster DMFT in real space are: The DCA cluster has periodic boundary conditions, whereas that of cluster DMFT has open boundary conditions. Moreover, the dynamical mean field couples to every

site of the cluster in DCA and to the boundary sites in cluster DMFT. In the limit of infinite cluster size ($N_c \rightarrow \infty$), both approaches become exact. While cluster DMFT might be more suitable for dealing with particular short-range correlations in real space, such as the formation of a spin singlet on neighbouring sites, DCA more naturally preserves translational symmetry. Let us also mention three further alternatives: the cluster perturbation theory by Gros and Valenti (124), the variational cluster perturbation theory of Potthoff *et al.* (118), and the (very general) self energy functional approach of Potthoff (125; 126). In the context of classical spin models cluster extensions such as the embedded cluster method (127) have been used for a long time, leading to early proposals (56) to employ similar approaches for DMFT.

In the DMFT context, cluster extensions have been applied extensively by now for studying superconductivity. Indeed, *d*-wave superconductivity in the two-dimensional Hubbard model was found for a 2×2 cluster (128; 117; 129), and a pseudogap phase at elevated temperatures (130). Whether the *d*-wave superconductivity persists for larger cluster sizes and in the $N_c \rightarrow \infty$ limit is however less obvious (115; 131; 132). Let us also note that Jarrell and coworkers (133; 134) employed a hybrid cluster solve for treating larger cluster sizes, where the fluctuation exchange approximation (FLEX) by Bickers *et al.* (135) is employed for longer-range correlations.

A different route to extend DMFT by non-local correlations has been proposed by Schiller and Ingersent (136; 137). The authors extended DMFT diagrammatically through all diagrams to order $1/d$. This leads to a theory with a single-site and a two-site cluster whose Green functions have to be subtracted. Necessarily, this $1/d$ approach is hence restricted to nearest neighbour correlations.

All extensions of DMFT mentioned so far, are restricted to relatively short-range correlations. Often, however, long-range correlations are of vital importance, e.g. for magnons, screening and quantum criticality. If we want to account for such long-range correlations, other extensions of DMFT are necessary. Very recently, Toschi *et al.* (138) introduced a way to do so (also see Ref. (139; 140)): the dynamical vertex approximation (D Γ A). The basic idea is to extend DMFT diagrammatically: Toschi *et al.* (138) take the local, fully irreducible two-particle vertex as a starting point and construct from this vertex all possible (local and non-local) self energy diagrams. A restriction of this approach to the particle-hole channel yields (para-)magnons, a restriction to the particle-particle channels yields the cooperon diagrams. Hence, ladder diagrams describing long-range correlations for weakly correlated systems are recovered, but with the vertex instead of the bare Coulomb interaction so that strong correlations are accounted for. Independently, Kusunose (139) extended DMFT by the transverse particle-hole channel using iterated perturbation theory, and Slezak *et al.* (140) proposed to use similar ladder diagrams for solving

larger DCA clusters. Previous attempts supplement the DMFT self energy by spin-fluctuations from the spin-fermion model (141; 142; 143; 144) or from the self-consistent renormalisation theory (145). Bolech *et al.* (146) explored the possibility of a renormalisation group extension of cluster DMFT and Rubtsov *et al.* extended DMFT by including non-local correlations through the dual Fermion approach (147; 148).

4 Merging conventional bandstructure approaches with DMFT

The standard 20th century approach to calculate materials realistically, i.e. density functional theory (DFT) in its local density approximation (LDA), was introduced in Section 2. As pointed out in Section 1, this conventional approximation does not work for materials with d or f electrons because electronic correlations are too strong. Of prime importance for these correlations are the *local* Coulomb interactions between the d or f electrons. This is because the local Coulomb interaction is the largest one and also because other density-density interactions are to leading order in $1/Z_{\parallel i-j \parallel}$ (one over the number of sites with the same distance, see Section 3) only given by the Hartree term as was proved by Müller-Hartmann (28). This Hartree term is already contained in the LDA.

In this Section, we will review recent approaches which start from the *ab initio* Hamiltonian [2] and merge conventional bandstructure approaches (Section 2) with DMFT (Section 3) in order to reliably account for the *local* correlations induced by the local Coulomb interaction. In Section 4.1, we will discuss how conventional LDA calculations are merged with DMFT, presenting two points of view: (i) a physically-motivated Hamiltonian formulation in Section 4.1.1, which can be done self-consistently as pointed out in Section 4.1.2 and whose parameters can be calculated by constrained LDA as discussed in Section 4.1.3; and (ii) in Section 4.1.4 a formulation in terms of a spectral density functional theory which appreciates the Hohenberg-Kohn (2) extremum principle for the energy. Section 4.1.5 is devoted to simplified LDA+DMFT implementations for transition metal oxides. In Section 4.2, the Hartree+DMFT and the Hartree-Fock+DMFT approach are introduced. The former is very natural from the DMFT point of view concerning non-local interactions. Section 4.2 also paves the way for the more profound alternative to LDA+DMFT which is a combination of the GW approximation and DMFT, finally addressed in Section 4.3.

4.1 LDA+DMFT

4.1.1 Hamiltonian formulation. In Section 2.3, we deduced the LDA Hamiltonian [11] from the *ab initio* Hamiltonian [2]. To account for the important *local* correlations, we will now supplement this LDA Hamiltonian [11] by the *local* Coulomb interaction. The resulting multi-band many-body problem will then be solved by DMFT. A predecessor of this LDA+DMFT approach is the so-called LDA+U method of Anisimov *et al.* (19), which constructs the same many-body problem but then solves it by (symmetry-broken) Hartree-Fock, i.e. without taking into account electronic correlations if these are defined as being beyond Hartree-Fock. As an approximate solution of the DMFT self-consistency equations we will rediscover this LDA+U scheme in Section 5.1.

In principle, one could use the most general local Coulomb interaction as in Hamiltonian [15] of Section 3 and calculate the Coulomb matrix elements by

$$U_{lmno} = \frac{e^2}{4\pi\epsilon_0} \int d^3r \int d^3r' \varphi_{il}(\mathbf{r})^* \varphi_{im}(\mathbf{r}')^* \frac{1}{|\mathbf{r} - \mathbf{r}'|} \varphi_{in}(\mathbf{r}') \varphi_{io}(\mathbf{r}). \quad (33)$$

However, this approach is not practical. First of all, it is often sufficient to take into account only the most important matrix elements of the Coulomb interaction, including only two distinct orbital indices and restricting the interaction to the localised *d* or *f* orbitals only. Another aspect which makes Eq. [33] impractical is screening: If we add an extra electron to the *d* or *f* orbitals at our local site *i*, the *sp* electrons will redistribute and, therefore, reduce the energy required to add this extra electron. Since non-local Coulomb interactions as well as local interactions between *d* and *sp* electrons are responsible for this screening process, a Hamiltonian with only a local Coulomb interaction like Eq. [15] does not describe these processes anymore. Therefore, the effective local Coulomb interaction has to be smaller (screened) than the overlap integral Eq. [33]. Presently, two methods are employed for the calculation of these screened local Coulomb interactions: the constrained LDA method in the context of LDA+DMFT and the random phase approximation (RPA) within the GW+DMFT approach. This will be discussed in more detail in Section 4.1.3 and in Section 4.3, respectively.

Set-up of the LDA+DMFT Hamiltonian—Based on these considerations, the starting point of the LDA+DMFT approach is usually the following Hamilto-

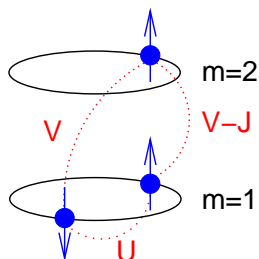


Figure 10. Pictogram of the intra- and inter-orbital repulsion U and V and the Hund exchange J for two orbitals in Hamiltonian [34].

nian, where \hat{H}_{LDA} denotes the LDA Hamiltonian [11]:

$$\begin{aligned} \hat{H} = & \hat{H}_{\text{LDA}} + U \sum_{\substack{i\sigma \\ l \in L_U}}' \hat{n}_{il}^{\sigma} \hat{n}_{il}^{\bar{\sigma}} + \sum_{\substack{i\sigma\sigma' \\ l \in L_U \neq m \in L_U}}' (V - \delta_{\sigma\sigma'} J) \hat{n}_{il}^{\sigma} \hat{n}_{im}^{\sigma'} \\ & - \frac{J}{2} \sum_{\substack{i\sigma \\ l \in L_U \neq m \in L_U}}' \hat{c}_{il\sigma}^{\dagger} \hat{c}_{il\bar{\sigma}} \hat{c}_{im\bar{\sigma}}^{\dagger} \hat{c}_{im\sigma} - \frac{\tilde{J}}{2} \sum_{\substack{i\sigma \\ l \in L_U \neq m \in L_U}}' \hat{c}_{il\sigma}^{\dagger} \hat{c}_{il\bar{\sigma}}^{\dagger} \hat{c}_{im\sigma} \hat{c}_{im\bar{\sigma}} - \sum_{\substack{i\sigma \\ l \in L_U}} \Delta\epsilon \hat{n}_{il\sigma} \end{aligned} \quad (34)$$

Here, the prime on the sum indicates that every term of the sum is counted only once; $\bar{\sigma} = \downarrow$ (\uparrow) for $\sigma = \uparrow$ (\downarrow); $\hat{n}_{il}^{\sigma} = \hat{c}_{il}^{\sigma\dagger} \hat{c}_{il}^{\sigma}$; $\delta_{\sigma\sigma'}$ denotes the Kronecker symbol. Moreover, $l \in L_U$ indicates that the interaction is only taken into account on the subset L_U of the ‘U-interacting’ orbitals in the unit cell i . For example, L_U might denote the set of d (or the t_{2g}) orbitals of a transition metal or the $4f$ orbitals of rare earth elements.

The Coulomb interaction terms consist of the intra-orbital Coulomb repulsion U , the inter-orbital Coulomb repulsion V , the Hund exchange term J and a pair-hopping term \tilde{J} , see Fig. 10. The last term of Eq. [34] describes the contribution of U , V and J already included in \hat{H}_{LDA} , which has to be subtracted to avoid a double counting. This last term led to some criticism. It arises, however, very naturally from the constrained LDA calculation, as we will discuss below. If the Coulomb interaction is the same for all orbitals, the double counting term corresponds to a simple shift of the chemical potential and has no effect. This is the case if, for example, only d orbitals are taken into account, see Section 4.1.5.

In Eq. [34], the Hund exchange has been separated into its z - z and the spin-flip components which altogether yield a $\text{SU}(2)$ symmetric contribution of the

form

$$\hat{H}_J = -2J \sum_{im} \left[\hat{s}_{im} \hat{s}_{il} + \frac{1}{4} \hat{n}_{il} \hat{n}_{im} \right] \quad (35)$$

for the coupling of the spins \hat{s}_{im} between different orbitals l, m at site i . For real-valued wave functions $\varphi_{im}(\mathbf{r})$, it immediately follows from Eq. [33] that the pair-hopping amplitude equals that of the exchange interaction: $\tilde{J} = J$. Note, that purely real wave functions can be chosen if time reversal symmetry is not broken, for example by an external magnetic field. The pair-hopping term has not yet been included in LDA+DMFT calculations because one commonly assumes that configurations are rare in which one orbital is doubly occupied while another is empty if the Hund exchange and the hopping terms are included. For quantum Monte-Carlo (QMC) simulations, the spin-flip term of the Hund exchange poses a (sign) problem (149) and has, hence, not been included in LDA+DMFT calculations with QMC as an impurity solver so far. Different ways to overcome this sign-problem are discussed in Section 5.5. These improved methods, such as the continuous time QMC, may hence allow to do such LDA+DMFT calculations in the future.

For degenerate orbitals, e.g. the t_{2g} orbitals in a cubic symmetry, Hamiltonian [34] has to be invariant under orbital rotations, necessitating $V = U - 2J$. Then, with M interacting orbitals, the average Coulomb interaction is

$$\bar{U} = \frac{U + (M-1)(U-2J) + (M-1)(U-3J)}{2M-1}. \quad (36)$$

Even if degeneracy is only fulfilled approximately one often employs $V = U - 2J$ as an approximation, which is often quite good and allows us to set up Hamiltonian [34] with only three parameters: the average Coulomb repulsion \bar{U} , the exchange interaction J and the double counting correction $\Delta\epsilon$. All these parameters can be calculated by constrained LDA, see Section 4.1.3.

After setting up the multi-band many-body Hamiltonian [34], we have to solve it. This can be done, without genuine electronic correlations, in the LDA+U approach of Anisimov *et al.* (19) or more sophisticatedly by DMFT, as in the pioneering work of Anisimov *et al.* (31) and Lichtenstein and Katnelson (32). Within DMFT, Hamiltonian [34] is mapped onto an auxiliary Anderson impurity problem with the same Coulomb interaction and an effective non-interacting Green function $(\mathcal{G}^0)^{-1} = (\mathbf{G}^{-1} + \mathbf{\Sigma})$, see Section 3. This Anderson impurity model has to be solved self-consistently together with the \mathbf{k} -integrated Dyson equation [32], relating the local Green function \mathbf{G} and self energy $\mathbf{\Sigma}$. The LDA part \hat{H}_{LDA} of Hamiltonian [34] is only entering in this Dyson equation [32]. Most conveniently, \hat{H}_{LDA} is formulated in \mathbf{k} -space

with matrix elements as in Eq. [13], and the double counting correction $\Delta\epsilon$ is included in this term:

$$\hat{H}_{\text{LDA}}^{\text{dc}} = \hat{H}_{\text{LDA}} - \sum_{i\sigma l \in L_U} \Delta\epsilon \hat{n}_{il\sigma} = \sum_{\mathbf{k}\sigma l m} \tilde{\epsilon}_{lm}^{\text{LDA}}(\mathbf{k}) c_{\mathbf{k}l}^{\sigma\dagger} c_{\mathbf{k}m}^{\sigma} \quad (37)$$

with $\tilde{\epsilon}_{lm}^{\text{LDA}}(\mathbf{k}) = \epsilon_{lm}^{\text{LDA}}(\mathbf{k}) - \delta_{lm}\Delta\epsilon \forall l \in L_U$ (for all U -interacting orbitals) and $\tilde{\epsilon}_{lm}^{\text{LDA}}(\mathbf{k}) = \epsilon_{lm}^{\text{LDA}}(\mathbf{k}) \forall l \notin L_U$ (for all non-interacting orbitals). Employing $\tilde{\epsilon}^{\text{LDA}}(\mathbf{k})$ of Eq. [37] for the \mathbf{k} -integrated Dyson equation [32], the LDA+DMFT approach consists of the following steps, see flow diagram Fig. 11:

- (i) We start with a conventional LDA calculation, as in the flow diagram Fig. 4.
- (ii) With the given density we can calculate the hopping matrix elements t_{iljm} and from these, via a Fourier transformation, the bandstructure $\epsilon_{lm}^{\text{LDA}}$.
- (iii) In a constrained LDA calculation we determine \bar{U} , J and $\Delta\epsilon$.
- (iv) This defines the Hamiltonian [34] which we solve by DMFT, see flow diagram Fig. 8. Thereby, $\tilde{\epsilon}_{lm}^{\text{LDA}}$ enters in the Dyson equation; \bar{U} and J as interaction parameters in the Anderson impurity model.
- (v) From the DMFT self energy $\Sigma(\omega)$, we can calculate a new electron density. With this, we can go back to step 2. to calculate a new LDA Hamiltonian, if we do a self-consistent LDA+DMFT calculation as will be discussed now.

4.1.2 Self-consistent LDA+DMFT calculations. In the first four steps of the LDA+DMFT scheme above, the LDA bandstructure calculation and the inclusion of electronic correlations by DMFT are performed sequentially. In general, the DMFT solution will result in changes of the electron density $\rho(\mathbf{r})$, see Eq. [38] below. The new $\rho(\mathbf{r})$ then leads to a new LDA-Hamiltonian \hat{H}_{LDA} [11] since both the Hartree term and the exchange correlation term of \hat{H}_{LDA} depend on $\rho(\mathbf{r})$. Also, the Coulomb interaction U changes and needs to be determined by a new constrained LDA calculation, resulting in a new many-body problem.

This gives an iteration scheme as in the flow diagram Fig. 11, which without Coulomb interaction reduces to the self-consistent solution of the Kohn-Sham (60) equations since $\Sigma(\omega) = 0$. A similar self-consistency scheme was employed by Savrasov and Kotliar (150) in their calculation of Pu, albeit without self-consistency for \bar{U} , and without J and $\Delta\epsilon$. The quantitative difference between non-self-consistent and self-consistent LDA+DMFT calculations depends on the change of the number of electrons in the different bands after the DMFT calculation. This change, of course, depends on the problem at hand. For example for the Ce calculation presented in Section 6.1.1, the change of the

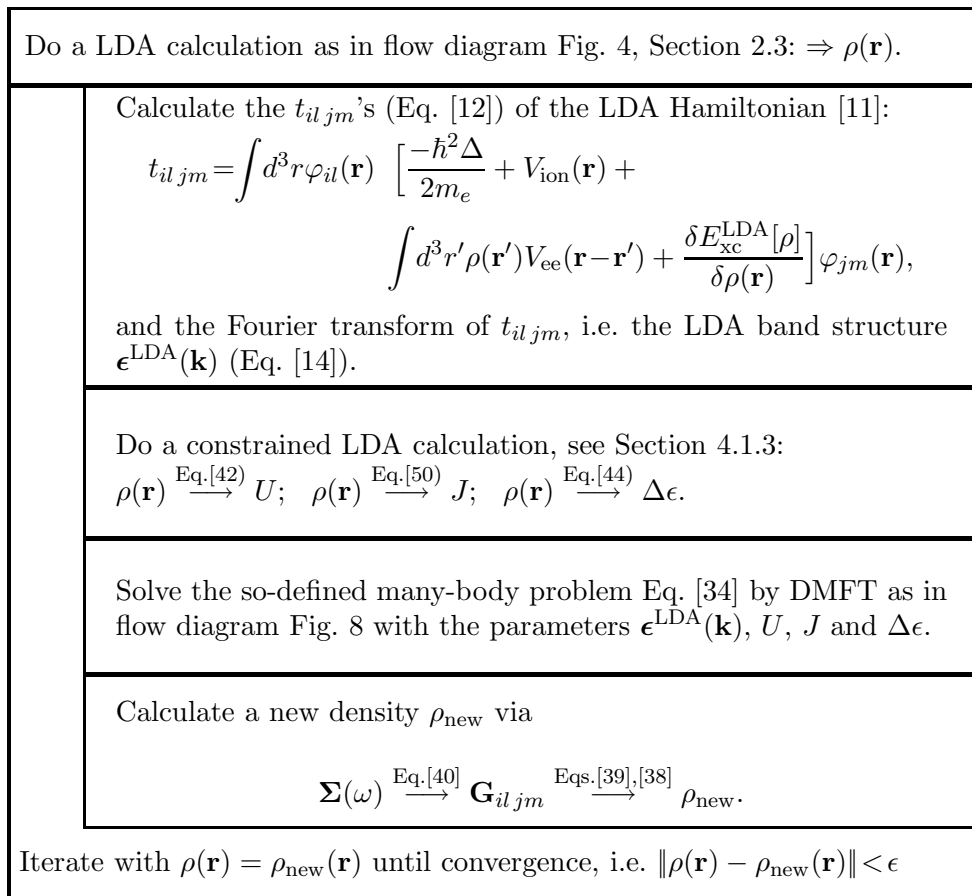


Figure 11. Flow diagram of the LDA+DMFT algorithm.

orbital occupation (from LDA to LDA+DMFT) was very minor in the vicinity of α - γ transition but more significant at lower volumes. Hence, a self-consistent LDA+DMFT calculation does not appear to be necessary in the vicinity of the Ce α - γ transition. Indeed, most LDA+DMFT calculations reported so far are not self-consistent. A notable exception is the work of Savrasov and Kotliar (150) on Pu already mentioned.

We still have to describe how to calculate the new electron density $\rho(\mathbf{r})$ after the DMFT calculation. We can relate $\rho(\mathbf{r})$ to the DMFT self energy $\Sigma(\omega)$ as follows:

Expressing $\rho(\mathbf{r})$ via an expectation value of the field operator $\hat{\Psi}^+(\mathbf{r}, \sigma)$ and

doing the basis transformation to the orbital basis set $\varphi_{il}(\mathbf{r})$ (Eq. [10]), we obtain

$$\rho(\mathbf{r}) = \sum_{\sigma} \langle \hat{\Psi}^+(\mathbf{r}, \sigma) \hat{\Psi}(\mathbf{r}, \sigma) \rangle = \sum_{\sigma il jm} \varphi_{il}^*(\mathbf{r}) \varphi_{jm}(\mathbf{r}) \langle \hat{c}_{il}^{\sigma\dagger} \hat{c}_{jm}^{\sigma} \rangle. \quad (38)$$

Here, the expectation value can be calculated from the equal-time Green function

$$G_{il jm}^{\sigma}(\tau = 0^+) = -\delta_{ij}\delta_{lm} + \langle \hat{c}_{il}^{\sigma\dagger} \hat{c}_{jm}^{\sigma} \rangle. \quad (39)$$

This Green function is, in turn, the Fourier transformation with respect to space and (imaginary) time of

$$\mathbf{G}_{\mathbf{k}}^{\sigma}(i\omega_{\nu}) = [i\omega_{\nu}\mathbf{1} + \mu\mathbf{1} - \tilde{\epsilon}^{\text{LDA}}(\mathbf{k}) - \Sigma(i\omega_{\nu})]^{-1}; \quad (40)$$

(bold symbols denote matrices in the orbital index). In principle, the frequency dependent DMFT self energy $\Sigma(i\omega_{\nu})$ and the \mathbf{k} -dependent LDA $\tilde{\epsilon}(\mathbf{k})$ can be spin-dependent. In the present presentation however, such a possible spin-dependence is not taken into account. We also have not discussed the peculiarities of the LDA basis set; rather we assume that the LDA Hamiltonian has been calculated in an appropriate basis set with sufficiently localised orbitals. For the self-consistent LDA+DMFT calculation, this basis set should also be optimised again with the new LDA+DMFT density $\rho(\mathbf{r})$.

A remark: Since the solution of the DMFT Anderson impurity model is often the computationally most expensive task, it might be a good idea to do only one DMFT iteration for every iteration loop in the flow diagram Fig. 11. When converged, this will produce the same result as a scheme in which, for *every* new $\rho(\mathbf{r})$, the DMFT equations are iterated until convergence. One might also omit the initial LDA loop. However, we would expect that the overall numerical effort grows.

4.1.3 Constrained LDA calculations of the interaction parameters. The task of calculating \bar{U} , J and $\Delta\epsilon$ in Hamiltonian [34] is not at all trivial as pointed out on p. 26 and requires additional approximations. Such an approximation, which works in practice and gives very reasonable values for the screened Coulomb interaction, is the constrained LDA method by Dedrichs *et al.* (151), McMahan *et al.* (152) and Gunnarsson *et al.* (153). Hence, constrained LDA allowed us to perform parameter-free, i.e. truly *ab initio*, LDA+DMFT calculations for transition metal oxides and f electron systems, yielding results in good agreement with experiment (154; 155).

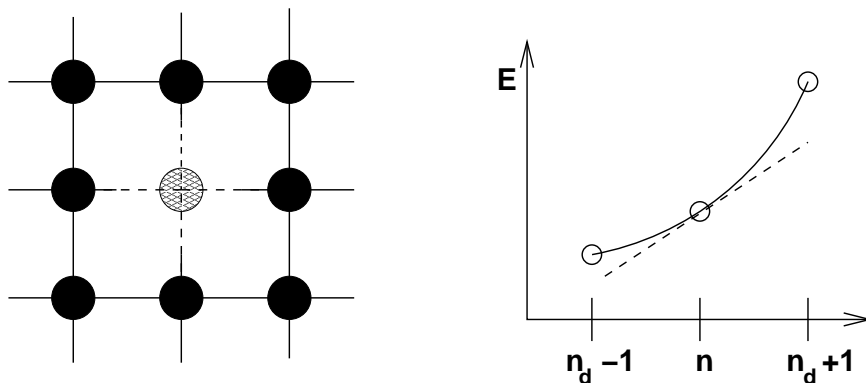


Figure 12. Left: In the constrained LDA calculation the interacting d or f electrons on one lattice site are kinetically decoupled from the rest of the system, i.e. they cannot hop to other lattice sites. By contrast, the *non*-interacting electrons can still hop to other sites (indicated by dashed lines) and screen the d or f electrons. Right: This allows us to change the number n_d of interacting d or f electrons on the decoupled site and to calculate the corresponding LDA energies $E(n)$ [circles]; the *interacting* Hamiltonian Eq. [34] reproduces these constrained LDA energies if \bar{U} and $\Delta\epsilon$ are set properly; the dashed line sketches the behaviour of \hat{H}_{LDA} defined in Eq. [11].

The basic idea of constrained LDA is to do LDA calculations for a slightly modified problem, i.e. a problem where the interacting d or f electrons of one site are kinetically decoupled from the rest of the system. This is achieved by setting the hopping matrix elements between these localised orbitals l on site i and all other orbitals to zero: $t_{iljm} = 0 \forall j, m$, see Fig. 12. This allows us to change the number of interacting electrons on this decoupled site; they cannot hop away. At the same time, screening effects of the other electrons are taken into account, since they redistribute if the number of d or f electrons is changed on the decoupled site.

Usually, we know how many d or f electrons n_d to expect, for example, from the formal oxidation, and typically n_d is close to an integer number. Then, we can do constrained LDA calculations for $n_d - 1$, n_d , and $n_d + 1$ electrons on the decoupled site within the interacting orbitals ($l \in L_U$). This leads to three corresponding total energies, see Fig. 12. The LDA Hamiltonian \hat{H}_{LDA} which was calculated at a fixed density $\rho(\mathbf{r})$, see Section 2.3, would predict a linear change of the LDA energy with the number of interacting electrons, i.e. $E(n_d) = E_0 + \epsilon_d^{\text{LDA}} n_d$. This linear behaviour does not take into account the Coulomb interaction \bar{U} which requires a higher energy cost to add the $(n + 1)$ th electron than to add the n th electron. This effect leads to the curvature in Fig. 12 and is taken into account in the Hamiltonian [34] which yields for $J = 0$:

$$E(n_d) = E_0 + \frac{1}{2} \bar{U} n_d (n_d - 1) + (\epsilon_d^{\text{LDA}} + \Delta\epsilon) n_d. \quad (41)$$

Here, ϵ_d^{LDA} is the energy contribution of \hat{H}_{LDA} in Eq. [34] for d or f orbitals on the decoupled site. If m denotes the (degenerate) d or f orbital this contribution is given by the diagonal hopping matrix element (Eq. [11]): $\epsilon_d^{\text{LDA}} \equiv t_{imim}$ (if so, orbitally averaged). Note that all hopping elements t_{imjl} to other orbitals and sites are set zero in the truncated problem of the constrained LDA. Since the n_d electrons are kinetically decoupled from the rest of the system, we can calculate the interaction energy in Eq. [41] directly from the number of n_d electrons.¹ Note that part of $\Delta\epsilon$ just arises to cancel the Coulomb contribution $(1/2) d[\bar{U}n_d(n_d - 1)]/dn_d = \bar{U}(n_d - 1/2)$.

Knowing how the energy $E(n)$ changes when going from $n_d - 1$ to n_d and $n_d + 1$ electrons allows us to determine \bar{U} and $\Delta\epsilon$ since there are two parameters and two energy differences. In the actual calculation, we obtain these energy differences from the constrained LDA eigenlevels of the decoupled d or f orbitals, using the relation $\epsilon_d(n_d) = \frac{dE(n_d)}{dn_d}$ (156; 157). From this we directly determine

$$\begin{aligned}\bar{U} &= E(n_d + 1) + E(n_d - 1) - 2E(n_d) \\ &\approx \epsilon_d(n_d + \frac{1}{2}) - \epsilon_d(n_d - \frac{1}{2}).\end{aligned}\quad (42)$$

$\Delta\epsilon$ is obtained from the energy difference to add a single electron. Eq. [41] yields

$$E(n_d) - E(n_d - 1) = \bar{U}(n_d - 1) + (\epsilon_d^{\text{LDA}} + \Delta\epsilon) \quad (43)$$

so that

$$\begin{aligned}\epsilon_d^{\text{LDA}} + \Delta\epsilon &= E(n_d) - E(n_d - 1) - \bar{U}(n_d - 1) \\ &\approx \epsilon_d(n_d - \frac{1}{2}) - \bar{U}(n_d - 1).\end{aligned}\quad (44)$$

This shift of the d or f eigenlevel can be taken into account by replacing $\epsilon_d^{\text{LDA}} = t_{imim}$ in \hat{H}_{LDA} [34] by the term $\epsilon_d(n_d - \frac{1}{2}) - \bar{U}(n_d - 1)$ from the constrained LDA calculation. This replacement thus includes $\Delta\epsilon$ in \hat{H}_{LDA} .

With this procedure, we guarantee that Hamiltonian [34] correctly reproduces the constrained LDA energies for the truncated problem where hopping from and to the localised d or f orbitals onto one site i is forbidden. It is slightly different from the approach by Anisimov *et al.* (19) who directly related the

¹Operators $\sum_m \hat{n}_m$ stay constant all the time and can be replaced by this constant, i.e. n_d .

double counting correction to \bar{U} :

$$\Delta\epsilon = \bar{U}(n_d - \frac{1}{2}). \quad (45)$$

A third path has been proposed by Lichtenstein *et al.* (158; 36), identifying an orbital-dependent term

$$\Delta\epsilon_m = \frac{1}{2} \sum_{\sigma} \Sigma_{mm}^{\sigma}(\omega = 0). \quad (46)$$

A cautionary remark: While the total LDA spectrum is rather insensitive to the choice of the basis, the constrained LDA calculations of \bar{U} depend more strongly on the shape of the orbitals which are considered to be interacting, e.g. the d or f orbitals. For example, in the case of LaTiO₃ at a Wigner-Seitz radius of 2.37 a.u. (atomic units) for Ti, a LMTO-ASA calculation by Nekrasov *et al.* (159) using the TB-LMTO-ASA code (160) yielded $\bar{U} = 4.2$ eV while a ASA-LMTO calculation within the orthogonal representation by Solovyev *et al.* (161) gave $\bar{U} = 3.2$ eV. Thus, an appropriate basis is mandatory, and, even then, a significant uncertainty in \bar{U} remains. For conventional LDA bandstructure calculations, the choice of basis is not so crucial since with a large enough basis set the same bandstructure $\epsilon^{\text{LDA}}(\mathbf{k})$ will be obtained. In this respect, LDA+DMFT is more challenging since it now becomes important for which orbitals the Coulomb interaction is taken into account.

Similarly as \bar{U} , the Hund exchange J can be obtained from constrained LDA calculations. Instead of the number of electrons, however, the spin-polarisation has to be changed. Since the electrons within the interacting orbitals on our decoupled lattice site cannot hop, we can change the number of $n_{d\uparrow}$ and $n_{d\downarrow}$ electrons, while keeping $n_d = n_{d\uparrow} + n_{d\downarrow}$ fixed. Then the Coulomb repulsion \bar{U} will not be affected, but nonetheless $E(n_{d\uparrow}, n_{d\downarrow} = n_d - n_{d\uparrow})$ will change because of the Hund rule exchange. Instead of the change of the total energy with $n_{d\uparrow}$, we can, as in Eq. [42], use the now spin-dependent energy levels $\epsilon_{d\sigma}(n_{d\sigma}, n_{d\bar{\sigma}}) = \frac{dE(n_{d\sigma}, n_{d\bar{\sigma}})}{dn_{d\sigma}}$. From this Anisimov *et al.* (19) determine J as

$$J_{\text{cLDA}} = \epsilon_{d\uparrow}(n_{d\uparrow} = \frac{n_d}{2} + \frac{1}{2}, n_{d\downarrow} = \frac{n_d}{2} - \frac{1}{2}) - \epsilon_{d\downarrow}(n_{d\uparrow} = \frac{n_d}{2} + \frac{1}{2}, n_{d\downarrow} = \frac{n_d}{2} - \frac{1}{2}). \quad (47)$$

Taking such a value of J , Anisimov *et al.* (19) assume that the Hund exchange enters via a term

$$\hat{H}_J = -J \sum_{l \in L_U \neq m \in L_U \sigma} \hat{n}_{l\sigma} \hat{n}_{m\sigma}. \quad (48)$$

Nature and the LDA+DMFT Hamiltonian [34] are, however, different. As depicted in Fig. 10, the Hund exchange also influences the difference between inter-orbital and intra-orbital Coulomb interaction, given by $V = U - 2J$ in Hamiltonian [34]. This goes beyond Eq. [48] which only gives a reduction of the inter-band interaction for two spin aligned electrons.

For example, let us consider the case of a V^{3+} ion in a cubic crystal field. Then we have two d electrons ($n_d = 2$) in three degenerate t_{2g} orbitals. These two electrons can be spin aligned or not. For Hamiltonian [48], the energy difference between these two configurations is simply

$$E(n_{d\uparrow} = 2, n_{d\downarrow} = 0) - E(n_{d\uparrow} = n_{d\downarrow} = 1) = J. \quad (49)$$

In contrast, the difference also depends on the orbital configuration for the LDA+DMFT Hamiltonian (Eq. [34]). For the configuration ($n_{d\uparrow} = 2, n_{d\downarrow} = 0$), the two electrons have to be in different orbitals and their energy is $V - J = U - 3J$. For the configuration ($n_{d\uparrow} = 1, n_{d\downarrow} = 1$) and without the spin-flip term, we have the possibility that the two electrons are in the same orbital with $E(n_{d\uparrow} = n_{d\downarrow} = 1) = U$ or in different orbitals with $E(n_{d\uparrow} = n_{d\downarrow} = 1) = V = U - 2J$. Averaging over the (unknown) orbital configurations, this yields an average value $E(n_{d\uparrow} = n_{d\downarrow} = 1) = U - 4/3J$. Hence, we have

$$E(n_{d\uparrow} = 2, n_{d\downarrow} = 0) - E(n_{d\uparrow} = n_{d\downarrow} = 1) = \frac{5}{3}J \quad (50)$$

for Hamiltonian [34] if the spin-flip and pair-hopping term are not taken into account.

For example, the constrained LDA calculation by Solovyev *et al.* (161) yields a value of $J_{\text{CLDA}} = 0.93 \text{ eV}$ for V^{3+} . To reproduce this result with Hamiltonian Eq. [34], the left hand side of Eq. [50] has to be 0.93 eV and, therefore, the parameter J in Eq. [50] has to be $J = 3/5 \cdot 0.93 \text{ eV} = 0.56 \text{ eV}$. Such a reduced value of the Hund exchange coupling is also more reasonable when we compare it with the atomic value of $J = 0.689 \text{ eV}$ which is precisely measurable from the atomic spectrum¹, see Table 1. In particular, note that it is implausible

¹How to extract the Racah parameters from the atomic spectra is discussed e.g. by Griffith (162). He arrives at the following fit formulas for the Racah parameters B and C :

$$B = \frac{3}{50}[E(^3P) - E(^3F)] + \frac{1}{70}[E(^1G) - E(^1D)] \quad (51)$$

$$C = \frac{1}{350}[21E(^3F) - 84E(^3P) + 40E(^1G) + 37E(^1D) + 28E(^1S)] \quad (52)$$

where $E(X)$ denotes the energy of the atomic state X . Looking up these atomic energies for the vanadium $3d^2$ configurations at the NIST Atomic Spectra data base (http://physics.nist.gov/cgi-bin/AtData/main_asd, which stem in turn from the overview ar-

constrained LDA J_{CLDA}	$J = \frac{3}{5}J_{\text{CLDA}}$	atomic value
0.9 eV	0.6 eV	0.7 eV

Table 1. Hund exchange for a V^{3+} ion as calculated by constrained LDA, corrected value for Eq. [34] and the atomic value from Suga and Corliss (163).

that the Hund exchange is larger than the atomic value since we expect that screening effects reduce J in the crystal.

Similarly, the constrained LDA J_{CLDA} has to be corrected by $J = \frac{3}{10}J_{\text{CLDA}}$ for $n_d = 3$ before it is included in Hamiltonian Eq. [34]. These two factors determine all correction factors for the exchange coupling J between t_{2g} orbitals because of the unimportance of J for $n_d = 1$ and because particle hole symmetry gives the same correction factors for $n_d = 4$ and 5 as for $n_d = 2$ and 1, respectively.

4.1.4 Spectral density functional theory formulation. Our previous derivation of the LDA+DMFT method was physically motivated. We started from the assumption that the Kohn-Sham equations, i.e. the LDA part, yield the correct results for the weakly correlated s or p bands, while the DMFT-part takes into account the local Coulomb interactions of the strongly correlated d or f bands. Let us now consider an alternative way to formulate the LDA+DMFT method as a *spectral density functional theory*, which goes back to Chitra and Kotliar (164) and Savrasov *et al.* (165; 150), for more information also see Ref. (37) and Ref. (36) and particularly the recent review by Kotliar *et al.* (40). The basic idea is to replace the Hohenberg-Kohn (2) DFT functional $E[\rho]$ by an energy functional $E[\rho, \mathbf{G}]$ which depends on the electron density $\rho(\mathbf{r})$ and the local Green function $G_{ilim}(\omega)$ of the interacting orbitals ($m, l \in L_U$). Since the local Green function is related to the \mathbf{k} -integrated spectrum Savrasov *et al.* (165; 150) coined the name *spectral density functional theory*.

As a starting point let us take the standard Luttinger-Ward (166) many-body functional, which in compact form (suppressing site i , orbital l , spin σ and Matsubara frequency ω_ν indices) reads

$$\Omega[\Sigma, G] = \Phi[G] - \text{Tr} \Sigma G - \text{Tr} \ln((G^0)^{-1} - \Sigma). \quad (53)$$

Here Tr denotes the trace ($\frac{1}{\beta} \sum_{\nu i l \sigma}$) and $\Phi[G]$ the full set of two-particle irreducible diagrams with lines G and without external legs. From the stationary

ticle by Sugar and Corliss (163)), we obtain $B = 0.1085 \text{ eV}$ and $C = 0.4181 \text{ eV}$ so that the Hund exchange coupling is $J = \frac{5}{2}B + C = 0.689 \text{ eV}$ for the free atom.

conditions

$$\frac{\delta\Omega[\Sigma, G]}{\delta G} = 0 \quad (54)$$

we obtain the diagrammatic representation of the self energy:

$$\Sigma = \frac{\delta\Phi[G]}{\delta G}. \quad (55)$$

The second stationary condition

$$\frac{\delta\Omega[\Sigma, G]}{\delta\Sigma} = 0 \quad (56)$$

yields the usual Dyson equation, i.e. Eq. [32] without \mathbf{k} integration:

$$G = [(G^0)^{-1} - \Sigma]^{-1}. \quad (57)$$

Such a construction is then a ‘conserving approximation’ in the sense of Baym and Kadanoff (167; 168). On the basis of this functional theory, albeit with a purely local Green function and self energy, Janiš (169; 170) formulated a generalised coherent potential approximation (CPA), and Janiš and Vollhardt (77) the DMFT self-consistency approach.

On the other hand, DFT was also formulated as an effective action by Fukuda *et al.* (171; 172). Now, the electron density $\rho(\mathbf{r})$ plays the role of the Green function G in Eq. [53], and the Kohn-Sham potential $V_{\text{KS}}(\mathbf{r})$ replaces the self energy. In terms of these variables, the DFT functional reads

$$\begin{aligned} \Omega_{\text{DFT}}[V_{\text{KS}}, \rho] = & \int d^3r V_{\text{ion}}(\mathbf{r})\rho(\mathbf{r}) + \frac{1}{2} \int d^3r d^3r' \frac{\rho(\mathbf{r})\rho(\mathbf{r}')}{|\mathbf{r} - \mathbf{r}'|} + E_{\text{xc}}[\rho] \\ & - \int d^3r V_{\text{KS}}(\mathbf{r})\rho(\mathbf{r}) - \text{Tr} \ln[i\omega_\nu + \hbar^2/2m_e\Delta - V_{\text{KS}}(\mathbf{r})]. \end{aligned} \quad (58)$$

Here, the first line corresponds to the many-body functional $\phi[G]$ which is now given by the ionic potential, the Hartree and the exchange correlation term; Tr denotes again the trace (now w.r.t. the operator following and any basis, e.g. the $|\mathbf{r}\rangle$ basis) as well as the sum over Matsubara frequencies as before.

Minimisation of the functional w.r.t. ρ , i.e. $\delta\Omega_{\text{DFT}}[\rho, V_{\text{KS}}]/\delta\rho = 0$, reproduces the correct form the Kohn-Sham potential in the Kohn-Sham equation

[6],

$$V_{\text{KS}}(\mathbf{r}) = V_{\text{ion}}(\mathbf{r}) + \int d^3r' V_{\text{ee}}(\mathbf{r}-\mathbf{r}')\rho(\mathbf{r}') + \frac{\delta E_{\text{xc}}[\rho]}{\delta \rho(\mathbf{r})}, \quad (59)$$

in analogy to Eq. [55] which gives the correct form of the self energy. The second minimisation, $\delta \Omega_{\text{DFT}}[\rho, V_{\text{KS}}]/\delta V_{\text{KS}} = 0$, gives the Kohn-Sham equation [6] itself if $V_{\text{KS}}(\mathbf{r})$ is replaced by the right hand side of Eq. [59], which of course is guaranteed if self-consistency is obtained. More precisely, it yields $\rho(\mathbf{r})$ directly, expressed via the Kohn-Sham equation:

$$\rho(\mathbf{r}) = \frac{1}{\beta} \sum_{\nu} \left\langle \mathbf{r} \left| [i\omega_{\nu} + \hbar^2/2m_e\Delta - V_{\text{KS}}]^{-1} \right| \mathbf{r} \right\rangle. \quad (60)$$

In the case of LDA+DMFT, we have to deal with a mixed representation in terms of the density $\rho(\mathbf{r})$ (LDA) and the local Green function of the interacting orbitals $\mathbf{G}(\omega)$ (DMFT). Savrasov *et al.* Ref. (165; 150) constructed such a functional:

$$\begin{aligned} \Omega[\Sigma, \mathbf{G}, V_{\text{KS}}, \rho] = & \int d^3r V_{\text{ion}}(\mathbf{r})\rho(\mathbf{r}) + \frac{1}{2} \int d^3r d^3r' \frac{\rho(\mathbf{r})\rho(\mathbf{r}')}{|\mathbf{r}-\mathbf{r}'|} + E_{\text{xc}}[\rho] \\ & - \Phi[\mathbf{G}] - \Phi_{\text{dc}}[\mathbf{G}] \\ & - \int d^3r V_{\text{KS}}(\mathbf{r})\rho(\mathbf{r}) - \text{Tr} \Sigma(i\omega_{\nu})\mathbf{G}(i\omega_{\nu}) \\ & - \text{Tr} \ln [i\omega_{\nu} + \hbar^2/2m_e\Delta - V_{\text{KS}} - \Sigma(i\omega_{\nu})_{lm} \varphi_{il}^*(\mathbf{r}') \varphi_{im}(\mathbf{r})] \end{aligned} \quad (61)$$

Here, $\Sigma(i\omega_{\nu})_{lm} \varphi_{il}^*(\mathbf{r}') \varphi_{im}(\mathbf{r})$ is the transformation of the local orbital self energy to the real space formulation in terms of \mathbf{r} and \mathbf{r}' , and $\Phi_{\text{dc}}[\mathbf{G}]$ is an additional double counting correction term.

In the spirit of Hohenberg and Kohn (2), we are looking for the density $\rho(\mathbf{r})$ and the local Green function $\mathbf{G}(\omega)$ at which the functional [61] takes its minimum. (The minimisation w.r.t. Σ and V_{KS} gives two additional equations, defining Σ and V_{KS} .) The minimisation procedure yields the exact ground state energy, density and local Green function if $E_{\text{xc}}[\rho]$ and $\Phi[\mathbf{G}(\omega)]$ are themselves the exact ones. However, we do not know these exact $E_{\text{xc}}[\rho]$ and $\Phi[\mathbf{G}(\omega)]$ and have to use approximations. LDA+DMFT is one such approximation where we replace $E_{\text{xc}}[\rho]$ by the LDA exchange-correlation energy $E_{\text{xc}}^{\text{LDA}}[\rho]$ and $\Phi[\mathbf{G}(\omega)]$ by all local two-particle irreducible diagrams, i.e. the DMFT diagrams $\Phi_{\text{DMFT}}[\mathbf{G}(\omega)]$. The double counting term $\Phi_{\text{dc}}[\mathbf{G}]$ will have one of the forms discussed in Section 4.1.3.

With this LDA+DMFT approximation of the spectral density functional [61], we recover the LDA+DMFT equations formulated earlier in this Section:

- The DMFT self energy $\Sigma(\omega)$ minus the double counting correction term is obtained from

$$\frac{\delta\Omega[\Sigma, \mathbf{G}, V_{\text{KS}}, \rho]}{\delta\mathbf{G}} = \frac{\delta\Phi_{\text{DMFT}}[\mathbf{G}]}{\delta\mathbf{G}} - \Sigma - \frac{\delta\Phi_{\text{dc}}[\mathbf{G}]}{\delta\mathbf{G}} = 0. \quad (62)$$

- From

$$\frac{\delta\Omega[\Sigma, \mathbf{G}, V_{\text{KS}}, \rho]}{\delta\Sigma} = 0 \quad (63)$$

and expressing $-\hbar^2/2m_e\Delta + V_{\text{KS}}$ in the basis $\varphi_{il}(\mathbf{r})$, i.e. replacing it by the orbital matrix (the LDA bandstructure) $\epsilon^{\text{LDA}}(\mathbf{k})$ defined via Eq. [14], we obtain the Dyson equation:

$$\mathbf{G}(\mathbf{k}, i\omega_\nu) = [i\omega_\nu - \epsilon^{\text{LDA}}(\mathbf{k}) - \Sigma(i\omega_\nu)]^{-1} \quad (64)$$

- Similarly,

$$\frac{\delta\Omega[\Sigma, \mathbf{G}, V_{\text{KS}}, \rho]}{\delta V_{\text{KS}}} = 0 \quad (65)$$

yields the Kohn-Sham equations, or more precisely, $\rho(\mathbf{r})$ expressed through the Kohn-Sham equations as in Eq. [60], as in Eq. [60] but now with the self energy included:

$$\rho(\mathbf{r}) = \frac{1}{\beta} \sum_{\nu} \left\langle \mathbf{r} \left| [i\omega_\nu + \hbar^2/2m_e\Delta - V_{\text{KS}} - \Sigma(i\omega_\nu)]_{lm} \varphi_{il}^*(\mathbf{r}') \varphi_{im}(\mathbf{r}) \right|^{-1} \right| \mathbf{r} \rangle. \quad (66)$$

This equation can also be formulated in the orbital basis $\varphi_{il}(\mathbf{r})$ instead of the real space basis $|\mathbf{r}\rangle$.

- Finally, the correct form of the Kohn-Sham potential follows from

$$\frac{\delta\Omega[\Sigma, \mathbf{G}, V_{\text{KS}}, \rho]}{\delta\rho} = 0 \quad (67)$$

as before.

Let us not forget to mention a conceptional deficiency of spectral density functional theory (or LDA+DMFT) compared with standard DFT: What we define as local and interacting in DMFT is basis dependent. Different basis sets

will hence produce different results, unless more and more orbitals are considered as interacting in DMFT and more and more non-local correlations are taken into account. This poses the so-far open question: What is the optimal basis set for LDA+DMFT?

4.1.5 Simplifications for transition metal oxides with well separated e_g and t_{2g} bands. Many transition metal oxides are cubic perovskites, often with a slight distortion of the ideal cubic crystal structure. In these systems, the cubic crystal field of the oxygen ions splits the d -orbitals into three degenerate t_{2g} and two degenerate e_g orbitals. This splitting is often so strong that the t_{2g} or e_g bands at the Fermi energy are rather well separated from all other bands. For the low energy physics, it is hence sufficient to take only those bands into account which cross the Fermi energy, e.g. the three t_{2g} bands. Note that these effective bands at the Fermi energy are not purely of d character. These are the effective bands corresponding to the LDA eigenenergies. Hence, they also contain contributions of the other orbitals, in particular the oxygen p orbitals due to hybridisation effects.

From a conventional LDA bandstructure calculation, these effective low-energy bands can be accurately determined via the NMTO downfolding approach of Andersen *et al.* (46; 47) or the projection to Wannier orbitals (49).

If the transition metal oxide is cubic or only slightly distorted, a further simplification can be employed for the (almost) degenerate bands at the Fermi energy: Instead of the full LDA Hamiltonian \hat{H}_{LDA} in Eq. [34] only the total DOS of the low-lying bands needs to be taken into account within DMFT: Without symmetry breaking, the Green function and the self energy of these bands remain degenerate, i.e. $G_{lm}(\omega) = G(\omega)\delta_{lm}$ and $\Sigma_{lm}(\omega) = \Sigma(\omega)\delta_{lm}$ for $l, m \in L_U$ (i.e. the interacting orbitals at the Fermi energy). Downfolding to a basis with these degenerate L_U bands results in an effective Hamiltonian $H_{\text{LDA}}^{\text{eff}}$ or a corresponding $\tilde{\epsilon}^{\text{LDA}}(\mathbf{k})$. From this reduced Hamiltonian, the diagonal element of the Green function is calculated via

$$G(\omega)\mathbf{1} = \frac{1}{V_B} \int d^3k [\omega\mathbf{1} + \mu\mathbf{1} - \tilde{\epsilon}(\mathbf{k}) - \Sigma(\omega)\mathbf{1}]^{-1}. \quad (68)$$

Due to the diagonal structure of the self energy, the degenerate interacting Green function can be expressed via the non-interacting Green function $G^0(\omega)$:

$$G(\omega) = G^0(\omega - \Sigma(\omega)) = \int d\epsilon \frac{N^0(\epsilon)}{\omega - \Sigma(\omega) - \epsilon}. \quad (69)$$

Thus, it is possible to use the Hilbert transformation of the unperturbed LDA-calculated density of states (DOS) $N^0(\epsilon)$, i.e. Eq. [69], instead of the Dyson

equation (Eq. [32]) with the full Hamilton matrix $\epsilon^{\text{LDA}}(\mathbf{k})$. This simplifies the calculations considerably. With Eq. [69] also some conceptual simplifications arise: (i) the subtraction of the double counting correction $\Delta\epsilon$ only results in an (unimportant) shift of the chemical potential in Eq. [69] and, thus, the exact form of $\Delta\epsilon$ is irrelevant; (ii) the theorem of Müller-Hartmann (66) of a fixed spectral function at the Fermi energy holds within a Fermi liquid; (iii) as the number of electrons within the different bands is fixed, a self-consistent LDA+DMFT calculation (step 5 in Section 4.1.1) is dispensable. If the distortion from the cubic symmetry is only weak or if the off-diagonal elements of $\epsilon^{\text{LDA}}(\mathbf{k})$ are small, a slight modification of Eq. [69] can be used:

$$G_{mm}(\omega) = G^0(\omega - \Sigma(\omega)) = \int d\epsilon \frac{N_m^0(\epsilon)}{\omega - \Sigma_{mm}(\omega) - \epsilon} \quad (70)$$

which now depends on the orbitals, albeit neglecting the orbital admixture.

It should also be noted that the approximation Eq. [69] is justified only if the overlap between the t_{2g} orbitals and the other orbitals is rather weak.

4.2 Hartree+DMFT and Hartree-Fock+DMFT

Within the concept of DMFT, a combined Hartree+DMFT approach is a very natural approximation, since the non-local (density-density) Coulomb interaction U_{ij} enters only via the Hartree (173) term in the $d \rightarrow \infty$ limit (28): There are $Z_{\parallel i-j \parallel}$ equivalent U_{ij} terms so that U_{ij} has to scale like $1/Z_{\parallel i-j \parallel}$ in order that the Hartree energy contribution stays finite. This is exactly the analogy to the Weiss (174) mean field theory for spin models, in which the summed contribution of the neighbouring sites gives an effective Weiss field $h_i^{\text{Weiss}} = \sum_{j \neq i} J_{ij} \langle \hat{S}_j \rangle$ so that the proper scaling is $J_{ij} \sim 1/Z_{\parallel i-j \parallel}$.

Consequently, other contributions scale at least like $1/\sqrt{Z_{\parallel i-j \parallel}}$. For the Fock term, i.e. Fig. 13 (right), this scaling is obvious since there is one Green function $\mathbf{G}_{ij} \sim 1/\sqrt{Z_{\parallel i-j \parallel}}$ connecting i and j .¹ Note that Si and Smith (175; 176) and Chitra and Kotliar (177; 178) employed a different scaling $U_{ij} \sim 1/\sqrt{Z_{\parallel i-j \parallel}}$ in the so-called extended DMFT, also see Ref. (179). This scaling results in additional diagrams, but requires to treat the Hartree term separately since it would otherwise diverge.

The reader might think of the Hartree+DMFT approach as a special case of LDA+DMFT, in which the LDA exchange and correlation potential $E_{\text{xc}}[\rho] =$

¹The general way of such scaling arguments was elaborated in Section 3.1.

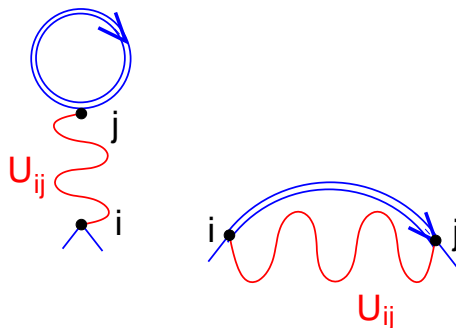


Figure 13. Left: Hartree diagram for the non-local Coulomb interaction. Right: Exchange diagram (Fock term). Both are taken into account within Hartree-Fock.

0. In our orbital basis $\varphi_{il}(\mathbf{r})$, the Hartree term contributes as

$$\Sigma_{iljm}^{\text{Hartree}} \equiv t_{iljm}^{\text{Hartree}} = \int d^3r \varphi_{il}^*(\mathbf{r}) \int d^3r' \rho(\mathbf{r}') V_{\text{ee}}(\mathbf{r}-\mathbf{r}') \varphi_{jm}(\mathbf{r}), \quad (71)$$

which is the left diagram of Fig. 13 and gives, Fourier-transformed, a \mathbf{k} -dependent self energy $\Sigma_{\mathbf{k}}^{\text{Hartree}}$. An advantage is that Hartree+DMFT is a diagrammatic approach, consisting of the Hartree diagram of Fig. 13 and the local DMFT contributions of all irreducible diagrams.

Because we know the Hartree contribution diagrammatically,¹ we are in full control of the double counting term of the many-body Hamiltonian Eq. [34]. Diagram Fig. 13 yields in terms of the on-site equal-time Green function $G_{ilm}^{\sigma}(\tau=0^+)$ the following local correction for the self energy of the interacting orbitals $l \in L_U$:

$$\Sigma_{\text{dc}}^{\text{Hartree}} = \frac{1}{\sum_{\sigma l}} \left[\sum_{\sigma l} U G_{ll}^{\sigma}(\tau=0^+) + \sum_{\substack{m \in L_U \\ m \neq l}} V G_{imim}^{\bar{\sigma}}(\tau=0^+) + (V-J) G_{imim}^{\sigma}(\tau=0^+) \right]. \quad (72)$$

Altogether, the Hartree+DMFT self energy consists of the ω -independent, but \mathbf{k} -dependent, Hartree contribution and the ω -dependent, but \mathbf{k} -independent, DMFT contribution with the double counting term subtracted:

$$\Sigma_{ijlm}^{\text{Hartree+DMFT}}(\omega) = \Sigma_{iljm}^{\text{Hartree}} + \delta_{ij} \Sigma_{lm}^{\text{DMFT}}(\omega) - \delta_{ij} \delta_{lm} \Sigma_{\text{dc}}^{\text{Hartree}}. \quad (73)$$

With this self energy, one needs to calculate a new electron density $\rho(\mathbf{r})$ which in turn gives a new $\Sigma_{ijlm}^{\text{Hartree+DMFT}}$ and has to be iterated until convergence.

¹It also follows from the variational principle as was stressed by Slater (180).

The advantages of Hartree+DMFT are that it follows the $d \rightarrow \infty$ concept and that it is a very clear and diagrammatically controlled scheme. The disadvantage, however, is that by neglecting the LDA exchange and correlation term all exchange and correlation contributions need to stem from DMFT which only includes the local exchange and correlations. With the success of LDA and its superiority over a simple Hartree calculation, this seems not to be sufficient. This explains the reluctance, in particular, of the physicists of the LDA community, to implement such a scheme. Indeed, Hartree+DMFT calculations have not been done in the context of realistic calculations; for model Hamiltonians see e.g. Ref. (101). A more thorough investigation of how well such a relatively simple scheme works for realistic calculations is mandatory. Also note that with cluster DMFT calculations, which were briefly discussed in Section 3.2, more and more non-local exchange and correlation contributions can be taken into account so that the treatment of the remaining Coulomb interaction terms by the Hartree approximation is a less severe approximation. The calculation of the screened Coulomb interaction parameters, however, remains challenging.

If one combined the Hartree-Fock (181) approximation and DMFT, at least the non-local exchange (given by the right diagram of Fig. 13) would be additionally included. The problem with the exchange term is that the Kohn-Sham equations become much more complicated due to the non-local nature of the exchange term: In terms of the first quantised wave functions $\varphi_i(\mathbf{r})$, the Hartree-Fock equations read

$$\left[-\frac{\hbar^2}{2m_e}\Delta + V_{\text{ion}}(\mathbf{r}) + \int d^3r' \frac{e^2}{4\pi\epsilon_0} \frac{1}{|\mathbf{r} - \mathbf{r}'|} \rho(\mathbf{r}') \right] \varphi_i(\mathbf{r}) - \sum_j \int d^3r' \frac{e^2}{4\pi\epsilon_0} \frac{\varphi_j^*(\mathbf{r}')\varphi_i(\mathbf{r}')}{|\mathbf{r} - \mathbf{r}'|} \varphi_j(\mathbf{r}) = \varepsilon_i \varphi_i(\mathbf{r}), \quad (74)$$

instead of the Kohn-Sham equation [6]. But because it is not local in \mathbf{r} , Eq. [74] is mathematically much more complicated to solve. Nonetheless, with increasing computational resources exact exchange calculations have become possible and were performed by Stadelde *et al.* (182).

Closely related are also the Hartree-Fock calculations by Schnell *et al.* (52; 53). The authors start with a conventional bandstructure calculation which is, however, only used to construct maximally localised Wannier orbitals by the Marzari-Vanderbilt (49) projection approach. With these orbitals Schnell *et al.* (52; 53) calculate the non-interacting hopping matrix elements, i.e. the overlap integral of these Wannier wave functions w.r.t. $-\frac{\hbar^2}{2m_e}\Delta + V_{\text{ion}}(\mathbf{r})$, and the Coulomb interaction by the overlap integral Eq. [33]. This defines a multi-band many-body Hamiltonian for which, because of

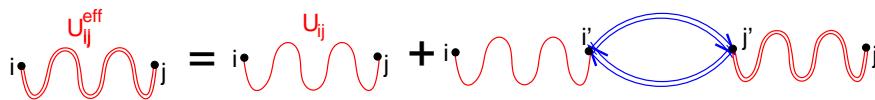


Figure 14. The bare Coulomb interaction (wiggled line) is, within RPA, screened by particle-hole excitations (Green function bubbles; double lines), resulting in a screened Coulomb interaction (wiggled double line) given by an infinite series of bubble diagrams which can be calculated self-consistently as indicated.

the localised orbitals, the hopping and Coulomb interaction between far apart orbitals is neglected. Schnell *et al.* (52; 53) solve this Hamiltonian within a reduced set of Wannier orbitals by Hartree-Fock. But their approach also offers the advantage that more sophisticated many-body approaches like DMFT can be employed in the future. The calculation of the screened Coulomb interaction remains problematic. Schnell *et al.* (52; 53) propose to employ the Thomas-Fermi theory of screening to this end.

4.3 GW+DMFT

A serious disadvantage of both, Hartree+DMFT and Hartree-Fock+DMFT, is that the screening of the Coulomb interaction is not yet included. Most important for this screening are the random phase approximation (RPA) bubble diagrams depicted in Fig. 14. Particle-hole excitations, even at relatively high energy, dramatically reduce the effective Coulomb interaction. This is taken into account by the infinite series of RPA diagrams, replacing the bare Coulomb interaction (wiggled line) by the screened Coulomb interaction (wiggled double line).

For a many-body physicist, a diagrammatically controlled approach for the challenging task of realistic material calculations is desirable. The minimal set of diagrams to this end are (i) the Hartree and Fock terms of Fig. 13 which make up a major contribution of the Coulomb interaction, (ii) the RPA diagrams of Fig. 14 for calculating the screened Coulomb interaction, and (iii) the local DMFT contribution of all irreducible diagrams for *d* or *f* materials with strong electronic correlations. The former two terms are contained in the so-called GW approach, and Biermann *et al.* (42) recently proposed to include the local dynamics of DMFT in a GW+DMFT method, also presenting first results for ferromagnetic Ni.

Let us start by briefly recapitulating the GW equations introduced by Hedin (41), for a review see Ref. (57). The GW self energy consists of the Hartree part, Eq. [71], and the exchange contribution, the right diagram of Fig. 13.

The latter is given by

$$\Sigma^{\text{GW}}(\mathbf{r}, \mathbf{r}'; \omega) = i \int \frac{d\omega'}{2\pi} G(\mathbf{r}, \mathbf{r}'; \omega + \omega') W(\mathbf{r}, \mathbf{r}'; \omega'). \quad (75)$$

This form of the self energy, Green function G times screened interaction W , coined the name of the ‘GW’ approximation. The imaginary unit i in front of G stems from the standard definition of the real time or real frequency Green function and the rules for evaluating the diagram Fig. 13, see Ref. (94).

To take the RPA screening into account, Eq. [75] employs the screened interaction W , i.e. the double line in Fig. 14. This screened W is given by a geometric series, defined iteratively in Fig. 14, which yields

$$W(\mathbf{r}, \mathbf{r}'; \omega) = \int d^3r'' V_{\text{ee}}(\mathbf{r}, \mathbf{r}'') \epsilon^{-1}(\mathbf{r}'', \mathbf{r}'; \omega). \quad (76)$$

Here, $V_{\text{ee}}(\mathbf{r}, \mathbf{r}'')$ is the bare Coulomb interaction (Eq. [2] in Section 2] which does not depend on ω , and $\epsilon^{-1}(\mathbf{r}, \mathbf{r}'; \omega)$ denotes the inverse of the dielectric function

$$\epsilon(\mathbf{r}, \mathbf{r}'; \omega) = \delta_{\mathbf{r}\mathbf{r}'} - V_{\text{ee}}(\mathbf{r}, \mathbf{r}') P^{\text{GW}}(\mathbf{r}, \mathbf{r}'; \omega). \quad (77)$$

Together, Eqs. [76] and [77] have the usual pole-structure of the geometric series in which the GW polarisation

$$P^{\text{GW}}(\mathbf{r}, \mathbf{r}'; \omega) = -2i \int \frac{d\omega'}{2\pi} G(\mathbf{r}, \mathbf{r}'; \omega + \omega') G(\mathbf{r}, \mathbf{r}'; \omega') \quad (78)$$

is the factor for the bubble consisting of two Green functions. In Eq. [78], the prefactor 2 stems from the spin summation, assuming here that G and Σ are spin-independent in a paramagnetic phase. Because of the screening the effective interaction W becomes frequency dependent.

Since the computational burden of the more complicated GW approximation is much higher than that of the simpler LDA, plane-wave basis calculations become very costly because of the big basis set. Therefore, the LMTO basis of Andersen (45) or a Gaussian basis is preferable.

To merge GW with DMFT, first the local contribution in the GW equations has to be subtracted since this part will later be included within DMFT:

$$\mathbf{P}^{\text{GW+DMFT}}(\mathbf{k}, \omega) = \mathbf{P}^{\text{GW}}(\mathbf{k}, \omega) - \underbrace{\frac{1}{V_{\text{BZ}}} \int_{\text{BZ}} d^3k \mathbf{P}^{\text{GW}}(\mathbf{k}, \omega)}_{\text{local contribution}} + \mathbf{P}^{\text{DMFT}}(\omega), \quad (79)$$

where we Fourier-transformed $P^{\text{GW}}(\mathbf{r}, \mathbf{r}'; \omega)$ of Eq. [78] from real to \mathbf{k} -space, and also employed an orbital basis, indicated by the bold symbols. To switch between the representation in terms of spatial coordinates \mathbf{r} and the representation in terms of orbitals l , one has to calculate the overlap integral w.r.t. the orbital wave functions $\varphi_{il}(\mathbf{r})$ or to multiply by $\varphi_{il}(\mathbf{r})$, respectively. In practice, Aryasetiawan *et al.* (44) propose to calculate the two-particle polarisations and interactions within another basis, the optimal product basis, see Ref. (57).

Similarly, we have

$$\begin{aligned} \Sigma^{\text{GW+DMFT}}(\mathbf{k}, \omega) &= \Sigma^{\text{GW}}(\mathbf{k}, \omega) - \frac{1}{V_{\text{BZ}}} \int_{\text{BZ}} d^3k \Sigma^{\text{GW}}(\mathbf{k}, \omega) \\ &+ \Sigma^{\text{Hartree}}(\mathbf{k}, \omega) - \Sigma_{\text{dc}}^{\text{Hartree}} + \Sigma^{\text{DMFT}}(\mathbf{k}, \omega). \end{aligned} \quad (80)$$

Here, also the Hartree self energy and its local part, Eqs. [71] and [72], respectively, have been included. The local DMFT self energy contribution is that of the auxiliary Anderson model or, equivalently, that of the local contribution of all irreducible diagrams. Note, that the combined contribution $\Sigma^{\text{DMFT}}(\mathbf{k}, \omega) - \Sigma_{\text{dc}}^{\text{Hartree}}$ is actually the exchange-correlation part of the DMFT self energy.

To calculate the DMFT polarisation, let us start with the local impurity interaction of the DMFT Hamiltonian Eq. [15], considering only density-density type of interaction between two orbitals, i.e. $U_{lmno} = \delta_{mn}\delta_{lo}U_{lm}$ in Eq. [15]. Within DMFT, this local interaction is screened, yielding a local screened interaction

$$W_{lm}(\omega) = U_{lm}(\omega) - \sum_{m'l'} U_{ll'}(\omega) \chi_{ll'm'm}(\omega) U_{m'm}(\omega), \quad (81)$$

which can be calculated from the local susceptibility

$$\chi_{lmno}(\tau) = \langle T c_l^\dagger(\tau) c_m(\tau) c_n^\dagger(0) n_o(0) \rangle. \quad (82)$$

Here, T is the time-ordering operator.

From the difference between the inverse matrices in the orbital index \mathbf{W} and \mathbf{U} , the DMFT local polarisation can be calculated by an inversion w.r.t. the orbital indices:

$$\mathbf{P}^{\text{DMFT}}(\omega) = \mathbf{U}^{-1}(\omega) - \mathbf{W}^{-1}(\omega). \quad (83)$$

This relation follows directly from the definition of the local polarisation analogous to Eq. [76], after substituting $\epsilon(\omega)$ of Eq. [77] and solving for $\mathbf{P}(\omega)$, with

$\mathbf{U}(\omega)$ playing the role of V_{ee} .

Now, however, the interaction $\mathbf{U}(\omega)$ is frequency dependent or (in imaginary time) τ -dependent. This has to be taken into account in the effective action of the Anderson impurity model, where we have now to employ the following $\mathcal{A}[\psi, \psi^*, (\mathcal{G}^0)^{-1}, \mathbf{U}]$ in Eq. [27]:

$$\begin{aligned} \mathcal{A}[\psi, \psi^*, (\mathcal{G}^0)^{-1}, \mathbf{U}] = & \sum_{\nu\sigma lm} \psi_{\nu m}^{\sigma*} (\mathcal{G}_{\nu mn}^{\sigma 0})^{-1} \psi_{\nu n}^{\sigma} \\ & + \sum_{lm\sigma\sigma'} \int_0^{\beta} d\tau \psi_l^{\sigma*}(\tau) \psi_l^{\sigma}(\tau) U_{lm}(\tau - \tau') \psi_m^{\sigma'*}(\tau') \psi_m^{\sigma'}(\tau'). \end{aligned} \quad (84)$$

Altogether, we are now in the position of formulating the GW+DMFT scheme, introduced by Biermann *et al.* (42; 43; 44), see flow diagram Fig. 15: Starting point is a conventional LDA calculation, yielding an electron density $\rho(\mathbf{r})$ and also a LDA Green function

$$\mathbf{G}_{\mathbf{k}}^{\text{LDA}}(\omega) = [\omega \mathbf{1} + \mu \mathbf{1} - \boldsymbol{\epsilon}^{\text{LDA}}(\mathbf{k})]^{-1}. \quad (85)$$

This Green function is inserted into Eq. [78] to calculate the GW polarisation $\mathbf{P}^{\text{GW}}(\mathbf{k}, \omega)$ and, via Eq. [77], the screened interaction $\mathbf{W}(\mathbf{k}, \omega)$, Eq. [76].

Now three self energies have to be calculated: (i) the GW self energy $\boldsymbol{\Sigma}^{\text{GW}}(\mathbf{k}, \omega)$, i.e. the Fourier transform of Eq. [75]; (ii) the Hartree self energy and double counting correction, Eqs. [71] and [72], respectively; and (iii) the DMFT self energy. For the latter, we first have to define the non-interacting Green function of the auxiliary DMFT impurity problem, i.e. \mathcal{G}^0 . Moreover, we have to unscreen the local Coulomb interaction since the DMFT diagrams include the local screening bubble, the contribution of Fig. 14 with $i' = j'$. This contribution would be doubly counted if we started DMFT with the fully screened \mathbf{W} .

The result of the calculation of the impurity problem will be the impurity Green function, which is identical to the local GW+DMFT Green function, and the local susceptibility. From these two quantities we can determine the local DMFT self energy and polarisation. Altogether, this then allows us to calculate the total GW+DMFT self energy and GW+DMFT polarisation. The former in turn allows us to calculate the GW+DMFT Green function by the Dyson equation [24] in which the non-interacting Green function is simply the solution of the *ab initio* Hamiltonian (Eq. [2]) without electron-electron interaction. With this new Green function \mathbf{G} , the DMFT self energy $\boldsymbol{\Sigma}^{\text{DMFT}}$, and the GW+DMFT polarisation $\mathbf{P}^{\text{GW+DMFT}}$, we can restart our iteration loop until convergence.

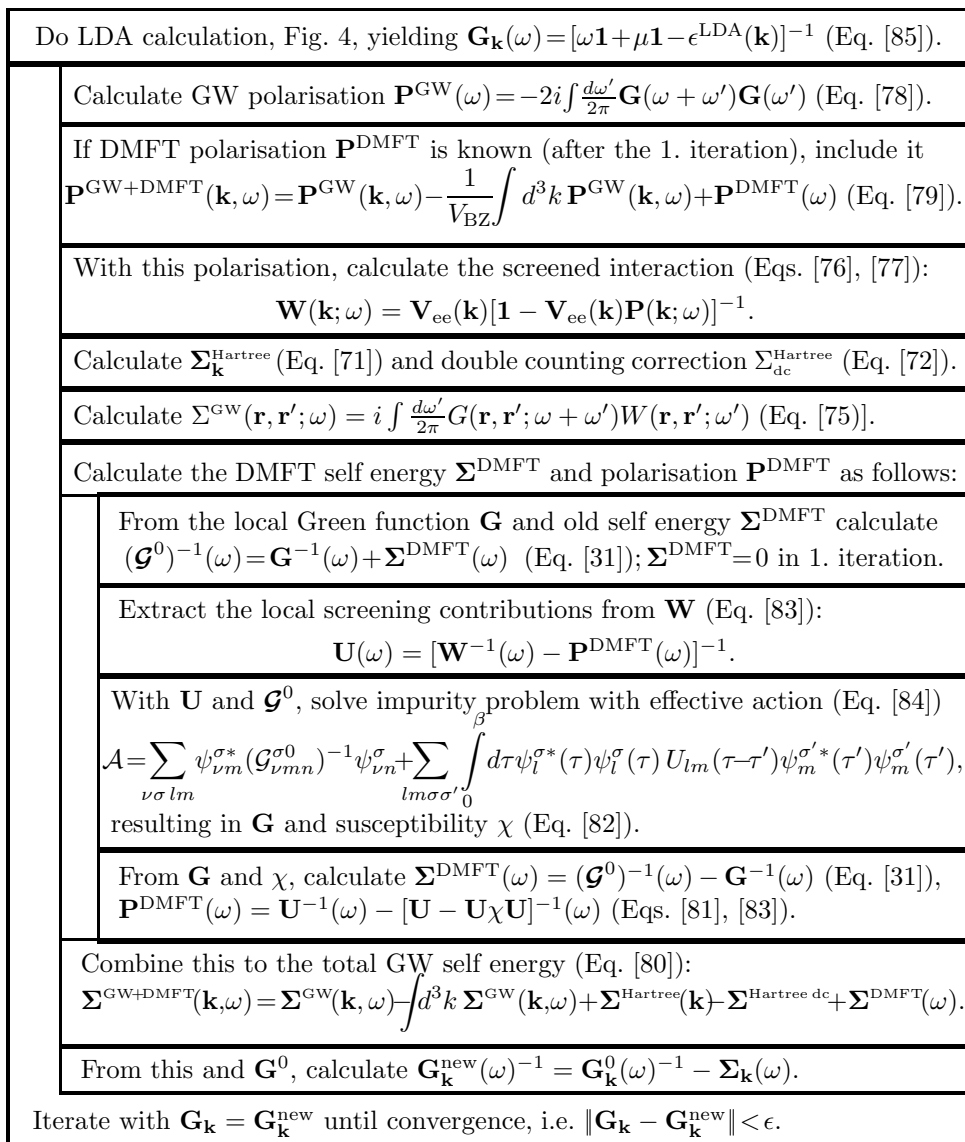


Figure 15. Flow diagram of the GW+DMFT algorithm.

Certainly, such a fully self-consistent GW+DMFT scheme is a formidable task, and Biermann *et al.* (42) employed a simplified implementation for their calculation of Ni: For the DMFT impurity problem, only the local Coulomb interaction between d orbitals was included and its frequency dependence was neglected $\mathbf{W}(\omega) = \mathbf{W}(0)$. Moreover, only one iteration step has been done, calculating the inter-site part of the self energy by GW with the LDA Green

function as an input and the intra-site part of the self energy by DMFT (with the usual DMFT self-consistency loop, see flow diagram Fig. 8). The GW polarisation \mathbf{P}^{GW} was calculated from the LDA instead of the GW Green function. This is, actually, common practice even for conventional GW calculations.

Notwithstanding, Aryasetiawan *et al.* (183) emphasised the importance of the frequency dependence of the Coulomb interaction, even for the effective low-energy physics. For a model Hamiltonian, the Hubbard model with nearest-neighbour interaction, Sun and Kotliar (184; 185) already performed such self-consistent GW+DMFT calculation and included further local correlations through the extended (E-)DMFT (176; 175; 186; 178). Also note, that one can embed GW+DMFT (similar to LDA+DMFT) as a Luttinger-Ward (166) free energy functional which is, here, a functional of the Green function \mathbf{G} and the screened Coulomb interaction \mathbf{W} ; for more details see Ref. (43).

5 DMFT solvers suitable for material calculations

The equivalence of the DMFT single-site problem and the Anderson impurity problem, noted by Georges and Kotliar (29), also see Jarrell (30), allows us to employ a variety of well established techniques to solve the DMFT equations. Since the DMFT results depend on this solver, we should be careful to employ the respective solvers only in the parameter regime where they are applicable, and e.g. not a perturbative approximation in the non-perturbative regime. Otherwise, we run the risk of reporting a good agreement with experiment which stems from a cancellation of errors. LDA+DMFT is an approximation and misses non-local correlations which are certainly important for some materials. If we introduce a second error due to the DMFT impurity solver, good agreement with experiment might be by chance. Possibly, we then overlook important non-local correlations.

For these reasons, Nekrasov *et al.* (159) coined the notation DMFT(X) and LDA+DMFT(X) where X denotes the solver for the auxiliary DMFT impurity problem.

In the following we will review the most common techniques X which are promising for material calculations with DMFT. At the beginning, we will discuss approximate techniques, starting with the Hartree approximation in Section 5.1 which makes the LDA+DMFT approach equivalent to LDA+U. This allows us to describe an insulating phase with Hubbard bands, albeit only if there is spin or orbital order. In the case of alternating antiferromagnetic or orbital order, however, LDA+U fails to yield the correct shape of the Hubbard bands since it misses the formation of polaron side bands (25). Alternatives, in particular for the paramagnetic phase without symmetry breaking,

are the approximations by Hubbard (15; 187) and extensions which are discussed in Section 5.2. In the opposite limit of weak coupling (weak Coulomb interaction), one can do iterated perturbation theory (IPT) which is second order perturbation theory in the local Coulomb interaction of the Anderson impurity model. IPT will be discussed in Section 5.3.

A good description of the behaviour at strong coupling is possible by $1/N$ type of approaches such as the non-crossing approximation (NCA), which is a resolvent perturbation in the hybridisation of the Anderson impurity model. These approaches become exact for a large number of degenerate orbitals N and are good for the insulator but also for the metal if the temperature is higher than the Kondo temperature of the impurity model. In Section 5.4, we will introduce the NCA.

In Section 5.5, the concept of numerically exact quantum Monte Carlo (QMC) simulations is introduced, which directly solve the Anderson impurity model, albeit on the imaginary axis. Therefore, the maximum entropy method (188) is needed for an analytical continuation to real frequencies if, for example, the spectral function is calculated. The numerical effort of QMC grows cubically with decreasing temperature so that it is possible to do room temperature, or say 100 K, calculations nowadays. Since the effort only grows cubically (not exponentially) with temperature calculations at lower temperatures will be possible in the future, although not at really low temperatures. To this end, Feldbacher *et al.* (189) recently developed a projective QMC algorithm for ‘ $T=0$ ’ calculations which we will also discuss.

We will not present details of the exact diagonalisation (ED) and the numerical renormalisation group (NRG) method of Wilson (190), which have been very successfully employed for the one-band Hubbard model: ED by Caffarel and Krauth (89), also see Ref. (56; 191), and NRG by Bulla *et al.* (192; 193; 194). Hence, let us briefly state the idea and the limitations for multi-orbital calculations here. Both of these methods diagonalise the Anderson impurity model. In the case of ED the Anderson impurity model is diagonalised directly for a limited number of non-interaction ‘bath’ sites. Astonishingly, Potthoff (195) demonstrated that even a single ‘bath’ site gives a very good estimate of the critical U value of the Mott transition. In the case of NRG, one diagonalises within a restricted energy window which is renormalised to lower and lower energies. Since the number of quantum mechanical states grows exponentially with the number of orbitals in the Anderson impurity model, these methods are severely restricted concerning the number of orbitals: one orbital is manageable; a sound calculation with two orbitals is already almost exceeding the computational limits, but can with great numerical effort still be done; a reliable treatment of three orbitals will be impossible even if computer resources grow considerably. Hence the usefulness of ED and NRG for realistic material calculations is very limited and we will not dis-

cuss these methods here, referring the reader to the references above for more information.

Most recently, also the related (dynamical) dynamical matrix renormalisation group (DMRG) approach (196; 197; 198) has been employed by different groups (199; 200; 201; 202; 203; 204). DMRG is a powerful alternative to ED and NRG and might become a standard impurity solver for DMFT in the future. For realistic multi-orbital calculations, it however also scales exponentially with the number of orbitals involved.

Another method which one might subsume under the $d \rightarrow \infty$ limit is the Gutzwiller approximation. As was shown by Metzner and Vollhardt (27; 205; 206) and Gebhard (207), this approximate treatment of the Gutzwiller (208; 209; 210) wave function becomes exact for $d \rightarrow \infty$. Gebhard (207; 211) also showed that the $d \rightarrow \infty$ Gutzwiller wave function is equivalent to the Kotliar-Ruckenstein (212) slave Boson approximation at zero temperature (also note recent slave-rotor (213) and slave-spin (214) variants). The Gutzwiller wave function starts with the Fermi sea onto which the so-called Gutzwiller correlator $g^{\hat{d}}$ is applied, where \hat{d} is the operator of local double occupations, i.e. $\hat{d} = \sum_i \hat{n}_{i\uparrow} \hat{n}_{i\downarrow}$ for the one-band Hubbard model. With g as a variational parameter, this wave function emulates a central effect of the local Coulomb interaction, the reduction of the number of doubly occupied sites. An important step for our understanding of the Mott-Hubbard transition was the work by Brinkman and Rice (20) who recognised that the Gutzwiller approximation describes a Mott-Hubbard metal-insulator transition, indicated by the disappearance of the quasiparticle peak. This approximation, stemming from the metallic side, however misses a correct description of the Hubbard bands. Gebhard (211) generalised the Gutzwiller approximation to the multi-orbital situation, allowing subsequently Strack and Vollhardt (215; 216) and Gulásci *et al.* (217) to apply it to model Hamiltonians. More recently, it was employed for realistic calculations of ferromagnetic transition metals by Bünemann *et al.* (218; 219; 220), for a summary of these results see Ref. (221). Closely related to this are also material calculations with the local ansatz, which has been employed for material calculations long before DMFT, see, e.g. Refs. (222; 223; 224).

5.1 Polarised Hartree-Fock (HF) approximation (LDA+U)

The simplest way to deal with the auxiliary Anderson impurity problem of DMFT, Eq. [26], is to treat the interaction in the Hartree-Fock (HF) approximation. The Hartree diagram has already been shown in Fig. 13 (left) and corresponds to the decoupling

$$\langle \hat{c}_l^\sigma \dagger \hat{c}_l^\sigma \hat{c}_m^{\sigma'} \dagger \hat{c}_m^{\sigma'} \rangle \xrightarrow{\text{Hartree}} \hat{c}_l^\sigma \dagger \hat{c}_l^\sigma \langle \hat{c}_m^{\sigma'} \dagger \hat{c}_m^{\sigma'} \rangle + \langle \hat{c}_l^\sigma \dagger \hat{c}_l^\sigma \rangle \hat{c}_m^{\sigma'} \dagger \hat{c}_m^{\sigma'} - \langle \hat{c}_l^\sigma \dagger \hat{c}_l^\sigma \rangle \langle \hat{c}_m^{\sigma'} \dagger \hat{c}_m^{\sigma'} \rangle. \quad (86)$$

Hence, correlations given by

$$\langle \hat{c}_l^{\sigma\dagger} \hat{c}_l^{\sigma} \hat{c}_m^{\sigma'\dagger} \hat{c}_m^{\sigma'} \rangle - \langle \hat{c}_l^{\sigma\dagger} \hat{c}_l^{\sigma} \rangle \langle \hat{c}_m^{\sigma'\dagger} \hat{c}_m^{\sigma'} \rangle \quad (87)$$

are neglected within the Hartree approximation, i.e. within the approximate expectation value of the right hand side of Eq. [86]. In principle, we can treat the Fock term on a similar footing with a decoupling into non-diagonal expectation values of the form $\langle \hat{c}_l^{\sigma\dagger} \hat{c}_m^{\sigma'} \rangle$. However, for the local Fock term to contribute we need either a (non-diagonal) magnetisation in the xy plane or a corresponding kind of orbital ordering. At least for degenerate orbitals, these Fock expectation values, or the off-diagonal Green function required in the diagram Fig. 13 (right), are zero. Therefore, the local Fock term is usually not considered, only the Hartree term.

If the Coulomb interaction has the form of Eq. [34] with an intra-orbital Coulomb interaction U , an inter-orbital interaction V and Hund's exchange coupling J , Eq. [86] or equivalently the Green function of Fig. 13 (left) result in the Hartree self energy

$$\Sigma_l^{\text{Hartree}} = U \langle \hat{n}_l^{\bar{\sigma}} \rangle + \sum_{m \in L_U | \neq l} V \langle \hat{n}_m^{\bar{\sigma}} \rangle + (V - J) \langle \hat{n}_m^{\sigma} \rangle. \quad (88)$$

This is (up to a constant) the same as Eq. [72] if orbitally averaged and expressed in terms of Green functions instead of expectation values (Eq. [39]).

Doing such a LDA+DMFT(HF) calculation is completely equivalent to the LDA+U approach (19), also see Ref. (225). For a simple Hartree calculation, the DMFT formulation is not necessary and instead of decoupling the interaction of the Anderson impurity model one can directly apply the Hartree decoupling to the LDA-constructed many-body multi-orbital problem Eq. [34]. This is how Anisimov *et al.* (19) arrived at the LDA+U scheme.

Because of the purely local interaction, the Hartree self energy, Eq. [88], is \mathbf{k} -independent. Moreover, it is static, i.e. ω -independent. What kind of physics can we then expect to be described? For the paramagnetic phase with an equal orbital occupation, $\Sigma_l^{\text{Hartree}}$ is independent of l . Hence, the self energy is reduced to a constant shift like a chemical potential, which moreover should be canceled by the orbitally-averaged double-counting correction given by Eq. [72]. There is no effect at all.

This changes if the spin or orbital degrees of freedom are ordered (*polarised*), either in a homogenous way like the Stoner (226) ferromagnet or in a more complicated pattern such as the checkerboard alternating Néel (227) state, which gives rise to the Slater (96) bands. In these polarised phases, the bands of different spin or orbital species split into subbands since the self energy Eq. [88] differs. For a large average Coulomb interaction $\bar{U} = [U + (M - 1)V +$

$(M-1)(V-J)/(2M-1)$ (M : number of orbitals) this splitting results in two completely separated sets of bands with a typical distance \bar{U} at large \bar{U} . For an integer filling, the lower set of bands will be completely filled and the upper set completely empty, resembling the Hubbard bands of a Mott insulator, shown schematically in Fig. 2 of Section 1.

Since the number of double occupations is minimal for this large \bar{U} phase, the symmetry-broken Hartree-Fock solution also correctly produces the total energy in the $\bar{U} \rightarrow \infty$ limit. The corrections to this limit are of order W^2/\bar{U}^2 and depend on the kind of ordering, leading to the LDA+U prediction for the symmetry breaking in a specific material. Together with the insulating spectrum, this explains why the LDA+U method has been successfully applied for the *ab initio* calculation of insulators, including their low temperature ordering.

This good description of the insulator might be astonishing if one considers that the starting point, the Hartree self energy Eq. [88], is first-order perturbation theory in the Coulomb interaction, which suggests that Hartree is good at weak coupling (Coulomb interaction) only. However, except for almost uncorrelated systems with $\bar{U}/W \ll 1$, the Hartree approximation is rather bad for the metallic phase. The reason is that it strongly overestimates the energy of the paramagnetic phase. This paramagnetic energy grows $\sim \bar{U}$ since double occupations cannot be avoided without symmetry breaking in the Hartree approximation. Therefore, the tendency towards orbital or magnetic ordering is heavily overestimated, and LDA+U almost automatically yields split-bands even if this is not correct at small and intermediate strengths of the Coulomb interaction where the system is paramagnetic or has a much smaller magnetisation than the Hartree approximation predicts.

Nonetheless, a paramagnetic insulator with Hubbard bands with separation \bar{U} can be described by LDA+U if one considers the symmetry breaking as an artificial means to produce the correct spectrum and energy. Of course, then the magnetisation is incorrect, but also the free energy since the entropy of paramagnetic uncoupled spins is much higher than that of ordered spins. These obstacles can be overcome by the Hubbard-I approximation which also has the advantage that the weights of the Hubbard bands are better reproduced for non-integer fillings, see the following Section.

A cautious remark is also in place if one applies LDA+U for studying antiferromagnetic or orbitally ordered phases: While LDA+U then yields the correct *static* properties, dynamic properties are completely wrong. This was shown by Sangiovanni *et al.* (25), who particularly pointed out that the DMFT Hubbard bands are very different from the coherent, narrowed Hubbard bands of LDA+U: The DMFT Hubbard bands are incoherent, have spin-polaron side peaks and their widths correctly converges to that of the non-interacting bands for $\bar{U} \rightarrow \infty$ (25).

5.2 Hubbard-I, Hubbard-III and alloy-analogy approximation

Starting point of the Hubbard (15; 187) approximations is the atomic limit ($W = 0$), in which we can calculate the (purely local) Green function exactly, including the full multiplet structure with the spin-flip and pair-hopping term of the LDA+DMFT Hamiltonian (Eq. [34]). Due to the itinerancy of the system these atomic levels are, however, broadened. This broadening is included in different ways in the Hubbard-I (15) and Hubbard-III approximation (187), as well as in the alloy-analogy approximation.

The Hubbard approximations can be derived by decoupling the higher order Green functions in the equations of motion. This procedure is not controlled and allows for many different decoupling schemes, i.e. approximations. For infinite dimensions, the simplified momentum summations allow for the decoupling of higher order Green functions (228).

For realistic material calculations, Lichtenstein and Katsnelson (32) formulated the LDA+Hubbard-I, or in our notation LDA+DMFT(Hubbard-I), approach as one of their LDA++ approaches. For the γ -phase of cerium such LDA+DMFT(Hubbard-I) calculations by McMahan *et al.* (229) were quite successful. These cerium results will be presented in Section 6.1.1.

Here we will motivate the Hubbard-I approximation physically without attentiveness to the original equation of motion derivation by Hubbard (15; 187; 14) In the atomic limit, the hybridisation of our DMFT Anderson impurity model (Eq. [26]) vanishes and the impurity problem is simply the isolated atom for which the Green function is known exactly. Expressed via the spectral representation, see Ref. (94) p. 163 ff., it reads

$$G_{lm}(\omega) = \sum_{\mu\nu} \frac{\langle \mu | c_l | \nu \rangle \langle \nu | c_m^\dagger | \mu \rangle}{\omega + \mu - E_\nu + E_\mu} e^{-\beta[E_\nu - \mu(N+1)]} (1 - e^{-\beta(E_\mu - E_\nu + \mu)}). \quad (89)$$

Here, $|\mu\rangle$ ($|\nu\rangle$) are the exact many-body eigenvectors with eigenenergies E_μ (E_ν) for N ($N+1$) electrons. For the atomic limit we know these eigenenergies and vectors so that, without Hund's exchange ($J = 0$, $\bar{U} = U = V$) and for degenerate levels with site energy ε , the atomic Green function reads

$$G^{\text{at}}(\omega) = \sum_{N=0}^{2M-1} \frac{w_N(\mu_{\text{at}}, T)}{\omega + \mu_{\text{at}} - NU - \varepsilon}. \quad (90)$$

Thereby, the weights of the poles are given by

$$w_N = \frac{(N+1)v_{N+1} + (2M-N)v_N}{2M \sum_{N'=0}^{2M} v_{N'}}. \quad (91)$$

These are determined in turn by the weight for having N electrons on the atom with altogether $2M$ states

$$v_N = \frac{2M!}{N!(2M - N)!} e^{-\beta[\frac{1}{2}N(N-1)U + N\varepsilon - N\mu_{\text{at}}]}, \quad (92)$$

consisting of the Boltzmann weight and a combinatorial factor for the number of orbital configurations with N electrons in M degenerate orbitals. From G^{at} , we can also calculate the average number of local electrons n^{at} , for example, via the following sum over Matsubara frequencies ω_ν :

$$n^{\text{at}} = 2MT \sum_{\nu} G^{\text{at}}(i\omega_\nu) e^{i\omega_\nu 0^+} + 2M. \quad (93)$$

Since the non-interacting Green function of the Anderson impurity model is known to be $\mathcal{G}^0(\omega) = 1/(\omega + \mu - \varepsilon)$ the exact self energy in the atomic limit reads:

$$\Sigma^{\text{at}}(\omega) = \omega + \mu - \varepsilon - [G^{\text{at}}(\omega)]^{-1}. \quad (94)$$

Hubbard (15) now approximated the self energy of the itinerant problem by this atomic self energy:

$$\Sigma(\omega) = \Sigma^{\text{at}}(\omega). \quad (95)$$

This self energy allows us to calculate the \mathbf{k} -dependent Green function via the Dyson equation [24] or the local Green function via Eq. [32]:

$$\mathbf{G}(\omega) = \frac{1}{V_{\text{BZ}}} \int_{\text{BZ}} d^3k [\omega \mathbf{1} + \mu \mathbf{1} - \tilde{\epsilon}^{\text{LDA}}(\mathbf{k}) - \Sigma(\omega) \mathbf{1}]^{-1}. \quad (96)$$

Here, $\tilde{\epsilon}^{\text{LDA}}$ denotes the LDA bandstructure minus double counting correction as defined in Eq. [37]. For consistency, we require that the number of electrons in the auxiliary atomic problem n^{at} equals the average number n_d of electrons in the interacting d or f orbitals, which is calculated from the corresponding orbitals of the Green function $\mathbf{G}(\omega)$ of Eq. [96]. For this requirement to hold, we have to adjust μ_{at} correspondingly (230; 231; 232; 233). Noting that the w_j 's sum to one, we also see that $\Sigma^{\text{at}}(\omega) \xrightarrow{\omega \rightarrow \infty} (2M - 1)/(2M) U n_d$ which is the paramagnetic Hartree-Fock value and correct in the high-temperature limit.

Let us now elucidate the features of the Hubbard-I approximation. In contrast to the atomic limit, the Hubbard-I Green function has ‘dynamic’ Hub-

bard bands with a finite width. Usually $T \ll U$, so that only two addends contribute to the atomic Green function of Eq. [90]. Then, there will be two Hubbard bands which are centred around $-\mu$ and $U - \mu$ at large U . If the average number of electrons in the interacting orbitals n_d is integer, the lower Hubbard band at $-\mu$ will be completely filled and the upper Hubbard band at $U - \mu$ completely empty. Similar as in the Hartree-Fock approximation of Section 5.1, but now in the paramagnetic phase. In contrast to the rigid bands of the Hartree approximation, these spectral weights shift, however, when n_d is non-integer. This is very physical, since for non-integer n_d one can add an extra electron without paying more Coulomb interaction energy than for the last electron added.

The major deficit of the Hubbard approximations is that the metal which is generally described at non-integer n_d is not a Fermi liquid. This is a consequence of the construction with the *atomic* self energy. Hence, the Hubbard-I approximation is not an adequate method for non-integer n_d , except for such high temperatures at which the Fermi liquid behaviour has been lost. Or if, as in the case of manganites, strong scattering destroys the Fermi liquid behavior, justifying the application of the Hubbard-I approximation for this system (234; 235; 236; 237) to some extend.

There have been several attempts to improve the Hubbard-I approximation, starting with Hubbard's own work. The alloy-analogy approximation and the Hubbard-III approximation (187) introduce an additional energy-dependent scattering correction $\Delta(\omega)$ to the self energy which then becomes

$$\Sigma(\omega) = \Sigma^{\text{at}}(\omega - \Delta(\omega)). \quad (97)$$

In the alloy-analogy approximation, $\Delta(\omega)$ is fixed by requiring that the local Green function calculated from $\Sigma(\omega)$ via Eq. [96] still fulfils the atomic-limit Eq. [94]

$$G^{\text{at}}(\omega) = [\omega + \mu_{\text{at}} - \varepsilon - \Delta(\omega) - \Sigma(\omega)]^{-1}, \quad (98)$$

but with the scattering correction $\Delta(\omega)$. After substituting Σ^{at} from Eq. [94] into Eq. [98], we obtain an implicit equation for $\Delta(\omega)$.

The physical picture behind the alloy-analogy is that the electrons of one orbital move in a background of static electrons of the other orbitals. This reduces the Hubbard model to the simpler Falicov-Kimball model. With this approximation, the Coulomb interactions are reduced to a static scattering potential which is evaluated within the coherent potential approximation (CPA). Note that for disordered (non-interacting) systems the CPA (238; 239; 240; 241; 242; 243) becomes exact for the scattering problem in $d \rightarrow \infty$ (244); for a CPA-inspired derivation of DMFT, see (77; 245; 246).

Another way of thinking is in terms of moments of the interacting spectral function. Then, the Hubbard-I approximation yields the first two moments correctly and further-going approximations by Nolting and coworkers (247; 248; 249; 250; 251; 252) the first three moments.

The advantage of this alloy-analogy approximation and also the further going Hubbard-III approximation are that the splitting of the bands now occurs at a finite U . Moreover, the widths of the Hubbard-III bands at large U equals the width of the non-interacting system in agreement with general arguments. In contrast, this width is reduced in the Hubbard-I approximation and even goes to zero for a Slater (96) type of alternating ordering in the Hartree approximation. In contrast, the DMFT Hubbard bands have the correct width W also for staggered ordering (25).

The equation of motion decoupling scheme by Lacroix (253; 254) for the Anderson impurity model is also noteworthy here. It results in a three peak structure with a central resonance and two split-off side bands. Within the DMFT self-consistency scheme, it was employed by Jeschke and Kotliar (255).

Let us conclude here that Mott insulating materials can be described, at strong coupling, by the Hubbard-I and -III approaches, the alloy-analogy or CPA, and the LDA+ U method. Important differences concern the magnetic ordering tendencies and the shape of the Hubbard bands. The development of an *ab initio* approach which can be more generally used than LDA+ U or LDA+DMFT(Hubbard-I) for insulating transition metal oxides and other Mott insulators seems to be manageable.

5.3 Iterated perturbation theory (IPT) and extensions

The approaches discussed so far (Section 5.1 and 5.2) were only eligible deep within the Mott insulating phase. To describe the metallic phase, a natural starting point is weak coupling perturbation theory in the Coulomb interaction U . To first order in U , this is the Hartree-Fock approximation which is, however, better suited for a Mott insulator with magnetic or orbital ordering, as was shown in Section 5.1. To second order in U , we have to deal with the diagram shown in Fig. 16. As Green function we can either inset the bare non-interaction Green function of the Anderson impurity problem \mathcal{G}^0 or we can use the interacting Green function \mathbf{G} of the Anderson impurity model, generating an infinite series of \mathcal{G}^0 diagrams which is self-consistent in the sense of Baym and Kadanoff (167; 168). Müller-Hartmann (66) and Schweitzer and Czychołł Ref. (82) followed the latter path, which was extended by Menge and Müller-Hartmann (256) to bubble and ladder summations. However, while this self-consistent second order perturbation theory gives to order $(U/W)^2$ the same result as the perturbation theory in the bare \mathcal{G}^0 , it lacks important physical aspects, in particular the formation of Hubbard bands.

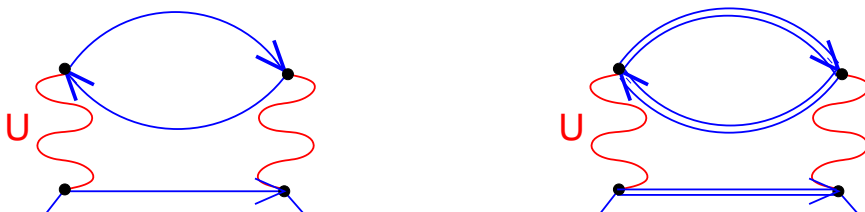


Figure 16. Second order perturbation theory for the Anderson impurity model with the bare Green function \mathcal{G}^0 (left) and the full Green function \mathbf{G} (right).

These and even the correct qualitative features of the Mott-Hubbard transition in the one-band Hubbard model are described by the iterated (second order) perturbation theory (IPT) of Georges and Kotliar (29), in which the bare \mathcal{G}^0 of the auxiliary DMFT impurity model is used. Yosida and Yamada (257; 258) and Zlatić (259) realised already that this bare perturbation theory for the Anderson impurity model is astonishingly good, showing a three peak structure with a qualitatively correct central quasiparticle resonance. This motivated Georges and Kotliar (29) to employ IPT as a DMFT solver. Later, Zhang *et al.* (260) recognised that IPT, albeit being a weak-coupling perturbation theory, also becomes correct in the strong coupling limit ($U \rightarrow \infty$). Hence, it might not be so astonishing that IPT describes the qualitative features of the Mott-Hubbard transition correctly, see Ref. (56).

Let us now write down the IPT equation. From the Feynman diagram Fig. 16, we obtain in terms of imaginary time τ and Matsubara frequencies ω_n :

$$\Sigma^{\text{IPT}}(i\omega_n) = \frac{2M-1}{2M} n_d U - U^2 \underbrace{\int_0^\beta d\tau e^{i\omega_n \tau} \mathcal{G}^0(\tau) \mathcal{G}^0(\tau) \mathcal{G}^0(-\tau)}_{\Sigma^{(2)}(i\omega_n)}. \quad (99)$$

Here, the first part is the Hartree term, which yields the high- ω behaviour. The second part stems from the second order diagram of Fig. 16.

Away from the, maybe coincidentally, good description for the half-filled one-band Hubbard model, IPT is less good at intermediate coupling and fails to reproduce the atomic limit. Because of these shortcomings but also because of the success of IPT for the half-filled one-band Hubbard model, several groups developed extrapolation schemes for the self energy which reproduce the correct self energy to second order in U/W and the atomic limit. Edwards and Hertz (261; 262) extended the Hubbard approximations from Section 5.2 to yield the correct result to order $(U/W)^2$. This approach gives a Fermi liquid phase at small U , however, there is an unphysical paramagnetic, non-Fermi-liquid metallic phase at intermediate U values before the system becomes

insulating.

Kajueter and Kotliar (263; 264) made an ansatz for the self energy of the form

$$\Sigma^{\text{IPT}'}(\omega) = \frac{2M-1}{2M}n_dU + \frac{A\Sigma^{(2)}(\omega)}{1-B\Sigma^{(2)}(\omega)} \quad (100)$$

where $\Sigma^{(2)}$ is the second order contribution from Eq. [99], analytically continued to the real axis. The parameters B and A are determined to give the correct self energy in the strong coupling limit ($U \rightarrow \infty$) and the correct $1/\omega$ behaviour, respectively. The latter also guarantees that the first two spectral moments are correct. However, the quasiparticle peak comes out too small in the IPT approximation by Kajueter and Kotliar. Potthoff *et al.* (265; 266) employed the same ansatz but adjusted the parameters to reproduce the correct third moment of the spectral function as well. In essence, this scheme is an interpolation scheme for the self energy between IPT and the strong coupling spectral density approach by Nolting and Borigiel (248). The ansatz by Potthoff *et al.* (265; 266) also allows for the treatment of magnetic phases.

Another self energy interpolation scheme was recently proposed by Oudovenko, Savrasov *et al.* (267; 268), using the Kotliar-Ruckenstein (212) slave Boson approach at weak and the Hubbard-I approximation at strong coupling. Also the local moment approach of Logan *et al.* (269; 270; 271) fulfils this feature of reproducing the correct weak and strong coupling limit.

Anisimov *et al.* (31) used IPT with the Kajueter-Kotliar IPT (264) interpolation as the impurity solver in the first LDA+DMFT calculations. As was demonstrated by Nekrasov *et al.* (159) in the context of realistic calculations for LaTiO_3 , IPT yields too small quasiparticle weights and violates the Fermi energy pinning, which was proven by Müller-Hartmann (66) for the one-band Hubbard model repeating the Luttinger-Ward (166) arguments and which generally holds for multi-band systems if the self energy for *all* orbitals is degenerate. This is, of course, generally not the case in realistic material calculations. It can be fulfilled if the DMFT calculation works with a restricted set of orbitals, e.g. degenerate t_{2g} orbitals for transition metal oxides.

An alternative weak-coupling perturbative approach is the fluctuation exchange approximation (FLEX) of Bickers and Scalapino (272) which has been employed as a DMFT solver in realistic calculations by Lichtenstein and Katnelson (32), Chioncel *et al.* (273) and Drchal *et al.* (274; 275). While this approach might be suitable for rather weakly correlated metals, i.e. at weak coupling U , it does not capture the development of Hubbard bands. Therefore, it is not appropriate at intermediate and strong coupling.

5.4 Non-crossing approximation (NCA)

The non-crossing approximation (NCA) is a conserving approximation corresponding to the resummation of a particular class of diagrams (those that do not cross). It can also be formulated as a resolvent perturbation theory in the hybridisation $\Delta(\omega)$ of the Anderson impurity problem (276; 277). Hence, it is reliable at strong coupling where, for all orbital matrix elements, $\Delta_{lm}^\sigma(\omega) \ll U$.

Let us start by rewriting the non-interacting Green function of the Anderson model (Eq. [27]) in a form consisting of a local and a hybridisation part (bold symbols indicate orbital matrices):

$$[\mathcal{G}^0(\omega)]^{-1} = \omega + \mu - \epsilon^{\text{at}} - \Delta(\omega), \quad (101)$$

where we identify the local part by

$$\epsilon^{\text{at}} = \frac{1}{V_{\text{BZ}}} \int d^3k \tilde{\epsilon}^{\text{LDA}}(\mathbf{k}). \quad (102)$$

Then, the Dyson equation [31] of the Anderson impurity model which connects the non-interacting Green function $\mathcal{G}^0(\omega)$ of the Anderson model and the local interacting Green function $\mathbf{G}(\omega)$ reads

$$[\mathbf{G}(\omega)]^{-1} = \omega + \mu - \epsilon^{\text{at}} - \Delta(\omega) - \Sigma(\omega). \quad (103)$$

Since NCA is a perturbation theory in terms of the hybridisation function $\Delta(\omega)$, the first step is to diagonalise the atomic problem (at) as in the Hubbard approximations of Section 5.2. In Section 5.2 we did so for the restriction to degenerate orbitals and a single Coulomb parameter U . Let us here diagonalise the atomic problem by formally rewriting the local Hamiltonian in terms of the local eigenvectors $|\alpha\rangle$ and eigenenergies E_α :

$$\hat{H}^{\text{at}} = \sum_{lm\sigma} \hat{c}_{l\sigma}^\dagger \epsilon_{lm}^{\text{at}} \hat{c}_{m\sigma} + \sum_{lmno\sigma\sigma'} U_{lmno} \hat{c}_l^{\sigma\dagger} \hat{c}_m^{\sigma'\dagger} \hat{c}_n^{\sigma'} \hat{c}_o^\sigma \quad (104)$$

$$= \sum_{\alpha} E_{\alpha} |\alpha\rangle \langle \alpha|. \quad (105)$$

In this eigenbasis, the creation and annihilation operators read

$$\hat{c}_{l\sigma}^\dagger = \sum_{\alpha,\beta} \left(D_{\beta\alpha}^{l\sigma} \right)^* |\alpha\rangle \langle \beta|, \quad (106)$$

$$\hat{c}_{l\sigma} = \sum_{\alpha,\beta} D_{\beta\alpha}^{l\sigma} |\beta\rangle \langle \alpha|. \quad (107)$$

Here, the eigenstates denoted by $|\alpha\rangle$ have one electron more than the $|\beta\rangle$ states.

A particular advantage of NCA is that this approach allows us to take into account the full Coulomb matrix plus the spin-orbit coupling. Of course, one will in practice reduce the matrix U_{lmno} to two-orbital terms as in Hamiltonian [9] of Section 4, but the spin-flip contribution of the Hund exchange coupling and the pair-hopping term can be included.

The key quantity for the resolvent perturbation theory is the resolvent $\hat{R}(\omega) = (\omega - \hat{H})^{-1}$. Without hybridisation, this resolvent can be simply expressed in the eigenbasis of \hat{H}^{at} :

$$\hat{R}^{\text{at}}(\omega) = \sum_{\alpha} \frac{1}{\omega - E_{\alpha}} |\alpha\rangle \langle \alpha|. \quad (108)$$

If we now take into account the hybridisation $\Delta(\omega)$, we can define a self energy correction due to this hybridisation. Denoting this self energy by $\hat{S}(\omega)$, the Dyson equation for the resolvent reads:

$$\hat{R}(\omega) = \hat{R}^{\text{at}}(\omega) + \hat{R}^{\text{at}}(\omega) \hat{S}(\omega) \hat{R}(\omega). \quad (109)$$

Following Keiter and Kimball (276) and Bickers *et al.* (277), we now express $\hat{S}(\omega)$ in a power series in terms of the hybridisation and cut this power series after the lowest order term (this is the non-crossing *approximation*):

$$\begin{aligned} S_{\alpha\beta}(\omega) = & \sum_{\sigma} \sum_{lm} \sum_{\alpha'\beta'} \int \frac{d\varepsilon}{\pi} f(\varepsilon) \left(D_{\alpha'\alpha}^{l\sigma} \right)^* \Gamma_{lm}^{\sigma}(\varepsilon) R_{\alpha'\beta'}(\omega + \varepsilon) D_{\beta'\beta}^{m\sigma} \\ & + \sum_{\sigma} \sum_{lm} \sum_{\alpha'\beta'} \int \frac{d\varepsilon}{\pi} (1 - f(\varepsilon)) D_{\alpha'\alpha}^{l\sigma} \Gamma_{lm}^{\sigma}(\varepsilon) R_{\alpha'\beta'}(\omega - \varepsilon) \left(D_{\beta'\beta}^{m\sigma} \right)^* \end{aligned} \quad (110)$$

Here, $S_{\alpha\beta}(\omega)$ and $R_{\alpha\beta}(\omega)$ are the matrix elements of $\hat{S}(\omega)$ and $\hat{R}(\omega)$, respectively, in the atomic eigenbasis; $f(\varepsilon) = 1/[1 + \exp(-\beta\varepsilon)]$ denotes the Fermi function, and $\Gamma_{lm}^{\sigma}(\varepsilon) = -\Im m \{ \Delta_{lm}^{\sigma}(\varepsilon + i0^+) \}$ is the imaginary part of the hybridisation. The resolvent $\hat{R}(\omega)$ in Eq. [110] has to be determined self-consistently in order to yield a conserving approximation for the Anderson impurity model. If we expressed Eq. [110] diagrammatically we would see that no conduction electron lines cross.

To employ NCA in the DMFT context, we have to determine the key quan-

tity of DMFT, i.e. the local Green function $\mathbf{G}(\omega)$. This is achieved via

$$G_{ilim}^{\sigma}(\omega) = \frac{1}{\mathcal{Z}^{\text{at}}} \sum_{\alpha, \alpha'} \sum_{\beta, \beta'} D_{\alpha\alpha'}^{l\sigma} (D_{\beta\beta'}^{m\sigma})^* \oint \frac{d\omega' e^{-\beta\omega'}}{2\pi i} R_{\alpha\beta}(\omega') R_{\alpha'\beta'}(\omega' + \omega), \quad (111)$$

with the atomic partition function

$$\mathcal{Z}^{\text{at}} = \sum_{\alpha} \oint \frac{d\omega e^{-\beta\omega}}{2\pi i} R_{\alpha\alpha}(\omega). \quad (112)$$

With $\mathbf{G}(\omega)$ from Eq. [111], we can continue the DMFT cycle, defining a new auxiliary Anderson impurity problem, solving it by NCA *etc.*

The particular advantages of NCA are that it is a (computationally) relatively fast method—at least if not too many orbitals are involved—, and a conserving approximation to the Anderson impurity model. It is good at strong coupling and at temperatures above the effective Kondo temperature of the Anderson impurity model. The drawbacks are that NCA is known to violate Fermi liquid properties at low temperatures (below the Kondo temperature) and whenever charge excitations become dominant (278; 85). Hence, in some parameter ranges it fails in the most dramatic way and must therefore be applied with considerable care (85). The NCA has been used intensively as a DMFT solver, in particular, by Pruschke and coworkers. In the context of LDA+DMFT, Zölfl *et al.* Ref. (279; 280) studied LaTiO₃ and cerium by NCA.

The same shortcomings are principally also true for the one-crossing approximation (281; 282) which goes beyond Eq. [110] by taking into account additional diagrams with a single line crossing, a vertex correction. Haule *et al.* (283) used this extension recently to study the optical conductivity of cerium. The conserving T matrix approximation (CTMA) includes further diagrams beyond NCA. Kirchner *et al.* (284) extended this approach to calculate dynamical properties which are necessary for a DMFT solver. This approach fulfils the Fermi liquid properties at low temperatures and might improve on most deficiencies of the NCA. Hence, this approximation might be suitable for DMFT, in particular, if the deficiency of not yielding the exact unitary limit, the exact height of the spectral function at $\omega = 0$, is overcome (284). Most recently, also a direct expansion of the Green function in terms of the hybridisation has been proposed (285).

5.5 Quantum Monte Carlo (QMC) simulations

In the previous Sections we have already introduced several methods to calculate the Green function of the Anderson impurity model (Eq. [27]). This

is necessary for the DMFT self-consistently cycle (flow diagram Fig. 8), and quantum Monte Carlo (QMC) simulations allow to do so in a numerically exact way. For the Anderson impurity model, the QMC algorithm of Hirsch and Fye (286) is the efficient, well established approach. Hence, we will briefly review this QMC algorithm and a projective variant in the next two Sections.

Let us mention however that there has been a rapid development in the field of QMC algorithms for the Anderson impurity model most recently. In particular, continuous time QMC algorithms have been developed (287; 288; 289; 290; 291), based on a series expansions starting either from the non-interacting problem (287; 288) or the atomic limit (289). Also a combination of series expansion and Hirsch-Fye algorithm is possible (292). One of these new algorithms might supersede the hirthto standard Hirsch-Fye QMC approach in the future. In the present state of flux, it is not clear however which of the new algorithms or furthergoing ones will prevail.

5.5.1 Hirsch-Fye algorithm. In essence, the QMC technique maps the interacting Anderson impurity problem (Eq. [27]) onto a sum of non-interacting problems where the single particle moves in a fluctuating, time-dependent field. This sum is evaluated by Monte Carlo sampling, see the flow diagram Fig. 17 for an overview.

Trotter discretisation

Let us now discuss this approach in more detail. In a first step, the imaginary time interval $[0, \beta]$ of the functional integral Eq. [27] is discretised into Λ steps of size $\Delta\tau = \beta/\Lambda$, yielding support points $\tau_\lambda = \lambda\Delta\tau$ with $\lambda = 1 \dots \Lambda$. Using this Trotter discretisation, the integral $\int_0^\beta d\tau$ is transformed into the sum $\sum_{\lambda=1}^\Lambda \Delta\tau$ and the exponential terms in Eq. [27] can be separated via the Trotter-Suzuki (294) formula for operators \hat{A} and \hat{B}

$$e^{-\beta(\hat{A}+\hat{B})} = \prod_{\lambda=1}^{\Lambda} e^{-\Delta\tau\hat{A}}e^{-\Delta\tau\hat{B}} + \mathcal{O}(\Delta\tau), \quad (113)$$

which is exact in the limit $\Delta\tau \rightarrow 0$. The single site action \mathcal{A} of Eq. [29] can

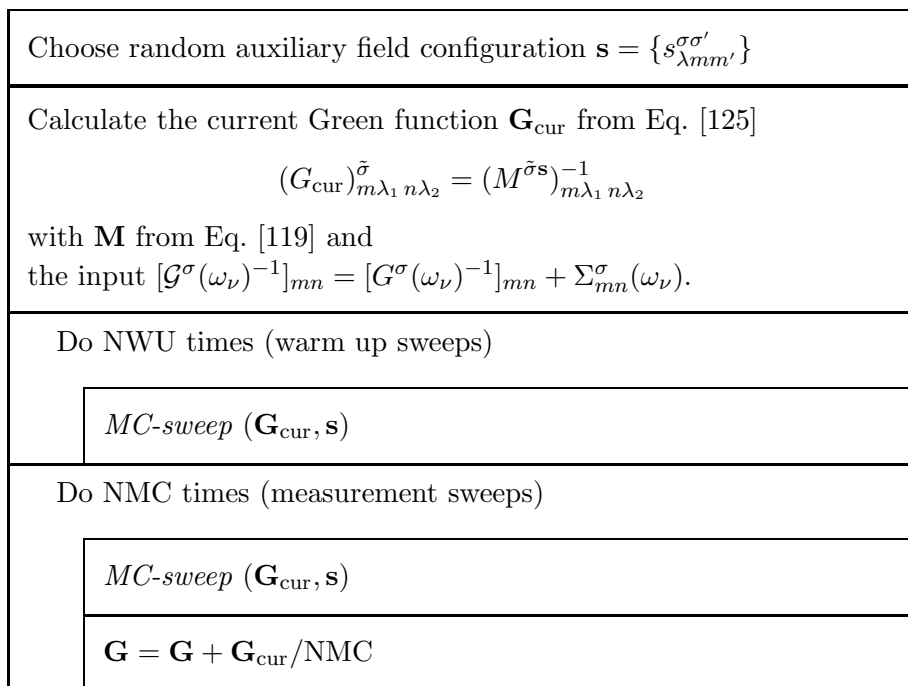


Figure 17. Flow diagram of the QMC algorithm to calculate the Green function matrix \mathbf{G} using the procedure *MC-sweep* of Fig. 18 [closely following (35)].

now be written in the discrete, imaginary time as

$$\begin{aligned}
 \mathcal{A}[\psi, \psi^*, \mathcal{G}^{-1}] &= \Delta\tau^2 \sum_{\sigma mn} \sum_{\lambda, \lambda'=0}^{\Lambda-1} \psi_{m\lambda}^{\sigma*} \mathcal{G}_{mn}^{\sigma-1} (\lambda\Delta\tau - \lambda'\Delta\tau) \psi_{n\lambda'}^\sigma \\
 &\quad - \frac{1}{2} \Delta\tau \sum_{m\sigma, m'\sigma'}' U_{mm'}^{\sigma\sigma'} \sum_{\lambda=0}^{\Lambda-1} \psi_{m\lambda}^{\sigma*} \psi_{m\lambda}^\sigma \psi_{m'\lambda}^{\sigma'*} \psi_{m'\lambda}^{\sigma'}. \quad (114)
 \end{aligned}$$

Here, the Coulomb interactions of the LDA+DMFT Hamiltonian [34], more specifically the inter-orbital and intra-orbital Coulomb repulsion and the Z -component of the Hund exchange interaction, were for convenience put into a

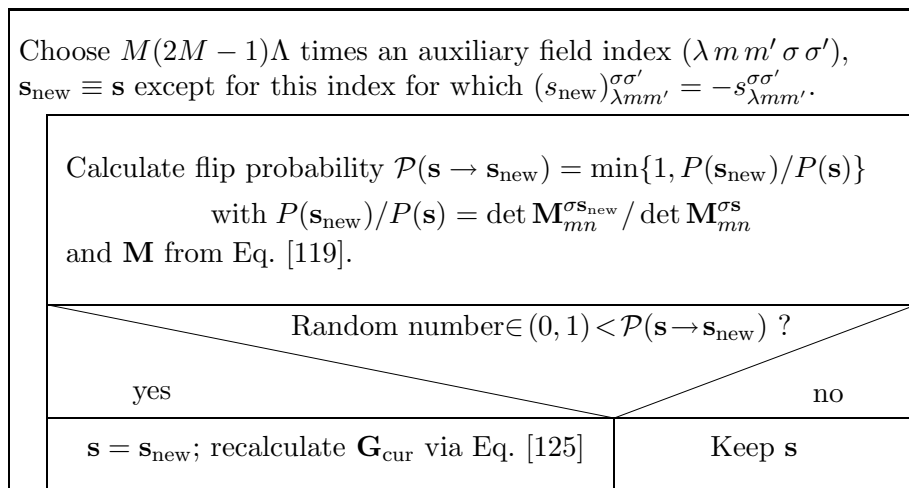


Figure 18. Procedure *MC-sweep* using the Metropolis(293) rule to change the sign of $s_{\lambda m m'}^{\sigma \sigma'}$. The recalculation of \mathbf{G}_{cur} , i.e. the matrix \mathbf{M} of Eq. [119], simplifies to $\mathcal{O}(\Lambda^2)$ operations if only one $s_{\lambda m m'}^{\sigma \sigma'}$ changes sign. Then, Eqs. [134] and [135] can be employed (closely following (35)).

unified form with

$$U_{mm'}^{\sigma \sigma'} = \begin{cases} 0 & \text{for } m = m' \text{ and } \sigma = \sigma' \\ U & \text{for } m = m' \text{ and } \sigma \neq \sigma' \\ V - J & \text{for } m \neq m' \text{ and } \sigma = \sigma' \\ V & \text{for } m \neq m' \text{ and } \sigma \neq \sigma' \end{cases}. \quad (115)$$

Also note, that the first term was Fourier-transformed from Matsubara frequencies in Eq. [29] to imaginary time.

Hubbard-Stratonovich transformation

In a second step, the $M(2M - 1)$ interaction terms (M denotes the number of interacting orbitals) of the single site action \mathcal{A} (Eq. [114]) are decoupled by

introducing a classical auxiliary field $s_{\lambda mm'}^{\sigma\sigma'}$:

$$\exp \left\{ \frac{\Delta\tau}{2} U_{mm'}^{\sigma\sigma'} (\psi_{m\lambda}^\sigma \psi_{m\lambda}^\sigma - \psi_{m'\lambda}^{\sigma'} \psi_{m'\lambda}^{\sigma'})^2 \right\} = \frac{1}{2} \sum_{s_{\lambda mm'}^{\sigma\sigma'} = \pm 1} \exp \left\{ \Delta\tau \mathcal{J}_{\lambda mm'}^{\sigma\sigma'} s_{\lambda mm'}^{\sigma\sigma'} (\psi_{m\lambda}^\sigma \psi_{m\lambda}^\sigma - \psi_{m'\lambda}^{\sigma'} \psi_{m'\lambda}^{\sigma'}) \right\}, \quad (116)$$

where $\cosh(\mathcal{J}_{\lambda mm'}^{\sigma\sigma'}) = \exp(\Delta\tau U_{mm'}^{\sigma\sigma'}/2)$. Since we need only one field for every pair of orbitals $[(m\sigma) \text{ and } (m'\sigma')]$ we can restrict the $s_{\lambda mm'}^{\sigma\sigma'}$ sum to one term per pair which is indicated by the prime. This so-called discrete Hirsch-Fye-Hubbard-Stratonovich transformation can be applied to the Coulomb repulsion as well as to the z -component of Hund's rule coupling, all included in $U_{mm'}^{\sigma\sigma'}$. One limitation of QMC is that it is very difficult to deal with terms which do not have this density-density type of form. In particular, a Hubbard-Stratonovich decoupling of the spin-flip term of Hund's rule coupling leads to a 'minus-sign problem', see Ref. (149). Therefore, this spin-flip term and the pair-hopping term, i.e. the second line of the LDA+DMFT Hamiltonian [34], are usually neglected. In the particle-hole symmetric case, another decoupling scheme which includes the spin-flip term is possible without 'minus-sign problem', see Ref. (295). More recently, also several new algorithms (296; 297; 287; 288; 289; 290; 291) have been introduced which include the spin-flip and pair-hopping terms. This is done by new kinds of Hubbard-Stratonovich transformations (296; 297) or series expansions (287; 288; 289; 291; 292). Hence, LDA+DMFT(QMC) calculations with the correct symmetry of the interaction should be possible in the future; first steps have already been taken (291).

By means of Eq. [116], we replace the interacting system by a sum of $\Lambda M(2M - 1)$ auxiliary fields $s_{\lambda mm'}^{\sigma\sigma'}$. This allows us to solve the functional integral by a simple Gauss integration since the Fermion operators only enter quadratically, i.e. for a given configuration $\mathbf{s} = \{s_{\lambda mm'}^{\sigma\sigma'}\}$ of the auxiliary fields the system is non-interacting. The quantum mechanical problem is then reduced to a matrix problem

$$G_{m\lambda_1 n\lambda_2}^{\tilde{\sigma}} = \frac{1}{\tilde{\mathcal{Z}}} \sum_{\lambda} \sum_{m'\sigma', m''\sigma''} \sum_{s_{\lambda m''m'}^{\sigma''\sigma'} = \pm 1} (M^{\tilde{\sigma}\mathbf{s}})^{-1}_{m\lambda_1 n\lambda_2} \det \mathbf{M}_{\tilde{m}\tilde{n}}^{\sigma\mathbf{s}}. \quad (117)$$

Here,

$$\mathcal{Z} = \sum_{\lambda} \sum'_{m'\sigma', m''\sigma''} \sum'_{s_{\lambda m''m'}^{\sigma''\sigma'} = \pm 1} \det \mathbf{M}_{mn}^{\sigma s} \quad (118)$$

is the partition function, the prime indicates that every distinct term is counted only once, the determinant includes the orbital, imaginary time and spin index, and $\mathbf{M}_{mn}^{\sigma s}$ is the following matrix in the imaginary time indices:

$$\mathbf{M}_{mn}^{\sigma s} = \Delta\tau^2 [(\mathbf{G}^{\sigma-1})_{mn} + \Sigma_{mn}^{\sigma}] e^{-\tilde{\mathcal{J}}_n^{\sigma s}} + \mathbf{1} - e^{-\tilde{\mathcal{J}}_n^{\sigma s}} \delta_{mn}. \quad (119)$$

The elements of the imaginary time matrix $\tilde{\mathcal{J}}_m^{\sigma s}$ are, in turn, given by

$$\tilde{\mathcal{J}}_{m\lambda\lambda'}^{\sigma s} = -\delta_{\lambda\lambda'} \sum_{m'\sigma'} \mathcal{J}_{mm'}^{\sigma\sigma'} \tilde{\sigma}_{mm'}^{\sigma\sigma'} s_{\lambda mm'}^{\sigma\sigma'}, \quad (120)$$

where $\tilde{\sigma}_{mm'}^{\sigma\sigma'} = 2\Theta(\sigma' - \sigma + \delta_{\sigma\sigma'}[m' - m] - 1)$ changes sign if $(m\sigma)$ and $(m'\sigma')$ are exchanged. For more details and a derivation why the matrix \mathbf{M} enters in Eq. [119], see Refs. (286; 299; 56).

Monte Carlo importance sampling

Since the sum in Eq. [117] consists of $2^{\Lambda M(2M-1)}$ addends, a complete summation for large Λ is computationally impossible. Therefore, the Monte Carlo method is employed, which is often an efficient way to calculate high-dimensional sums and integrals. In this method, the integrand $F(x)$ is split into a normalised probability distribution P and the remaining term O :

$$\int dx F(x) = \int dx O(x) P(x) \equiv \langle O \rangle_P \quad (121)$$

with

$$\int dx P(x) = 1 \quad \text{and} \quad P(x) \geq 0. \quad (122)$$

In statistical physics, the Boltzmann distribution is often a good choice for the function P :

$$P(x) = \frac{1}{\mathcal{Z}} \exp[-\beta E(x)]. \quad (123)$$

For the sum of Eq. [117], this probability distribution translates to

$$P(\mathbf{s}) = \frac{1}{\mathcal{Z}} \det \mathbf{M}_{mn}^{\sigma \mathbf{s}} \quad (124)$$

with the remaining term

$$O(\mathbf{s})_{m\lambda_1 n\lambda_2}^{\tilde{\sigma}} = [(M^{\tilde{\sigma} \mathbf{s}})^{-1}]_{m\lambda_1 n\lambda_2}. \quad (125)$$

Instead of summing over all possible configurations, the Monte Carlo simulation generates configurations x_i according to the probability distribution $P(x)$ and averages the observable $O(x)$ over these x_i . Therefore the relevant parts of the phase space with a large Boltzmann weight are taken into account to a greater extent than the ones with a small weight, coining the name *importance sampling* for this method. For \mathcal{N} statistically independent addends x_i drawn according to the probability $P(x)$ [this is indicated by $x_i \in P(x)$ in the following equation], one gets by virtue of the central limit theorem the following estimate

$$\langle O \rangle_P = \frac{1}{\mathcal{N}} \sum_{\substack{i=1 \\ x_i \in P(x)}}^{\mathcal{N}} O(x_i) \pm \frac{1}{\sqrt{\mathcal{N}}} \sqrt{\langle O^2 \rangle_P - \langle O \rangle_P^2}. \quad (126)$$

Here, the error and with it the number of needed addends \mathcal{N} is nearly independent of the dimension of the integral. The computational effort for the Monte Carlo method is therefore only rising polynomially with the dimension of the integral and not exponentially as in a normal integration. The so-called minus-sign problem occurs if the error [given by the variance in Eq. [126]] is large in comparison with the mean value. This happens particularly if $O(x)$ has contributions with positive and negative sign which almost cancel.

In order to pick configurations x with the proper probability $P(x)$, a Markov process is employed. Was x realised, a new configuration y is accepted with probability

$$\mathcal{P}(x \rightarrow y) = \min \{1, P(y)/P(x)\} \quad (127)$$

Since this transition probability by Metropolis *et al.* (293) fulfils the detailed balance

$$P(x)\mathcal{P}(x \rightarrow y) = P(y)\mathcal{P}(y \rightarrow x), \quad (128)$$

it guarantees that the series of configurations x obey the probability $P(x)$.

In our case, the probability ratio for deciding on the acceptance of a new auxiliary field configuration \mathbf{s}_{new} is given by

$$P(\mathbf{s}_{\text{new}})/P(\mathbf{s}) = \frac{\det \mathbf{M}_{mn}^{\sigma \mathbf{s}_{\text{new}}}}{\det \mathbf{M}_{mn}^{\sigma \mathbf{s}}}. \quad (129)$$

Single spin-flip updates

A very efficient algorithm is obtained by considering a new configuration of the auxiliary field (spins) \mathbf{s}_{new} which differs from the old one by only one component $(\lambda m m' \sigma \sigma')$: $\mathbf{s}_{\text{new}} = \mathbf{s}$ except for $(s_{\text{new}})_{\lambda m m'}^{\sigma \sigma'} = -s_{\lambda m m'}^{\sigma \sigma'}$. This dramatically reduces the effort to calculate the probability ratio which then only depends on three numbers:

$$P(\mathbf{s}_{\text{new}})/P(\mathbf{s}) = R_{mm\sigma}^{\mathbf{s}_{\text{new}}\mathbf{s}} R_{m'm'\sigma'}^{\mathbf{s}_{\text{new}}\mathbf{s}} - \delta_{\sigma\sigma'} R_{mm'\sigma}^{\mathbf{s}_{\text{new}}\mathbf{s}} \quad (130)$$

where

$$R_{mm\sigma}^{\mathbf{s}_{\text{new}}\mathbf{s}} = 1 + (1 - [(M^{\sigma\mathbf{s}})^{-1}]_{m\lambda m\lambda}) \underbrace{(e^{2\mathcal{J}_{\lambda m m'}^{\sigma\sigma'}} \tilde{\sigma}_{mm'}^{\sigma\sigma'} s_{\lambda m m'}^{\sigma\sigma'}}_{\equiv e^{\mathcal{J}}}, \quad (131)$$

$$R_{m'm'\sigma'}^{\mathbf{s}_{\text{new}}\mathbf{s}} = 1 + (1 - [(M^{\sigma'\mathbf{s}})^{-1}]_{m'\lambda m'\lambda}) (e^{-\mathcal{J}} - 1), \quad (132)$$

$$R_{mm'\sigma}^{\mathbf{s}_{\text{new}}\mathbf{s}} = [(M^{\sigma\mathbf{s}})^{-1}]_{m\lambda m'\lambda} (e^{-\mathcal{J}} - 1) [(M^{\sigma\mathbf{s}})^{-1}]_{m'\lambda m\lambda} (e^{\mathcal{J}} - 1). \quad (133)$$

Similarly one can show with some matrix algebra that the recalculation of $\mathbf{M}_{mn}^{\sigma \mathbf{s}_{\text{new}}}$ requires $\mathcal{O}(2M^2\Lambda^2)$ computational operations in two steps (without off-diagonal orbital-elements this reduces to $\mathcal{O}(2 \times \Lambda^2)$). The first step is

$$\begin{aligned} [(M_{1.}^{\sigma \mathbf{s}_{\text{new}}})^{-1}]_{\tilde{m}\lambda' \tilde{n}\lambda''} &= [(M^{\sigma\mathbf{s}})^{-1}]_{\tilde{m}\lambda' \tilde{n}\lambda''} + \frac{e^{\mathcal{J}} - 1}{R_{mm\sigma}^{\mathbf{s}_{\text{new}}\mathbf{s}}} \\ &\times ([(M^{\sigma\mathbf{s}})^{-1}]_{\tilde{m}\lambda' m\lambda} - \delta_{\lambda'\lambda} \delta_{\tilde{m}m}) [(M^{\sigma\mathbf{s}})^{-1}]_{m\lambda \tilde{n}\lambda''}. \end{aligned} \quad (134)$$

With the $\mathbf{M}_{1.}^{\sigma \mathbf{s}_{\text{new}}}$ from the 1. step, $R_{m'm'\sigma'}^{\mathbf{s}_{\text{new}}\mathbf{s}}$ is recalculated according to Eq. [132] and the second update incorporates the change because of m' :

$$\begin{aligned} [(M_{1.}^{\sigma' \mathbf{s}_{\text{new}}})^{-1}]_{\tilde{m}\lambda' \tilde{n}\lambda''} &= [(M_{1.}^{\sigma' \mathbf{s}_{\text{new}}})^{-1}]_{\tilde{m}\lambda' \tilde{n}\lambda''} + \frac{e^{-\mathcal{J}} - 1}{R_{m'm'\sigma'}^{\mathbf{s}_{\text{new}}\mathbf{s}}} \\ &\times ([(M_{1.}^{\sigma' \mathbf{s}_{\text{new}}})^{-1}]_{\tilde{m}\lambda' m'\lambda} - \delta_{\lambda'\lambda} \delta_{\tilde{m}m'}) [(M_{1.}^{\sigma' \mathbf{s}_{\text{new}}})^{-1}]_{m'\lambda \tilde{n}\lambda''}. \end{aligned} \quad (135)$$

Note that these equations hold if $G(\tau > 0)$ is negative, as in the standard definition for the Green function, and if $G(0) = G(\tau = 0-)$. Often in QMC, the Green function is defined differently, i.e. with the opposite (positive) sign.

Since roughly $M(2M - 1)\Lambda$ single spin flips have to be tried before arriving at a truly independent \mathbf{s}_{new} , the overall cost of the algorithm is

$$2M(2M - 1)M^2\Lambda^3 \times \text{number of MC-sweeps} \quad (136)$$

in leading order of Λ . It reduces considerably to

$$2M(2M - 1)\Lambda^3 \times \text{number of MC-sweeps} \quad (137)$$

if orbital off-diagonal elements are zero.

The advantage of the QMC method (for the algorithm see the flow diagrams Figs. 17 and 18) is that it is (numerically) exact. It allows one to calculate the one-particle Green function as well as two-particle (or higher) Green functions. On present workstations the QMC approach is able to deal with up to seven *interacting* orbitals and room temperature or higher temperatures, for typical values of the Coulomb interaction U and the LDA bandwidth W . Since the QMC approach calculates $G(\tau)$ or $G(i\omega_n)$ with a statistical error, it also requires an analytical continuation to obtain the Green function $G(\omega)$ at real (physical) frequencies ω or the physically relevant spectral function $A(\omega) = -\frac{1}{\pi}\text{Im}G(\omega)$, see Section 5.5.4. Very low temperatures are not accessible in QMC because the numerical effort grows as $\Lambda^3 \sim 1/T^3$. For these low temperatures or zero temperature, a projective QMC method was developed recently. We will discuss this variant in the next Section.

5.5.2 Projective quantum Monte Carlo (PQMC) simulations for $T = 0$.

Often interesting many-body physics occurs at low temperatures. In this case, the Hirsch-Fye (286) QMC algorithm, which was introduced in the previous Section, is not applicable as discussed above. For lattice QMC simulations an alternative projective quantum Monte Carlo (PQMC) method was developed by White *et al.* (300). This PQMC algorithm converges, according to Assaad and Imada (301), faster to the groundstate than the finite temperature lattice QMC algorithm of Blankenbecler *et al.* (302). The general idea of the PQMC is to start with a trial wave function $|\Psi_0\rangle$ and to project onto the ground state $|\Psi_{\text{GS}}\rangle$ via

$$|\Psi_{\text{GS}}\rangle = \lim_{\theta \rightarrow \infty} \frac{e^{-\theta/2 \hat{H}} |\Psi_0\rangle}{\sqrt{\langle \Psi_0 | e^{-\theta \hat{H}} | \Psi_0 \rangle}}. \quad (138)$$

If $|\Psi_0\rangle$ has any overlap with the (unique) ground state only this state with the lowest energy and, hence, the largest contribution to $e^{-\theta \hat{H}}$ will prevail in

the limit $\theta \rightarrow \infty$. In the DMFT context, one often calculates the Anderson impurity model in the thermodynamic limit with an infinite number of bath sites $N \rightarrow \infty$. In this case, ground state and low-lying excited states have the same energy to leading order in $1/N$ and yield the same Green function. Hence, we can project onto such low-lying excited states and obtain the correct Green function and other expectation values, so that Anderson's orthogonality catastrophe (303; 304; 305) is irrelevant for the PQMC algorithm, as was shown by Feldbacher *et al.* (306).

With the ground state given by Eq. [138], zero temperature observables can be calculated as follows:

$$\langle \hat{\mathcal{O}} \rangle = \langle \Psi_{\text{GS}} | \hat{\mathcal{O}} | \Psi_{\text{GS}} \rangle = \lim_{\theta \rightarrow \infty} \frac{\langle \Psi | e^{-\theta/2 \hat{H}} \hat{\mathcal{O}} e^{-\theta/2 \hat{H}} | \Psi_0 \rangle}{\langle \Psi_0 | e^{-\theta \hat{H}} | \Psi_0 \rangle}. \quad (139)$$

For a finite value of θ , this expectation value can be calculated by (projective) QMC simulations which decouple the projector $e^{-\theta/2 \hat{H}}$ by Hubbard-Stratonovich transformations, after discretising the imaginary time.

Let us now focus on the Anderson impurity model for which Feldbacher *et al.* (189) developed a new PQMC method. This PQMC is related to the one of White *et al.* (300) for lattice many-body systems in a similar way as the QMC of Hirsch and Fye (286) to that of Blankenbecler *et al.* (302) for lattice QMC. The biggest difference is that, for the Anderson impurity model, one is dealing with matrices in the imaginary time index, instead of matrices in the lattice indices for the lattice QMC algorithm of Blankenbecler *et al.* (302): The Hirsch-Fye algorithm is directly formulated in terms of the non-interacting Green function of the Anderson impurity model \mathcal{G}^0 . Within the DMFT iteration scheme, we usually do not even define a lattice for the auxiliary Anderson impurity model anymore. This leads to the difficulty of how to define the trial wave function which for a lattice problem is a more straightforward task.

Feldbacher *et al.* (189) overcame this difficulty by considering instead of Eq. [139] an artificial finite temperature problem:

$$\langle \hat{\mathcal{O}} \rangle_{\theta} = \lim_{\beta \rightarrow \infty} \frac{\text{Tr} e^{-\beta/2 \hat{H}_0} e^{-\theta/2 \hat{H}} \hat{\mathcal{O}} e^{-\theta/2 \hat{H}_{\text{AIM}}} e^{-\beta/2 \hat{H}_0}}{\text{Tr} e^{-\beta \hat{H}_0} e^{-\theta \hat{H}_{\text{AIM}}}}. \quad (140)$$

In the limit $\beta \rightarrow \infty$, this projects onto the ground state of the Hamilton operator \hat{H}_0 . If this ground state is $|\Psi_0\rangle$ and has energy E_0 we have

$$\lim_{\beta \rightarrow \infty} \text{Tr} e^{-\beta \hat{H}_0} \hat{\mathcal{O}} \rightarrow e^{-\beta E_0} \langle \Psi_0 | \hat{\mathcal{O}} | \Psi_0 \rangle. \quad (141)$$

Hence, the finite temperature problem of Eq. [140] becomes equivalent to the

projection of Eq. [139].

As a special case of Eq. [140], the θ -projected Green function is given by

$$G_{lm}(\tau, \tau') = -\langle T c_l(\tau) c_m^\dagger(\tau') \rangle \quad (142)$$

$$= \frac{\langle \Psi_0 | T e^{-\theta \hat{H}_{\text{AIM}}} c_l(\tau) c_m^\dagger(\tau') | \Psi_0 \rangle}{\langle \Psi_0 | e^{-\theta \hat{H}_{\text{AIM}}} | \Psi_0 \rangle} \quad (143)$$

$$= \lim_{\beta \rightarrow \infty} \frac{\text{Tr} T e^{-\beta \hat{H}_0} e^{-\theta \hat{H}_{\text{AIM}}} c_l(\tau) c_m^\dagger(\tau')}{\text{Tr} e^{-\beta \hat{H}_0} e^{-\theta \hat{H}_{\text{AIM}}}}. \quad (144)$$

Here, T is the Wick time ordering operator for the τ 's and $\hat{\mathcal{O}}(\tau) = e^{\tau \hat{H}} \hat{\mathcal{O}} e^{-\tau \hat{H}}$ as before.

A natural choice for the trial wave function is the ground state of a non-interacting Anderson impurity model [$U = 0$ in Hamiltonian [26]]. As was shown by Feldbacher *et al.* (189), one then arrives at the same algorithm as the Hirsch-Fye finite temperature algorithm. The only difference is that in Eq. [119], instead of the finite temperature $(\mathcal{G}^0)^{-1} = \mathbf{G}^{-1} + \Sigma$, a zero temperature $(\mathcal{G}^0)^{-1}$ enters as a $\Lambda \times \Lambda$ matrix. While at half-filling the finite temperature $\mathcal{G}_{mm}^0(\tau, 0)$ decreases (in terms of the absolute value) from $\tau = 0$ to $\tau = \beta/2$ and increases again from $\tau = \beta/2$ to $\tau = \beta$, the zero temperature $\mathcal{G}_{mm}^0(\tau, 0)$ continues to decrease from $\tau = \theta/2$ to $\tau = \theta$.

With these rather small changes to the QMC code, PQMC simulations are possible. In contrast to the finite temperature QMC, there are no thermal fluctuations. This is the reason why these PQMC calculations converge much faster to the ground state properties (as a function of θ) than the Hirsch-Fye QMC (as a function of β which corresponds to the same numerical effort). Let us mention that similar projective QMC versions of the continuous time QMC algorithms (287; 288; 289) are possible (298).

5.5.3 Fourier transformation from τ to $i\omega_\nu$. In the previous two Sections, we have introduced the Hirsch-Fye QMC and projective QMC simulations for the Anderson impurity model. In the context of DMFT, this Anderson impurity model is determined self-consistently, see flow diagram Fig. 8. While the Dyson equation [32] of this self-consistency is formulated in terms of Matsubara frequencies, the QMC calculations of the Anderson impurity model use a discrete set of Λ imaginary time support points. Hence, we have to overcome a final technical obstacle: the Fourier transformation from τ to $i\omega_\nu$ and vice versa. This is in particular problematic since we have only a limited number Λ of τ points, which only allow us to calculate the Green function for an equal number of Matsubara frequencies by means of a discrete Fourier

transformation. On the other hand, the tail at high Matsubara frequencies is important since it is responsible for the jump of the Green function at $\tau = 0$: $G_{lm}(\tau = 0^+) = -\delta_{lm} + G_{lm}(\tau = 0^-)$.

Therefore, a discrete Fourier transformation does not work. It would yield a Green function which oscillates considerably around the correct $\mathcal{G}(\tau)$. Different paths are used in the literature to overcome this obstacle:

Georges *et al.* (56) do a spline interpolation of $\mathbf{G}(\tau)$, resulting in arbitrarily many support points and, hence, enough Matsubara frequencies. Jarrell (299) extend the number of Matsubara frequencies by employing the iterated perturbation theory result at high frequencies.

Ulmke *et al.* (104) use a smoothing procedure which replaces $\mathcal{G}_{mm}^0(i\omega_\nu)$ by

$$\tilde{\mathcal{G}}_{mm}^0(i\omega_\nu) \equiv \frac{\Delta\tau}{1 - \exp[-\Delta\tau/\mathcal{G}_{mm}(i\omega_\nu)]}. \quad (145)$$

This $\tilde{\mathcal{G}}^0$ is Fourier transformed to imaginary time, and this Fourier transform is in turn used as the non-interacting Green function of the Anderson impurity model. After the QMC simulation yielded the output $\tilde{G}_{mm}(\tau_\lambda)$, the process is reversed: From the Fourier transform of $\tilde{G}_{mm}(\tau_\lambda)$, i.e. $\tilde{G}_{mm}(i\omega_\nu)$, the inverse of Eq. [145] yields $G_{mm}(i\omega_\nu)$. The new self energy is then $\Sigma_{mm}(i\omega_\nu) = \mathcal{G}_{mm}(i\omega_\nu)^{-1} - G_{mm}(i\omega_\nu)^{-1}$. This approach generates smooth Green functions $G(\tau_\lambda)$ and reproduces the correct $\Delta\tau \rightarrow 0$ limit.

In their implementation, McMahan *et al.* (229) use a constrained fit to the output QMC impurity Green function $G(\tau_\lambda)$:

$$G(\tau) = \sum_i w_i f_i(\tau). \quad (146)$$

The basis functions are $f_i(\tau) = -e^{-\varepsilon_i\tau}/(e^{-\beta\varepsilon_i}+1)$ and have Fourier transforms $f_i(i\omega) = 1/(i\omega - \varepsilon_i)$, hence allowing for determining $G(i\omega_\nu)$ at $N_\omega > \Lambda$ Matsubara frequencies. The difference to the spline-fit is that in Eq. [146] every fit coefficient is determined by the local behaviour in a frequency interval, not by the local behaviour in an imaginary time interval.

The fit of Eq. [146] has some additional constraints: $w_i \geq 0$, $G(0^+)$ is precisely the QMC value, $G(0^+) + G(\beta^-) = -1$, and $\frac{d}{d\tau}G(0^+) + \frac{d}{d\tau}G(\beta^-) = g_2$, where g_m is the $(i\omega)^{-m}$ high-frequency moment of $G(i\omega)$. For the last constraint, the second moment g_2 is obtained from the relation $G^{-1}(i\omega) = \mathcal{G}^{-1}(i\omega) - \Sigma(i\omega)$ which implies $g_2 = g_2 + s_0$, where these are the indicated moments of $G(i\omega)$, $\mathcal{G}(i\omega)$, and $\Sigma(i\omega)$, respectively. Note that g_2 is known since \mathcal{G} is input to the QMC, and for s_0 the analytical high frequency behaviour (known from the Hartree Fock) is taken: $s_0 = \Sigma(\omega = \infty) = \Sigma^{\text{Hartree-Fock}}$. For M degenerate orbitals and without Hund's exchange coupling this is: $s_0 = 2M - 1/2M[1 + G(\tau =$

$0^+)]U$. Using these constraints and $\Lambda/4$ equally spaced ε_i , the agreement between Eq. [146] with the QMC data for $G(\tau)$ is optimised.

For a faster convergence, McMahan *et al.* (229) also separated the self energy $\Sigma^{\text{QMC}}(i\omega) = \Delta\Sigma(i\omega) + \Sigma^{\text{Hartree-Fock}}$ into a constant Hartree-Fock contribution and a frequency-dependent rest $\Delta\Sigma(i\omega)$. After every QMC calculation, the authors did computationally inexpensive iterations during which $\Delta\Sigma(i\omega)$ was kept fix, but $\Sigma^{\text{Hartree-Fock}}$ and the number of interacting electrons were adjusted self-consistently until convergence.

For the PQMC simulations discussed in the previous Section, the Fourier transformation is even more challenging since the zero temperature Green functions extend from 0 to ∞ , instead of 0 to β at finite temperatures $T = 1/\beta$. With the Green function known only at Λ discrete τ points, one has not only to interpolate between the τ points as for finite temperatures but also to extrapolate to $\tau = \infty$. To this end, Feldbacher *et al.* (189) employed the maximum entropy method (see Section 5.5.4) which allows us to calculate from Λ support points the zero temperature spectral function $A(\omega)$ at real valued frequencies. From this spectra function, the Green function at any Matsubara frequency ω_ν can be easily calculated as

$$G(i\omega_\nu) = \int d\omega \frac{A(\omega)}{i\omega_\nu - \omega}. \quad (147)$$

5.5.4 Maximum entropy method. Since, in QMC, the Green function is calculated on the imaginary (Matsubara) axis, we have to do an analytical continuation to real frequencies for getting the spectral function $A(\omega) = -\frac{1}{\pi}\text{Im}G(\omega)$ which is of direct physical interest since it can be measured, e.g. by photoemission experiments. Because of the statistical QMC error, the standard approach for doing the analytical continuation is the maximum entropy method. In the following the basic concept will be briefly discussed, for a detailed review by Jarrell and Gubernatis see (188).

Starting point is the Fourier-transform of the spectral representation of the Green function

$$G(\tau) = \int_{-\infty}^{\infty} d\omega \frac{e^{\tau(\mu-\omega)}}{1 + e^{\beta(\mu-\omega)}} A(\omega). \quad (148)$$

This equation already shows that the analytical continuation is an ill-conditioned problem: The kernel of Eq. [148] is very small for large frequencies ω so that large changes in $A(\omega)$ have only a small impact on $G(\tau)$.

In this problematic situation, the maximum entropy method is used. It starts

with the entropy

$$S = - \int_{-\omega_0/2}^{\omega_0/2} d\omega A(\omega) \ln [A(\omega) \omega_0] \quad (149)$$

as the *a priori* probability $P(A) \sim \exp(TS)$ for a given spectrum $A(\omega)$, with adjustable parameter T . Besides this constant *a priori* probability, $A(\omega)$ has to yield the QMC-calculated $G(\tau)$. How good this is achieved can be measured by the usual χ^2 value for the quadratic difference between given (calculated) $G(\tau)$ and the one obtained from $A(\omega)$ via Eq. [148]. This χ^2 value gives the conditional probability for $G(\tau)$ with a given $A(\omega)$:

$$P(G|A) = e^{-\frac{1}{2}\chi^2}, \quad (150)$$

Following the Bayes theorem *a priori* and conditional probability yield the *a posteriori* probability for having a spectrum $A(\omega)$ if $G(\tau)$ was calculated in QMC:

$$P(A|G) \sim P(G|A)P(A) \sim e^{TS - \frac{1}{2}\chi^2}. \quad (151)$$

The result of the maximum entropy method is the most likely spectrum $A(\omega)$, maximising $P(A|G)$. This is a well defined statistical method for doing the analytical continuation. Because of the statistical error in the QMC and because Eq. [148] is ill conditioned for large $|\omega|$ the maximum entropy can however not resolve fine details at large frequencies, i.e. in the Hubbard band. In contrast, features at small frequencies, such as height and width of the central peak, and the overall weight and position of the Hubbard bands are reliable.

5.6 Comparing different DMFT solvers for $\text{La}_{1-x}\text{Sr}_x\text{TiO}_3$

After the discussion of different methods X to solve the DMFT self-consistency equations in the previous Sections, let us now compare how this solver reflects in the LDA+DMFT(X) results for a specific material: $\text{La}_{1-x}\text{Sr}_x\text{TiO}_3$. Such a comparison has been carried out by Nekrasov *et al.* (159), and we will recapitulate their findings here. The stoichiometric compound LaTiO_3 is a cubic perovskite with a small orthorhombic distortion (the distorted angle is $\angle \text{Ti-O-Ti} \approx 155^\circ$; see Ref. (307)), and is an antiferromagnetic insulator below $T_N = 125$ K (308; 309). Above T_N , or at low Sr-doping x , LaTiO_3 is a strongly correlated, but—except for the distortion—simple paramagnet with one $3d$ electron on the trivalent Ti sites. Since the aim of this Section is the

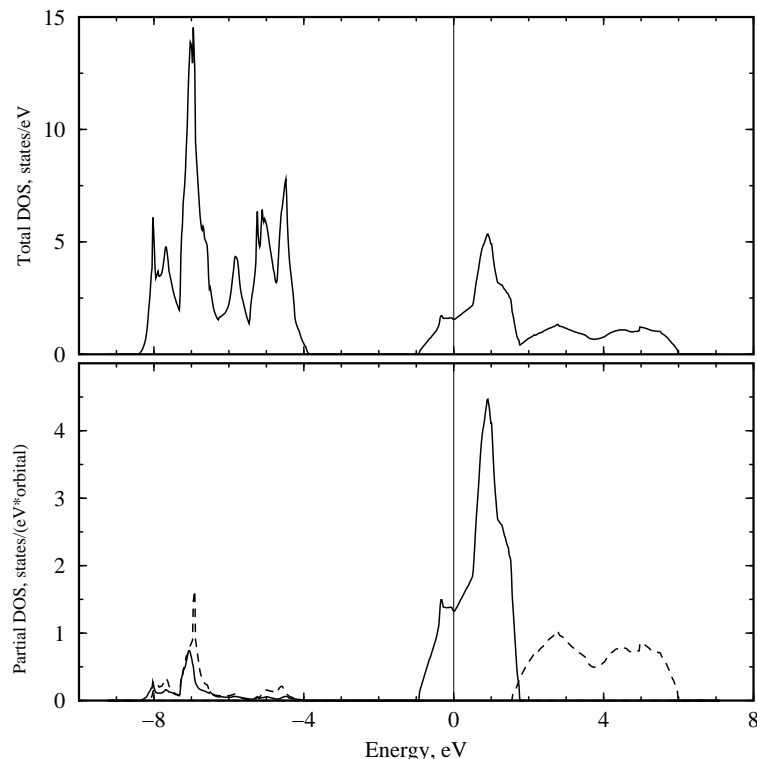


Figure 19. Densities of states of LaTiO_3 calculated with LDA-LMTO. Upper figure: total DOS; lower figure: partial t_{2g} (solid lines) and e_g (dashed lines) DOS (reproduced from Ref. (159)).

comparison of DMFT solvers we neglect the small orthorhombic distortion, i.e. consider a cubic structure with the same volume.

LDA calculations for the cubic crystal structure

Fig. 19 shows the LDA DOS for undoped LaTiO_3 . Thereby, Anisimov *et al.* (31) and Nekrasov *et al.* (159) approximated the crystal structure by a cubic one with the same volume. LDA+DMFT calculations including the orthorhombic distortion have been recently carried out by Pavarini *et al.* (310; 311) and Craco *et al.* (312). Here however, our main goal is the comparison of different DMFT solvers in a realistic material calculation. For this intercomparison the approximate cubic structure is sufficient.

In Fig. 19, the oxygen bands range from -8.2 eV to -4.0 eV and are completely filled so that Ti is three-valent. The cubic crystal field splits the Ti $3d$ bands into two empty e_g -bands and three degenerate t_{2g} -bands, well separated from the other bands. For the low-energy behaviour it is hence possible to restrict ourselves to these degenerate t_{2g} orbitals within the approximation introduced in Section 4.1.5, i.e. using the LDA DOS (Eq. [69]) instead of the

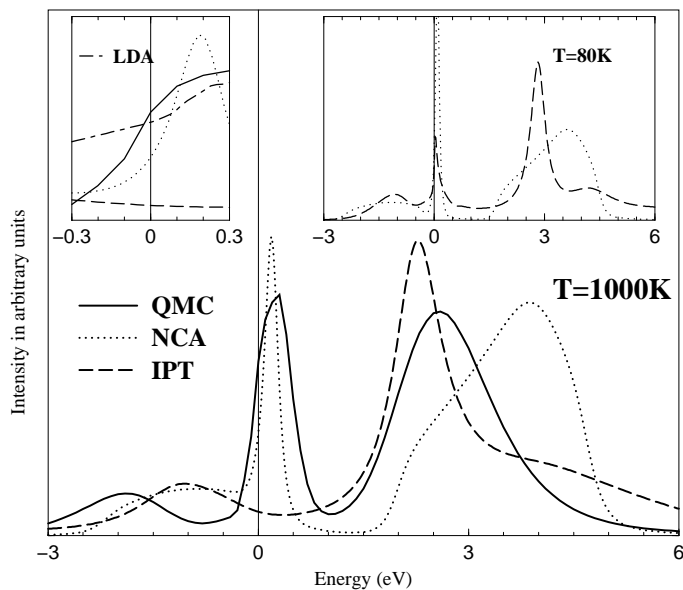


Figure 20. Spectrum of $\text{La}_{0.94}\text{Sr}_{0.06}\text{TiO}_3$ as calculated by LDA+DMFT(X) at $T = 0.1$ eV (≈ 1000 K) and $U = 4$ eV employing the approximations $X=\text{IPT}$, NCA and numerically exact QMC. Inset left: Behaviour at the Fermi level including the LDA DOS. Inset right: $X=\text{IPT}$ and NCA spectra at $T = 80$ K (reproduced from Ref. (159)).

full one-particle Hamiltonian H_{LDA}^0 of (Eq. [32]). We take Sr-doping x into account by adjusting the LDA+DMFT chemical potential to $n = 1 - x = 0.94$ t_{2g} electrons.

Method matters

In Fig. 20, we present the LDA+DMFT(X) spectrum of $\text{La}_{0.94}\text{Sr}_{0.06}\text{TiO}_3$, calculated for the impurity solvers $X=\text{IPT}$, NCA and QMC. Qualitatively, all three methods X yield the characteristic three peak structure, consisting of lower Hubbard band, quasiparticle peak and upper Hubbard band.

Quantitatively, however, we see pronounced differences: The IPT quasiparticle peak is very narrow and hence not visible at high temperatures (in the main panel), also the shape of the IPT Hubbard bands is different. NCA is much closer to the (numerically) exact QMC result than IPT, but nonetheless underestimates the width of the quasiparticle peak by a factor of two. NCA also violates the Luttinger pinning of the spectral function (66), a known deficit (313) seen clearly in the left inset, and puts the lower Hubbard band to close to the Fermi energy. The comparison of Fig. 20 hence shows that, at least on a quantitative level, it *matters* which *method* is employed as an impurity solver for the DMFT equations.

6 Realistic material calculations with DMFT

In this Section, we will review those electronic structure calculations which have been accomplished hitherto using DMFT for actual material calculations. The results are subdivided into different material classes: f electron systems in Section 6.1, transition metals in Section 6.2, their oxides in Section 6.3 and other materials in Section 6.4. Some highlights are discussed in more detail. Not discussed are LDA+U calculations, which would require a review on its own, and model DMFT calculations without material-specific LDA or GW input.

6.1 f electron systems

The state-of-the-art LDA+DMFT calculations for f -electron systems take into account all *spdf* valence orbitals and all hybridizations between them, but restrict the DMFT Coulomb interaction to the f orbitals in the LDA+DMFT Hamiltonian (Eq. [34]). This is a very reasonable starting point since the *spd* orbitals are much more extended and hence less strongly interacting. Whether the interaction of the d electrons leads to corrections, which cannot be completely ignored, remains however an open question since presently a DMFT calculation with all 24 interacting d and f orbitals would be too involved, at least when using a more rigorous impurity solver.

Two of the very early successes of LDA+DMFT were the calculations of the Mott transition in plutonium by Savrasov, Kotliar and Abrahams (165) and of the cerium volume collapse transition by Zöhl *et al.* (280) and Held, McMahan and Scalettar (154). Savrasov *et al.* (165; 150; 314) studied the δ -phase of Pu which is not well described by LDA, as is evident from the underestimation of the Pu volume by 30%. Within LDA+DMFT, electronic correlations drive the system towards a Mott transition. With these strong electronic correlations and a Coulomb interaction of $U \approx 4$ eV, the volume of δ -Pu comes out correctly (165). Subsequently, Dai *et al.* (315) extended these calculations by including lattice dynamics, allowing for the determination of the first LDA+DMFT phonon spectrum. This theoretical prediction well agrees with the later experiments (316). Concerning the magnetic properties of δ Pu, Pourovskii *et al.* (317) predicted the absence of dynamical and static magnetic moments in agreement with experiment. A detailed review of these activities, which are of possible relevance for nuclear waste (165), can already be found in Ref. (40). Hence, we will not discuss these calculations in more detail here. But let us mention that, more recently, also americium (318), PuCoGa₅ (319), different actinide monochalcogenides (320), Pu and Am compounds (321), and the rare earth elements Nd and Pr (322) have been investigated. In Ref. (322), also the effect of the spin-orbit coupling, which

is certainly important for f electron systems, was taken into account. Also, one of the very first LDA+DMFT(Hubbard-I) calculations was for the mixed valence 4f material TmSe (32).

6.1.1 Volume collapse transition in cerium. Let us now discuss in detail elemental cerium, the material hitherto most intensively studied with LDA+DMFT by various groups: Zöhl *et al.* (280), McMahan *et al.* (154; 229; 322), Haule *et al.* (283), and Amadon *et al.* (323). Under pressure, Ce undergoes the volume collapse, or α - γ transition, with a volume change of 15% at room temperature. This transition is isostructural within the face-centred-cubic (fcc) lattice structure and fades away for temperatures above the critical point at $T = 600 \pm 50$ K (324), for reviews see (324; 325; 326; 327). The volume collapse reflects in a dramatic transfer of spectral weight: In the α phase there is a large peak at the Fermi energy; whereas this peak is very much reduced in the γ phase, albeit there is still some spectral weight at the Fermi energy as to be expected for a metal. In accord with these findings, the optical conductivity is higher in the α phase where the frequency dependent scattering rate is characteristic for a Fermi liquid behaviour with an effective mass of about $20 m_e$, see Ref. (328). Concerning the magnetic susceptibility, α Ce behaves like a Pauli paramagnet at room temperature but has a Curie-Weiss form at higher temperatures and in the γ phase (324). Despite these dramatic differences in the spectrum, optical conductivity, and susceptibility, the number of 4f electrons does not change significantly and is close to one across the α - γ phase transition, as was revealed by Myon decay experiments (324).

Although some alternative theories have been proposed, see e.g. (329; 330; 331), the general belief is that the α - γ transition has an electronic origin. The first electronic theory, the promotional model (332; 333), which assumed the electronic configuration to change from $4f^0(sp d)^4$ in α Ce to $4f^1(sp d)^3$ for the γ phase, was however dismissed since it is at odds with the above mentioned Myon experiments and also with LDA calculations (334). Instead, Johansson (334) proposed a Mott transition (MT) model for the 4f electrons, assuming the 4f electrons in the α phase to be itinerant whereas they are localised (Mott insulating) in the γ phase which has a reduced LDA 4f bandwidth. Of course, γ Ce as a material remains metallic due to the other ($sp d$) electrons. In subsequent efforts to treat this scenario within LDA, Johansson (335) employed standard LDA calculations for the α phase and treated the 4f electrons in the γ phase as localised spins. Qualitatively, this yields similar results as the more sophisticated self-interaction corrected LDA calculation and the LDA+U method which were later performed (336; 337; 338; 339; 340) along with orbitally polarised calculations (341; 342; 336).

At the time Johansson was working out the MT scenario, another phe-

nomenon of electronic correlations was finally understood: the Kondo effect. Based on the physics of the Anderson impurity model, Allen and Martin (343; 344) proposed a Kondo volume collapse (KVC) scenario for the α - γ transition which appeared to be in conflict with the MT scenario. Both pictures agree that, at the experimental temperatures, the large volume γ phase has strongly correlated (localised) $4f$ electrons with a $4f^1$ moment and a Curie-Weiss magnetic susceptibility. But they differ considerably for α Ce: The MT scenario of Johansson assumes a weakly correlated (itinerant) α phase, with a ‘single’ peak at the Fermi energy in the $4f$ spectrum as on the left hand side of Fig. 2, only with some additional structures. As in the LDA, this itinerant phase has no $4f^1$ moment at all. The KVC scenario on the other hand assumes continued strong correlation in the α phase with a three peak structure, including a central Abrikosov-Suhl resonance and two side peaks at considerably higher and lower energies (345), as in the middle of Fig. 2. While the MT scenario envisages the coexistence of two phases and a first order transition between these, the KVC assumes the f -valence hybridisation to increase upon pressure so that the Kondo temperature which depends exponentially on this hybridisation changes dramatically. This leads to a correlation contribution to the energy (which is roughly proportional to the Kondo temperature) with a negative curvature as a function of volume. Therefore, one can lower the energy with a mixed low and high volume phase by a Maxwell (tangent) construction (343; 344), indicating a first order transition similar to the vapour-liquid transition. Attempts to do realistic material calculations on the basis of this KVC scenario started with Ref. (345) and were later continued (346; 347). In these calculations, the f -valence hybridisation is determined from LDA followed by a many-body treatment of the Anderson impurity model with the seven $4f$ orbitals.

Studying the Hubbard model and the periodic Anderson model¹ which are the simplest models for the MT and KVC scenario, respectively, Held *et al.* (348; 349) more recently stressed the similarity of these two models within DMFT and, hence, the MT and KVC scenarios. Actually, one can integrate out the valence electrons of the periodic Anderson model, resulting in an effective one-orbital model such as the Hubbard model but with a frequency dependent kinetic energy term. Hence, it might not be surprising that also the physics of the two models is very much the same: The spectrum shows a three peak structure with a lower and an upper Hubbard band and a central quasi-particle resonance in between. The local moment of the α phase is screened at low energies for both the Hubbard and the periodic Anderson model. This shows that the differences between the MT and the KVC scenario are due to

¹While the KVC is based on the Anderson impurity model, a more realistic treatment should start with its periodically extended version since the $4f$ electrons on every Ce site interact.

the LDA treatment of the α phase: In the α phase, the MT scenario misses electronic correlations and, therefore, the three peak structure of the spectrum. While many physical aspects of these models are similar, there are also some notable differences. In particular, there is no Mott-Hubbard transition in the periodic Anderson model at zero temperature, even though the finite temperature behavior is very similar to that of the Hubbard model including a region of two coexisting phases, i.e. metal and insulator (350).

Following these model studies, realistic LDA+DMFT calculations provided for an accurate *ab-initio* description of Ce. Fig. 21 (left panel) shows the evolution of the \mathbf{k} -integrated $4f$ spectral function with increasing volume. At a very small volume, $V = 20 \text{ \AA}^3$, most of the spectral weight is in a central quasiparticle peak or Abrikosov-Suhl resonance at the Fermi energy, similar as in the LDA. But, Hubbard side structures are already discernible, indicating that there are already electronic correlations, albeit these are not yet extraordinarily strong. With increasing volume, more and more spectral weight is transferred to the Hubbard side bands; electronic correlations increase. Approaching the experimental volumes of the α - γ transition, which occurs between 28.2 and 34.4 \AA^3 at room temperature, the three peak structure becomes much more pronounced: We see a sharp quasiparticle resonance at $V = 29 \text{ \AA}^3$. From the experimental α to the experimental γ phase volume (from $V = 29 \text{ \AA}^3$ to 34 \AA^3 in Fig. 21), the weight of the quasiparticle peak shrinks dramatically and fades away at even larger volumes. This large volume phase with a two peak structure can also be described by LDA+DMFT(Hubbard-I) and LDA+U calculations (not shown). Across the transition from γ to α Ce, also the local magnetic moment $\langle m_Z^2 \rangle$ is reduced by 5% (229) but not lost, in contrast to the Mott transition scenario of Johansson (335).

Adding the *spd* valence spectrum to the $4f$ spectrum and multiplying with the Fermi (inverse Fermi) function, the total LDA+DMFT spectrum is compared to the photoemission spectroscopy (PES) spectrum (351) below the Fermi energy and to the Bremsstrahlung isochromatic spectroscopy (BIS) (352) spectrum above the Fermi energy in Fig. 21 (right panel). The agreement between theory and experiment is very good. Note, that there are no free parameters in the LDA+DMFT(QMC) results of McMahan, Held and Scalettar (353; 229) since the f -electron Coulomb interaction and the double counting correction have been determined by constrained LDA calculations and the experimental resolution has been taken from (280). Particularly good is the agreement of the quasiparticle peak around the Fermi energy for both α and γ Ce, but also the position of the upper and lower Hubbard bands are approximately correct. The biggest differences can be found in the upper band which is broader in experiment and has some inner structure. It was argued (280; 229) that this is due to the Hund exchange interaction which was neglected in both, LDA+DMFT(NCA) (280) and LDA+DMFT(QMC)(229),

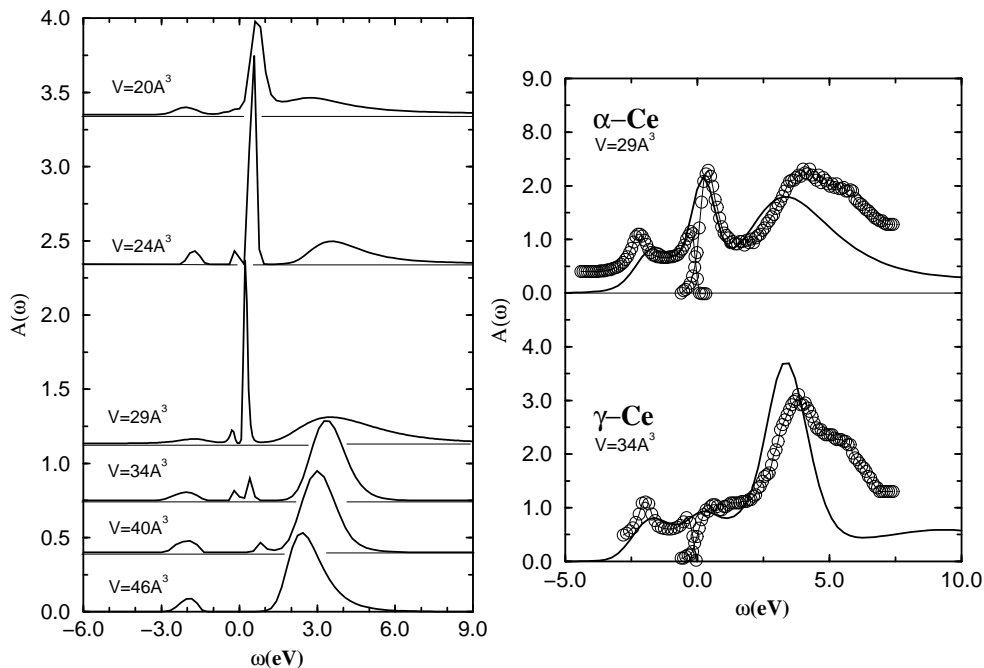


Figure 21. Left: Evolution of the $4f$ spectral function $A(\omega)$ with volume at $T = 632$ K. The curves at different volumes are shifted as indicated by the base line. When going from small to large volumes, the weight of the central quasiparticle peak is dramatically reduced at volumes corresponding to the experimental α - γ transition from $V = 29$ to 34 \AA^3 . Right: Comparison of the parameter-free LDA+DMFT(QMC) spectrum with experiment (circles), as collected in Ref. (345) (reproduced from (229)).

calculations. This exchange interaction has only a minor effect for the occupied states since these consist mainly of single occupied configurations. But, it is important for the upper Hubbard band because the Hund exchange splits these doubly occupied states into multiplets.

With decreasing volume, we saw the development of a quasiparticle peak in the $4f$ electron spectrum. This quasiparticle physics is associated with an energy gain which cannot be captured by LDA and which gives rise to a correlation energy with a negative curvature (353; 229) at low temperatures (not shown). Hence, it also reflects in the total energy shown in Fig. 22: At high temperatures and for the LDA+DMFT(polarised HF) results, we see a simple $E_{\text{tot}}(V)$ curve with a single minimum, the equilibrium volume. But at lower temperatures, the negative curvature of the correlation energy leads to a side structure. Since all energy contributions except for the correlation energy have a positive curvature, the negative curvature of the correlation energy is largely compensated, and we see a very shallow region at $T = 0.054 \text{ eV}$. Within the numerical error bars, it is difficult to decide whether we already have a nega-

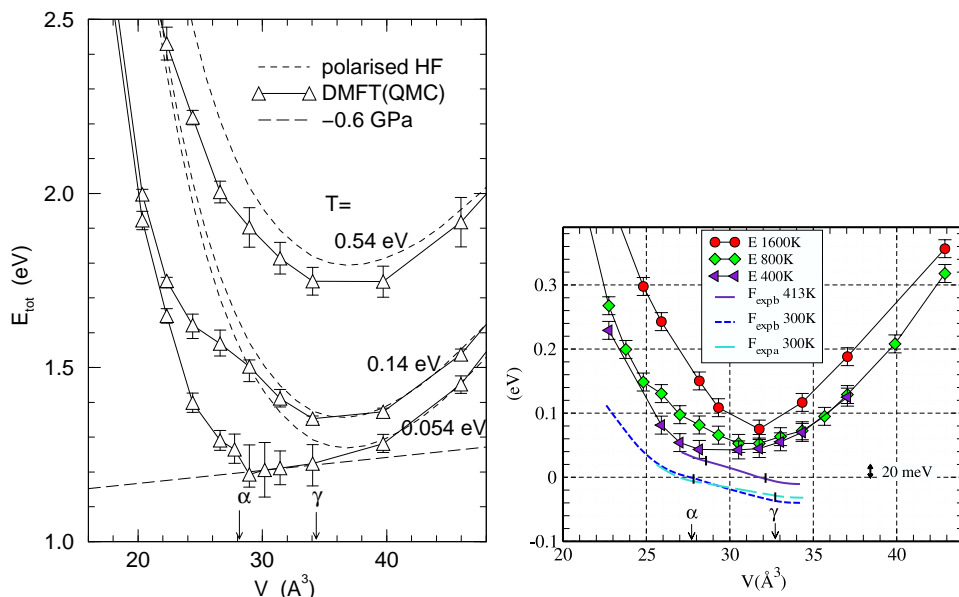


Figure 22. Left: Total LDA+DMFT(QMC) and LDA+DMFT(polarised HF) energy as a function of volume at three temperatures. The negative curvature of the correlation energy results in the development of a side structure, visible as a deviation from the LDA+DMFT(polarised HF) energy.

The long dashed line is the curve which corresponds to the pressure of the α - γ transition: $E = -P_{\text{exp}}V$ (reproduced from (229)). Right: Results for the total energy from (323), including also the experimental free energy. (reproduced from (323)).

tive curvature or whether slightly lower temperatures are needed. A negative curvature of the total energy will give rise to a Maxwell construction and a first order phase transition. The region in which the LDA+DMFT(QMC) results show these tendencies are in agreement with the experimental α - γ transition which is marked by the arrows in Fig. 22. The slope of the shallow minimum is also consistent with an experimental pressure of -0.6 GPa (long-dashed line) given by the α - γ transition pressure extrapolated to $T=0$ (335).

Since vertex corrections do not contribute to the optical conductivity within DMFT (85; 86), the optical conductivity can be calculated directly from the DMFT $\mathbf{G}(\mathbf{k}, \omega)$ and the dipole matrix elements. Haule *et al.* (283) calculated these dipole transition matrix from the LDA wave functions and used the one-crossing approximation (OCA) for solving the auxiliary DMFT impurity model. The resulting optical conductivity in Fig. 23 shows a clear Drude peak for the α phase, while for the γ -phase, the conductivity is much smaller for $\omega \rightarrow 0$ and no Drude peak is discernible. The basic features of the theoretical optical conductivity agree with experiment (lower panel of Fig. 23). Hence, we can altogether conclude that LDA+DMFT correctly describes the thermodynamic and spectral properties of the α - γ transition, as well as the $4f$ occupation of $n_f \approx 1$ in the vicinity of the transition (229).

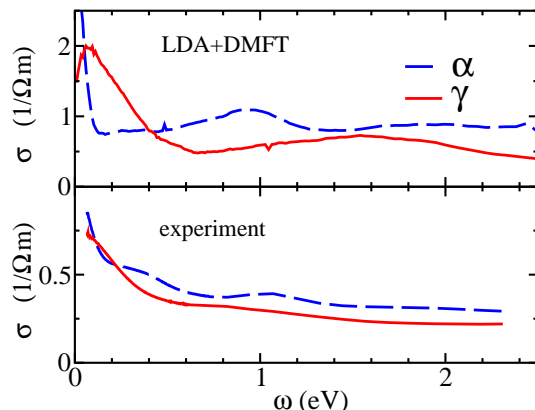


Figure 23. Comparison of LDA+DMFT optical conductivity (top panel; Ref. (283)) with experiment (lower panel; Ref. (328)). The LDA+DMFT spectra are for 580 K (α -Ce) and 1160 K (γ -Ce); the experimental temperature was 5 K (α -Ce) and 300 K (γ -Ce), respectively. (reproduced from Ref. (283)).

6.2 Transition metals

6.2.1 Ferromagnetism in Fe and Ni. Electronic structure calculations for transition metals and transition-metal-transition-metal alloys so far concentrated mainly on the ferromagnets Fe and Ni, starting with early LDA+DMFT calculations by Drchal *et al.* (274; 275) and Lichtenstein *et al.* (158). Since some aspects of ferromagnetism in Fe and Ni, in particular the ferromagnetic moment, are well described by conventional LDA calculations, the question is: Are transition metals strongly correlated as the importance of the 3d orbitals suggest or not? In other words: Is an LDA+DMFT calculation necessary for iron and nickel or is LDA sufficient?

Certainly not described by LDA is the famous -6 eV satellite in Ni. Using LDA+DMFT, Lichtenstein, Katsnelson and Kotliar (158; 36) reinvestigated this element, and did indeed find a satellite at about -6 eV, see Fig. 24 (left panel). This spectral feature could hence be explained by LDA+DMFT as a Hubbard band in the majority-spin spectrum. Later, this finding was also confirmed by GW+DMFT calculations by Biermann, Aryasetiawan and Georges (42; 43; 44), reporting similar results as LDA+DMFT for Ni, see Fig. 24.

Along with the satellite peak, Lichtenstein *et al.* (158; 36) found for the paramagnetic phase a Curie susceptibility which indicates the presence of local (unordered) magnetic moments of size 3.09 and 1.50 μ_B for Fe and Ni, respectively. This Curie susceptibility is in agreement with experiment, see Fig. 25. Along with the satellite, the local moment is clearly a correlation effect, since within L(S)DA the local magnetic moment fades away with the magnetisation. Similarly, LDA+DMFT calculations for α and γ Ce yield local magnetic moments in the paramagnetic phase. The absolute value for the

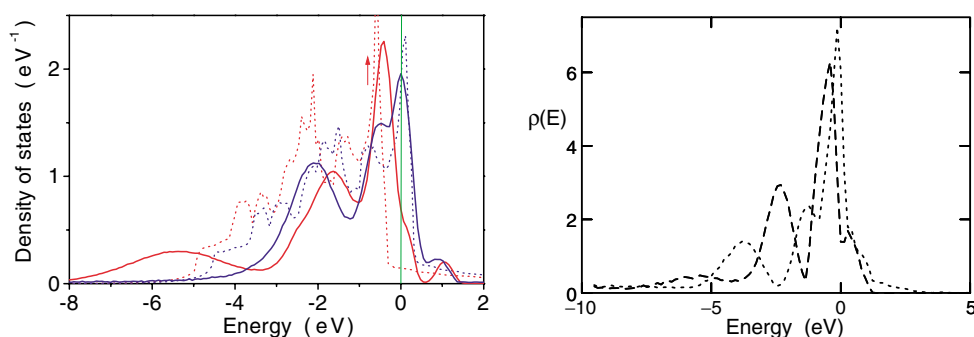


Figure 24. Spectrum (\mathbf{k} -integrated) of Ni [left: LDA+DMFT (solid lines), spinpolarised LDA (LSDA) (dotted lines); right: GW+DMFT]. The two lines represent the minority- and majority-spin spectrum respectively. At roughly -6eV, a satellite peak is clearly visible in the majority-spin spectrum (reproduced from (158) and (42), respectively).

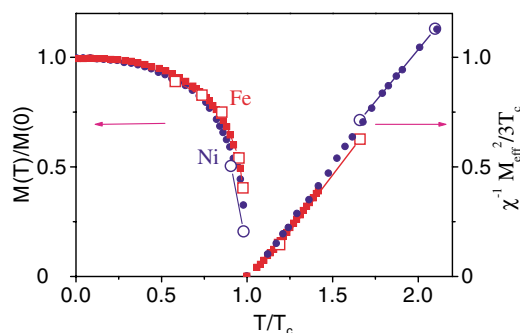


Figure 25. Magnetisation below and magnetic susceptibility above the Curie temperature for iron (squares) and Ni (circles). The LDA+DMFT results (open symbols) are compared to experiment (full symbols) (reproduced from Ref. (158); experiments from Ref. (354; 355)).

Curie temperature is somewhat overestimated, to a lesser extent in Ni (10%) than in Fe (80%). This is (i) because the DMFT neglects non-local correlations such as spin waves and (ii) because the LDA+DMFT calculations employed a Z_2 -symmetric Hund's exchange instead of a $SU(2)$ -symmetric so that transverse spin fluctuations are suppressed. Let us add that the general features of the susceptibility in Fig. 25 have been found for the ferromagnetic transition of a simple model: the single band Hubbard model on a fcc lattice (100).

More recently, Minar *et al.* (356; 357) employed the Korringa-Kohn-Rostoker (KKR) method for LDA+DMFT studies of Fe, Co, Ni and the alloy Fe_xNi_{1-x} , describing -among others- the Fano effect in these ferromagnets, and Grechnev *et al.* (358) studied Fe, Ni and Co surface spectra. Ferromagnetic Ni was also

at the centre of the realistic Gutzwiller calculations by Bünnemann *et al.* (218; 219; 220); for a summary of these results see Ref. (221) and, supplementarily, Ref. (359) for the angular resolved spectrum and Ref. (360) for the total energy. LDA+DMFT calculations for magnetic multilayers of transition metals have been carried out recently by Chioncel *et al.* (273; 361); also note Section 6.4.1 discussing half-metallic ferromagnetism in Heussler alloys.

6.3 Transition metal oxides

Transition metal oxides are an ideal laboratory for the study of electronic correlations in solids, showing a rich spectrum of physical phenomena, ranging from the Mott-Hubbard transition in V_2O_3 , to high temperature superconductivity (among others in Sr_2RuO_4) and the heavy Fermion behaviour in LiV_2O_4 . The materials mentioned and others have been studied meanwhile by LDA+DMFT. In these materials, the $3d$ bands are comparatively narrow with width $W \approx 2 - 3$ eV so that electronic correlations, induced by the local Coulomb interaction $\bar{U} \approx 3 - 5$ eV, are strong. Hence, in Fig. 2, transition metal oxides are neither in the weakly correlated region ($\bar{U}/W \ll 1$) nor is the opposite limit ($\bar{U}/W \gg 1$) appropriate. These materials are in the ‘in-between’ regime, $\bar{U}/W = \mathcal{O}(1)$. If the $3d$ transition metal oxide is metallic this phase is strongly correlated with a *quasiparticle* peak at the Fermi energy and Hubbard side bands. But depending on the material, also Mott insulating behaviour and the Mott-Hubbard metal-insulator transition can occur.

In all LDA+DMFT calculations for transition metal oxides, the LDA+DMFT Hamiltonian (Eq. [34]) was restricted to the low-energy orbitals at the Fermi energy, typically the t_{2g} or e_g orbitals. These Wannier orbitals represent mixtures between mainly the transition metal d and the oxygen p orbitals. So far, LDA+DMFT calculations have not succeeded in taking into account a larger basis including oxygen p orbitals. The naïve inclusion of non-interacting oxygen orbitals result in strong deviation from an integer occupation of the interacting d orbitals. Consequently, electronic correlations are too weak (362). This should be overcome if the p - d and the p - p interactions are included. However, such calculations are computationally very demanding presently. Often, also the simplification for transition metal oxides which we discussed in Section 4.1.5 and which allows us to do the DMFT calculation with the LDA DOS only was employed. For non-cubic systems this is an approximation, which is however very reasonable as long as the crystal is not too strongly distorted from the cubic symmetry. Typically, every transition metal ion is still surrounded by an octahedron of oxygen ions. However, this octahedron is then not perfect anymore, but tilted and distorted. Consequently, there are orbital off-diagonal elements between the e_g and t_{2g} orbitals in the LDA.

In the following, LDA+DMFT calculations for some transition metal oxides will be presented in detail. Besides these studies, LDA+DMFT has been also applied to Cr_2O_3 for which Craco, Laad and Müller-Hartmann (475; 476) analysed orbital correlations and the orbital Kondo effect, $\text{Sr}_2(\text{Ba}_2)\text{VO}_4$ under pressure - a potential d^1 superconductor (477), NiO (32; 478; 479; 481; 480), YTiO_3 (310), TiOCl (482; 483), $\text{Tl}_2\text{Mn}_2\text{O}_7$ (484), MnO, FeO and CoO (481), as well as the Verwey transition in Fe_3O_4 (485).

6.3.1 Ferro-orbital order in LaTiO_3 . LDA+DMFT calculations started with the investigation of $\text{La}_{1-x}\text{Sr}_x\text{TiO}_3$ by Anisimov *et al.* (31), who used the IPT method as a DMFT solver. Subsequently, Zöhl *et al.* (279) repeated these calculations employing LDA+DMFT(NCA), and Nekrasov *et al.* (159) using LDA+DMFT(QMC). The latter authors also compared the application of different DMFT solvers, approximative and numerically exact ones, for a realistic material calculation, i.e. doped LaTiO_3 which is a strongly correlated metal close to a Mott-Hubbard metal-insulator transition. The results showed that the method for solving the DMFT equation matters, as has already been discussed in Section 5.6 with Fig. 19 showing the spectrum of lightly doped LaTiO_3 . Very recently, Craco *et al.* (312) performed new LDA+DMFT(IPT) calculations for LaTiO_3 , including symmetry breaking. Pavarini *et al.* (310) and Craco *et al.* (312; 363) reported a ferro-orbital order. This is of particular interest since it rules out the orbital-liquid picture of Khaliullin *et al.* (364; 365). The LDA+DMFT results hence provided for an important piece of information concerning the controversial debate on the physics of LaTiO_3 .

Recently, also $\text{SrTiO}_3/\text{LaTiO}_3$ heterostructures have been studied by LDA+DMFT and PES (366). Such transition metal oxide heterostructures promise to be a vivid area of research in the future, and LDA+DMFT can provide for the necessary theoretical support.

6.3.2 Mott-Hubbard transition in V_2O_3 . A particularly important system is V_2O_3 which undergoes the famous Mott-Hubbard metal-insulator transition (367; 368), see the phase diagram Fig. 26. Held *et al.* (353; 369) investigated paramagnetic V_2O_3 and Cr-doped V_2O_3 by LDA+DMFT(QMC), describing a Mott transition at a reasonable strength of the Coulomb interaction. The authors reported reasonable agreement with photoemission spectroscopy (PES) experiments by Schramme *et al.* (370), see Fig. 27, as well as with the experimentally expected spin and orbital configuration (371). Later, Mo *et al.* (372; 373) reinvestigated the PES spectrum of V_2O_3 by new bulk-sensitive PES at the Spring-8 synchrotron. Their results represent a big step forward on the experimental side since the V_2O_3 quasiparticle peak could be resolved

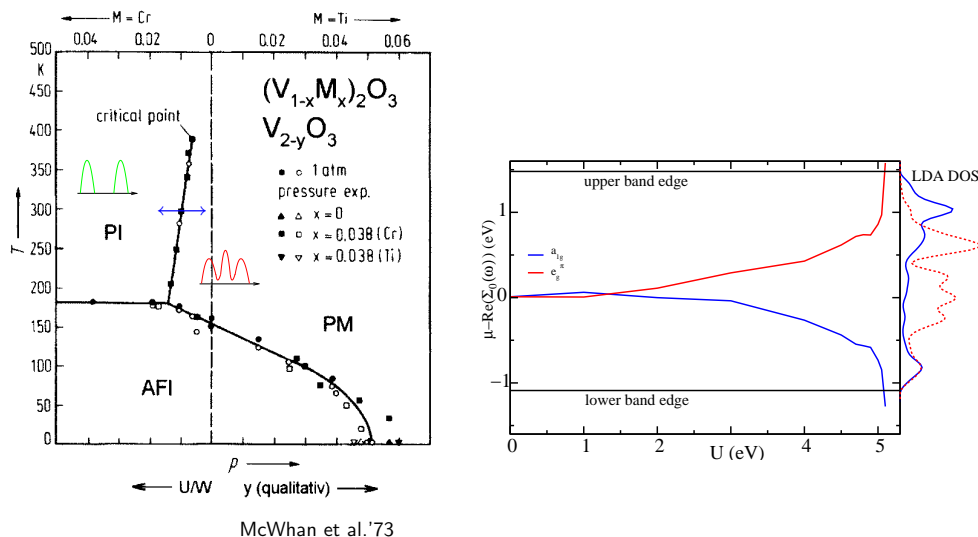


Figure 26. Left: Phase diagram of V_2O_3 as a function of Cr and Ti doping and/or pressure P . Within the paramagnetic phase a Mott-Hubbard transition between metallic (PM) and insulating phase (PI) occurs upon increasing U/W (reproduced from (368)). Right: LDA+DMFT result for the effective chemical potential $\mu - \text{Re}\Sigma(\omega_0)$ for the a_{1g} and e_g orbitals. (reproduced from (369))

for the first time. The PES results are also in better qualitative agreement with LDA+DMFT(QMC), but still show a broader quasiparticle peak with more spectral weight than theoretically expected.

The LDA+DMFT(QMC) results (353; 369) also include important differences to the Mott-Hubbard transition in a one-band Hubbard model. While the latter is characterised by the divergence of the effective mass (or vanishing quasiparticle weight $Z \rightarrow 0$), the effective mass for the a_{1g} band remains finite at the transition in V_2O_3 , only that of the e_g band diverges. This reflects the more complicated nature of the Mott-Hubbard transition in multi-orbital systems. As a detailed analysis by Keller *et al.* (369; 374) revealed, the a_{1g} orbital becomes insulating since the effective chemical potential $\mu - \text{Re}\Sigma(\omega_0)$ moves out of the band edges of the non-interacting DOS, see Fig. 26 (right panel). Hence close to the Fermi energy, the a_{1g} band behaves as if it becomes band-insulating at the transition. Shifts of the a_{1g} effective chemical potential were also reported for $BaVS_3$ (375), albeit not leading to insulating a_{1g} bands in the paramagnetic phase. For $BaVS_3$, these shifts and corresponding changes of the orbital occupation explain the nature of the charge density wave.

Another important LDA+DMFT prediction was that the Mott gap is filled with spectral weight upon increasing temperature. This characteristic feature has been confirmed recently in PES experiments by Mo *et al.* (377). It also re-

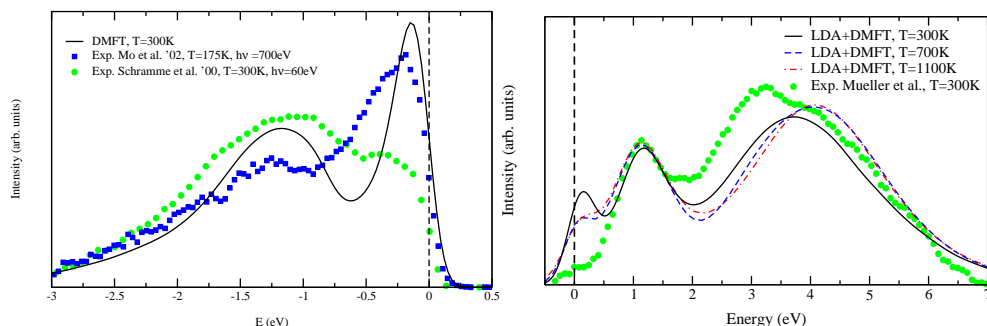


Figure 27. Comparison of the LDA+DMFT(QMC) spectra with photoemission (left; (370; 372)) and X-ray absorption (right; (376)). The photoemission experiments are for two different photon energies (reproduced from (369)).

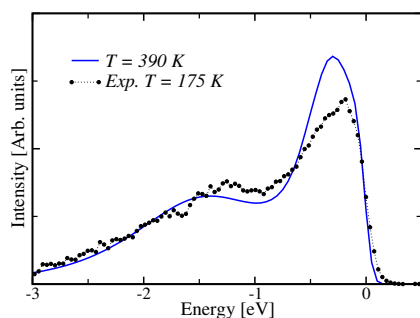


Figure 28. Same comparison as on the left hand side of Fig. 27, but using the NMTO t_{2g} Hamiltonian instead of the LDA DOS and slightly different Coulomb interaction parameters (reproduced from (382)).

flects in the dc conductivity which was reinvestigated by Limelette *et al.* (378) who found critical exponents which agree with those of the DMFT Mott transition scenario (379). Laad *et al.* (380; 381) also studied the Mott-Hubbard transition in V_2O_3 , using LDA+DMFT(IPT) and arriving at the conclusion that the Mott-Hubbard transition is driven by changes of the trigonal distortion under pressure. Using the NMTO-downfolded Hamiltonian instead the simplification to the LDA DOS employed in the earlier studies (353; 369; 380; 381), Poteryaev *et al.* (382) recently recalculated the LDA+DMFT spectrum and reported somewhat better agreement with experiment (377; 383), see Fig. 28.

In model calculations corrections due to non-local correlations have been discussed (384; 138). In particular close to the antiferromagnetic phase transition, paramagnon-like excitations result in strong non-local correlations (138).

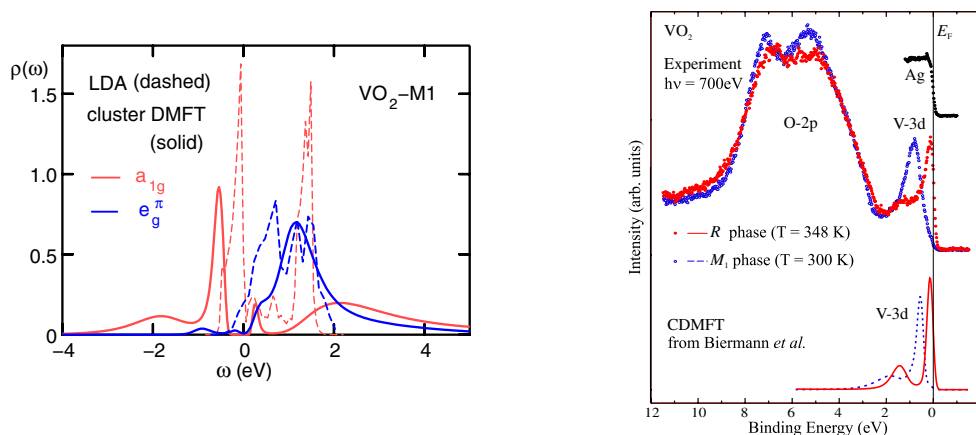


Figure 29. Left: Comparison of single-site and two-site LDA+DMFT spectra for VO_2 for the (insulating) monoclinic crystal structure. (reproduced from (122)). Right: Comparison of these LDA+cluster DMFT spectra with photoemission experiments for the rutile (R) and monoclinic (M_1) phase (reproduced from (389)).

Besides, non-local correlations, also the electron-phonon coupling is expected to be of relevance close to the Mott-Hubbard transition (385; 386). The strong changes of the electronic degrees of freedom couple to the lattice. Hence, while the local electronic correlations described by LDA+DMFT are the driving force for the transition, we have to expect corrections to the present LDA+DMFT results in the immediate vicinity of the Mott-Hubbard transition and close to the onset of magnetic order.

6.3.3 Peierls transition in VO_2 . There is a metal-insulator transition in another vanadate: VO_2 whose high-temperature rutile phase is metallic while the low-temperature monoclinic phase is insulating. One can make use of this effect in “smart” windows, which become reflective (metallic) if bright sunlight heats them up.

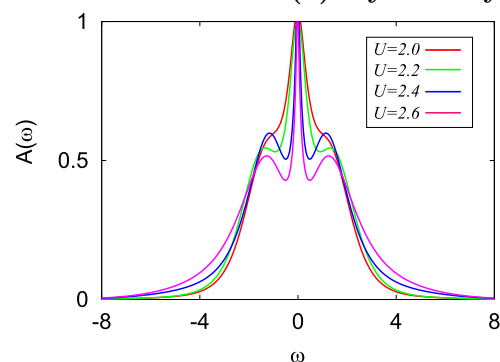
Already within LDA (387), the monoclinic phase is almost gapped due to the dimerisation of V atoms. Using single-site LDA+DMFT, VO_2 has been studied by Laad *et al.* (388) and by Liebsch *et al.* A more realistic scenario for the insulating nature of VO_2 has been proposed however by Biermann *et al.* (122), using a two site cluster DMFT. These two sites form a spin singlet, triggering the insulating behaviour (122). Hence, the gap in VO_2 shown in Fig. 29, is not a Mott-Hubbard gap but a Peierls gap.

6.3.4 Orbital selective Mott-Hubbard transition in $\text{Ca}_{2-x}\text{Sr}_x\text{RuO}_4$.

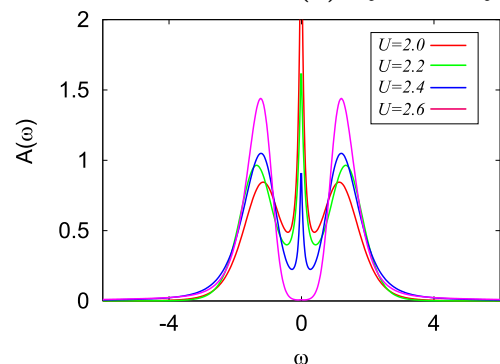
Among the first materials studied by LDA+DMFT was $\text{Ca}_{2-x}\text{Sr}_x\text{RuO}_4$ an unconventional superconductor. The LDA+DMFT calculations by Liebsch and Lichtenstein (390) and by Anisimov *et al.* (391; 392) are very different concerning the size of the Coulomb interaction of the 4d Ru orbitals, i.e. $\bar{U} = 0.8\text{ eV}$, $J = 0.2\text{ eV}$ in (390) and $\bar{U} = 1.7\text{ eV}$, $J = 0.7\text{ eV}$ in (392). Both groups did not address the superconducting phase, and restricted themselves to the normal phase. Actually, the study of superconducting transition metal oxides by DMFT is very difficult, since low temperatures are required. Furthermore, non-s-wave superconductivity is only possible with more formidable cluster DMFT calculations, which for the one-band Hubbard model indeed show d-wave superconductivity, see Ref. (128) and Ref. (117). These one-band calculations have some relevance for the cuprates but will not be discussed here as they are rather model than material calculations. Moreover these calculations have already been reviewed in Ref. (115). Coming back to Sr_2RuO_4 , Liebsch and Lichtenstein (390) reproduced the experimental \mathbf{k} -resolved spectrum very well, including the Hubbard side structure and the Fermi surface. Anisimov *et al.* (391) reported that the Mott-Hubbard transition in $\text{Ca}_{2-x}\text{Sr}_x\text{RuO}_4$ occurs subsequently for different orbitals so that there is a region where some orbitals are insulating and others are metallic, coining the name orbital-selective Mott transition. This orbital-selective Mott transition arises due to different widths of the non-interacting bandwidth of the two-different types of t_{2g} bands and has been a subject of intensive model studies thereafter (393; 394; 395; 396; 397; 398; 399; 400; 401; 402; 403; 404; 405; 406; 407; 408; 409; 410), leading to, at first glance, puzzling discrepancies. These discrepancies were settled when it was realised that the Mott-Hubbard transition is very different for a system with Z_2 symmetric Hund's exchange (393; 394; 396; 404; 405; 406; 409) and $\text{SU}(2)$ symmetric Hund's exchange (395; 397; 398; 399; 400; 401; 402; 403; 350; 411; 412). In the former case the Kondo-like quasiparticle peak cannot occur in the immediate vicinity of the Mott-Hubbard transition since the Z_2 symmetric Hund's exchange forms a $S_z = \pm 1$ spin and a spin-flip from $S_z = +1$ to $S_z = -1$ is not possible. Consequently there is a dip in the spectral function for both the narrow and wide band, see Fig. 30. Sakai *et al.* (292) reinvestigated Sr_2RuO_4 using a $\text{SU}(2)$ symmetric Hund's coupling. But, for the rather small Coulomb interaction of (390) (for which both bands have pronounced quasiparticle peaks) Sakai *et al.* did not yet find pronounced differences between $\text{SU}(2)$ and Z_2 Hund's exchange.

6.3.5 'Kinks' in SrVO_3 . Among transition metal oxides, SrVO_3 is particularly simple because it has (i) a $3d^1$ electronic configuration and (ii) a perfectly

Wide band – SU(2) symmetry



Narrow band – SU(2) symmetry



Z₂ symmetry

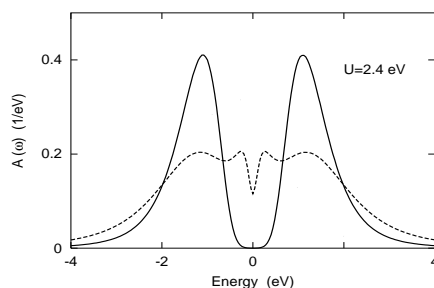


Figure 30. Orbital selective Mott-Hubbard transition for a two band model system with bandwidths 4 and 2 (a.u.) for the two bands respectively. The left side shows the situation for SU(2) symmetric Hund's exchange. At $U=2.6$ (a.u.), the wide band (upper left panel) whereas the narrow band (lower left panel) is already insulating (reproduced from (403)). this is in contrast to the right side, showing the Z_2 symmetric situation. Here, the intermediate phase has a gap for the narrow band (full line) and a dip in the spectrum at the Fermi energy for the wide band (dashed line) (reproduced from (396)).

cubic perovskite lattice structure, see Fig. 31. Due to (i), the effect of Hund's exchange interaction on the ground state properties is less crucial since this exchange interaction only takes effect for two or more electrons. The cubic symmetry (ii) on the other hand results in three degenerate t_{2g} bands at the Fermi energy and allows for the simplification described in Section 4.1.5, i.e. using the DOS instead of the full LDA bandstructure. Hence, SrVO_3 can be considered as a transition metal oxide prototype. Despite this simplicity, there has been some debate concerning the series $\text{Ca}_x\text{Sr}_{1-x}\text{VO}_3$ in which Ca doping x leaves the $3d^1$ configuration unchanged but results in an orthorhombic distortion. Interest in this $3d^1$ series was initiated by Fujimori *et al.* (413) who reported a pronounced lower Hubbard band in PES. While thermodynamic properties such as the Sommerfeld coefficient, resistivity and paramagnetic

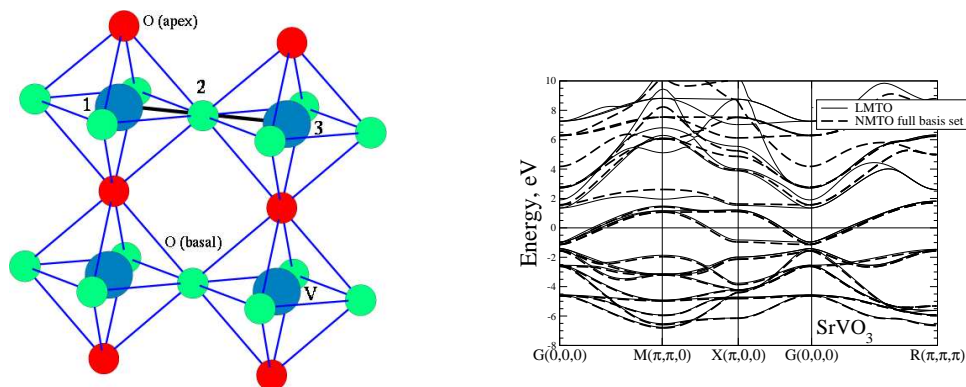


Figure 31. Left: cubic perovskite crystal structure of SrVO_3 ; right: LDA bandstructure calculated using LMTO and NMTO (reproduced from (419; 420))

susceptibility were reported to be essentially independent of x (414; 415; 416), PES (413) and Bremsstrahlungs isochromat spectra (BIS) (417) suggested dramatic differences between CaVO_3 and SrVO_3 , leading to the suggestion of a Mott-Hubbard transition with increasing Ca doping x (418).

This puzzling discrepancy was settled through bulk-sensitive (high photon energy) PES by Maiti *et al.* (421) and by Sekiyama *et al.* (422; 155) which, in mutual agreement with LDA+DMFT calculations (423; 155; 310; 419; 420), showed similar spectra for CaVO_3 and SrVO_3 . Hence the earlier reported differences were attributed to the surface-sensitivity of low photon energy PES. This is also supported by LDA+DMFT calculations of Liebsch *et al.* (424; 425) which show pronounced differences between SrVO_3 surface and bulk spectra. Fig. 31 shows the LDA bandstructure, and Fig. 32 the calculated LDA+DMFT(QMC) spectra in comparison with experiment. Note that the LDA+DMFT spectra are parameter free since the inter-orbital Coulomb interaction $\bar{U} = 3.55$ eV and Hund's exchange $J = 1.0$ eV have been obtained through constrained LDA calculations (423; 155). Pavarini *et al.* (310) also systematically studied the similar d^1 systems LaTiO_3 and YTiO_3 which have an increasingly smaller LDA bandwidth so that these materials become indeed Mott-Hubbard insulators, see Fig. 33.

Despite SrVO_3 being a simple material, the LDA+DMFT(QMC) results led nonetheless to a surprise: The dispersion of the quasiparticle peak shows 'kinks' at -0.25 eV and (less pronounced) at 0.25 eV. This was unexpected since such 'kinks' are usually associated with phonon modes, particularly for high temperature superconductors (426), or the coupling to other bosonic degrees of freedom such as spin fluctuations. The LDA+DMFT calculations showed that such 'kinks' emerge naturally in strongly correlated systems with narrow quasiparticle peaks. Let us note that kinks have also been observed experimentally for SrVO_3 by Yoshida *et al.* in angular-resolved PES (427).

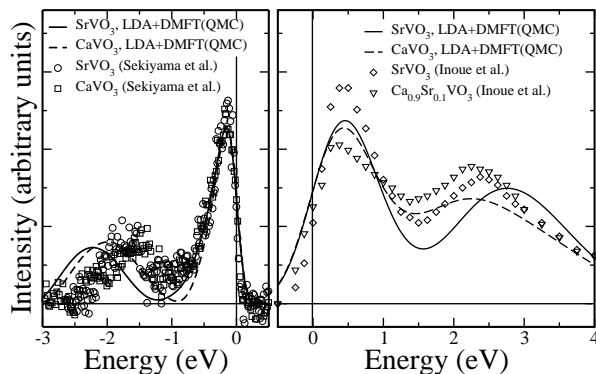


Figure 32. Parameter-free LDA+DMFT(QMC) spectra for SrVO₃ and CaVO₃ compared to PES and XAS experiments below and above the Fermi energy respectively (reproduced from (419)).

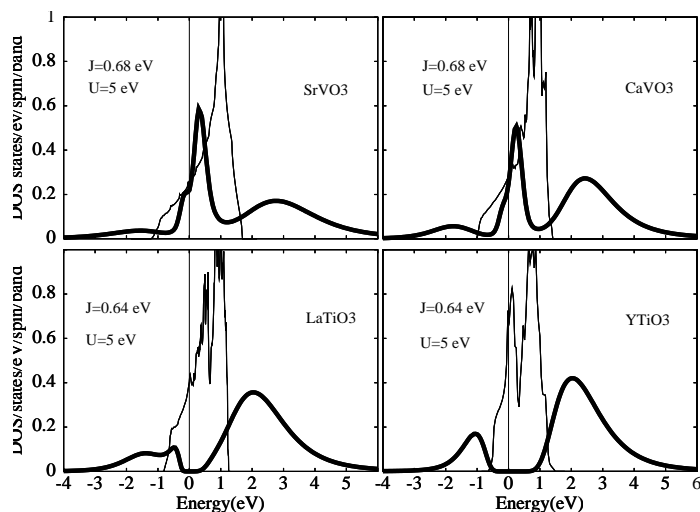


Figure 33. LDA+DMFT(QMC) spectra (thick lines) obtained by Ref. (310) for the 3d¹ series SrVO₃, CaVO₃, LaTiO₃ and YTiO₃. The thin lines represent the corresponding LDA DOSes (reproduced from Ref. (310)).

Using the DMFT self-consistency equation, Byczuk *et al.* (428) were able to show mathematically how a central peak in the spectrum necessarily results in a wiggle in the self energy and, hence, a ‘kink’ in the dispersion relation. Landau’s Fermi liquid theory is restricted to the excitations between Fermi energy and ‘kink’. The rest of the central peak is strongly damped and follows another effective mass renormalisation. That is,

$$E_{\mathbf{k}} = Z_{\text{FL}} \epsilon_{\mathbf{k}} \quad \text{for } |E_{\mathbf{k}}| < \omega_* \quad (152)$$

$$E_{\mathbf{k}} = Z_{\text{CP}} \epsilon_{\mathbf{k}} \pm c \quad \text{for } |E_{\mathbf{k}}| > \omega_*, \quad (153)$$

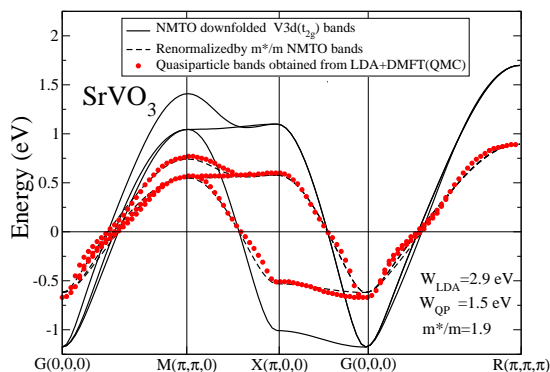


Figure 34. Comparison of the LDA bandstructure for SrVO_3 (full lines) with that from LDA+DMFT(QMC) (dots). Basically, the LDA+DMFT(QMC) describes renormalised quasiparticle bands with weight $Z^{-1} = 1.9$. However, there are deviations in the form of ‘kinks’ at ± 0.25 eV (the Fermi energy is set to zero; reproduced from Ref. (420))

where ω_* is the “kink” energy, $E_{\mathbf{k}}$ the dispersion relation of the interacting system, Z_{FL} the Fermi liquid renormalisation factor, Z_{CP} the renormalisation factor for the dispersion beyond the Fermi-liquid regime, c is a constant. From the bare (LDA) dispersion and one of the renormalisation factors Z_{FL} , Z_{CP} and ω_* , the other two can be calculated in a simple way (428). This allows for example to calculate from the linear specific heat coefficient ($\sim 1/Z_{\text{FL}}$) the ‘position of the “kink” and the overall bandwidth in angular resolved PES.

6.3.6 e'_g hole pockets in Na_xCO_2 . Unconventional superconductivity was also discovered in hydrated Na_xCO_2 (429), resulting in substantial interest in this material. This material is difficult to characterise, particularly, the O-Co-O angle is affected by the hybridisation and not known. Presently, it is also unclear which orbitals are responsible for the superconductivity, and even from which orbitals the Fermi surface is composed of. In LDA (430; 431; 432; 433; 434; 435) both a_{1g} and e'_g orbitals have similar centres of gravity, leading to the possibility of so-called hole pockets in the e'_g bands. Also the a_{1g} bands seem to play an important role, at least these orbitals change most dramatically in LDA when going from normal-conducting mono-layer-hydrated cobaltate to superconducting bi-layer-hydrated cobaltate (434). Since these t_{2g} bands are very narrow, Coulomb correlations are expected to play a major role. Within LDA+U, Zhang *et al.* (436; 435) reported the disappearance of the e'_g hole pockets. In contrast, more accurate LDA+DMFT calculations by Ishida, Perroni and Liebsch (437; 438) predict the contrary, i.e. an enhancement of these pockets. These results have been challenged recently by Marianetti *et al.* (440), reporting the opposite behavior, i.e., the suppression of the e'_g hole pockets in LDA+DMFT. This would agree with

experiments where these pockets seem to be absent. Such conflicting results are possible since, in the case of cobaltates, the results are very sensitive to small changes of the LDA crystal-field splitting, see Ref. (435) for a discussion. Finally, let us also mention two DMFT model studies, concentrating on bad metallic behaviour (439) and the Na-induced potential (441), respectively.

6.3.7 Heavy-Fermion behaviour in LiV_2O_4 . Another interesting transition metal oxide is LiV_2O_4 , the first d system signalling heavy Fermion behaviour by, for example, an unusually large specific heat coefficient, one order of magnitude larger than in other transition metal oxides. Nekrasov *et al.* (442) did realistic LDA+DMFT calculations for LiV_2O_4 and investigated whether the scenario of Anisimov *et al.* (443) for the heavy Fermion behaviour holds. The basic idea of Ref. (443) is a separation of the partially filled t_{2g} electrons into localised ones forming local moments and delocalised ones producing a partially filled metallic band. Then, the hybridisation between those two subsets of electrons, as in f -electron materials, can give rise to heavy Fermion effects. Nekrasov *et al.* (442) found a strong competition between antiferromagnetic direct (the exchange constant corresponds to an energy $\approx -450 k_B \text{ K}$) and ferromagnetic double exchange ($\approx 1090 k_B \text{ K}$). With these estimates it appears to be reasonable that these two contributions almost cancel so that the Kondo exchange ($\approx -630 k_B \text{ K}$) prevails, resulting in heavy Fermion Kondo physics. But, since the energy differences are rather small and the calculations were performed at relatively high temperatures and with a numerical error, the results of (442) do not allow for a final conclusion. In their LDA+DMFT(IPT) calculations, Laad *et al.* (444) on the other hand stressed the importance of geometrical frustration for the heavy Fermion behaviour which forms the basis of another explanations of the unusual behaviour in LiV_2O_4 (445; 446; 447; 448; 449; 450; 451; 452).

More recently, Arita *et al.* (453) managed to investigate the low temperature behavior of LiVO_3 using PQMC as an impurity solver. These calculations indeed show a sharp peak above the Fermi energy, in agreement with experiments (454), see Fig. 35. The physical origin of this sharp peak is however very different from the aforementioned scenarios. The sharp peak emerges from the physics of the a_{1g} orbital, which is a lightly doped Mott-Hubbard insulator, i.e., a metal with a large mass renormalisation.

6.3.8 Colossal magnetoresistance in manganites. Because of the colossal magnetoresistance (CMR) (455; 456), manganites such as $\text{La}_{1-x}\text{Ca}_x\text{MnO}_3$ have been at the focus of research during the last years, including many DMFT studies (74; 58; 110; 111; 457; 458; 75; 459; 460; 112; 461; 462; 463; 464).

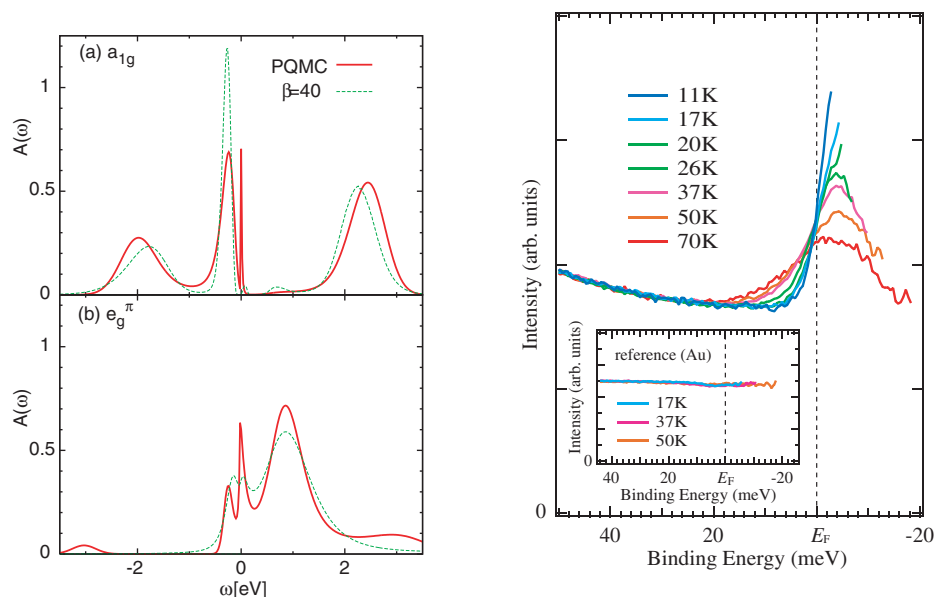


Figure 35. Left: Spectral function of LiVO_3 as calculated by LDA+DMFT for the a_{1g} and the two e_g orbitals at zero temperature (PQMC) and $T = 1/\beta = 1/40$ eV (reproduced from (453)). Right: Corresponding experimental PES spectrum in the vicinity of the Fermi energy (reproduced from (454)).

In the parent compound ($x = 0$), Mn has a d^4 configuration with cubic symmetry so that 3 electrons occupy the lower-lying t_{2g} orbitals, forming a spin 3/2. This spin and its coupling to the remaining itinerant electron in the doubly degenerate e_g bands constitute the (ferromagnetic) Kondo lattice model, which gives rise to ferromagnetism due to the so-called double exchange mechanism: A ferromagnetic alignment of the t_{2g} spins is favorable since it maximises the kinetic energy of the e_g electrons. This model was solved exactly within DMFT by Furukawa (74; 75). Also employing DMFT, Millis and coworkers (58; 110; 111) pointed out however that the double exchange of the Kondo lattice model is not enough for describing manganites and the CMR in particular. The importance of the electron-phonon coupling to Jahn-Teller phonons was stressed, and the Kondo lattice model plus Jahn-Teller phonons was studied using DMFT (110; 111; 458; 112). This model gives large magnetoresistances, however only without Ca doping x and also fails to describe other experimental aspects. Held and Vollhardt (459) on the other hand stressed the importance of electronic correlations induced by the Coulomb interaction between the e_g electrons. The arising question, whether the electron-phonon coupling or the Coulomb interaction is responsible for the insulating nature of the parent compound, was settled recently by LDA+DMFT calculations with

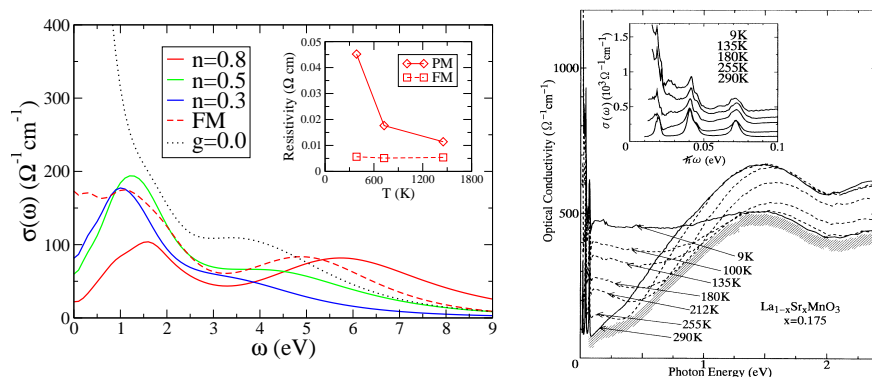


Figure 36. Optical conductivity $\sigma(\omega)$. Left: theory (reproduced from (464)), right: experiment (reproduced from (470)) for the paramagnetic (PM) phase of $\text{La}_{1-x}\text{Sr}_x\text{MnO}_3$, ($n = 1 - x$ electrons/site in the e_g orbitals). The dotted line is without electron-phonon coupling, showing a metallic Drude peak; the dashed line is the optical conductivity for the ferromagnetic phase (FM) at $x = 0.2$. Inset: The PM resistivity strongly increases with decreasing T , resulting in a ‘colossal’ magnetoresistance when going from the PM to the FM phase.

a static Jahn-Teller distortion (463), showing that both Jahn-Teller distortion and Coulomb interaction are needed: The Jahn-Teller distortion gives rise to a crystal field splitting of the two e_g orbitals which is largely enhanced by the Coulomb interaction so that a gap emerges. Since the e_g electrons are also spin-aligned to the t_{2g} spin, LaMnO_3 has one spin-polarised e_g electron per site and is hence an insulator, albeit not a Mott-Hubbard insulator. With the crystal-field splitting being reduced under pressure, Yamasaki *et al.* (463) were also able to explain the pressure-induced insulator-to-metal transition found experimentally by Loa *et al.* (465). Yang and Held (464) subsequently studied doped manganites with dynamical Jahn-Teller phonons instead of a static distortion. The authors reported the trapping of e_g electrons as Jahn-Teller polarons, an effect already described earlier without e_g - e_g Coulomb interaction (110; 111; 458; 112). However, the electronic correlations strongly enhance the tendencies towards polaron formation. The trapping of e_g electrons as polarons results in an insulating-like paramagnetic phase with a pseudogap structure in the spectrum at the Fermi energy, irrespectively of doping x , in agreement with experiment (466; 467; 468; 469). Including the effects of electronic correlations, also the optical conductivity (470; 471; 472; 473; 474) could be described, see Fig. 36, and a large CMR were reported for the doped system, see the inset of Fig. 36.

6.4 Other Materials

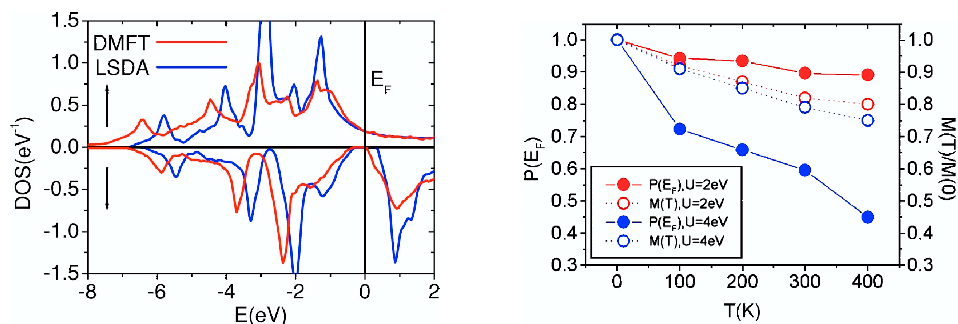


Figure 37. Left: Density of states for NiMnSb for spin-up (upper panel) and down (lower panel).

Due to electronic correlations, nonquasiparticle states appear within the LSDA gap when using DMFT. Right: Spin-polarisation P and magnetization M as a function of temperature for FeMnSb. The nonquasiparticle states lead to a reduction of the spin polarisation (reproduced from (491) and (493), respectively).

6.4.1 Half-metallic ferromagnetism in Heussler alloys. For the technical realization of spintronic (486; 487) devices, materials with high spin-polarisation are necessary. A promising candidate are half-metallic ferromagnets which show metallic behavior for one-spin species and insulating behavior for the other one, allowing in principle for a fully spin-polarized current. Such materials have been intensively studied by LDA. However, many of the potential candidates have d electrons so that electronic correlations cannot be neglected. An example of such correlation effects are nonquasiparticle states in the minority spin-band above the Fermi energy (488; 489; 490). This effect was also studied in realistic LDA+DMFT calculations for the Heussler alloys NiMnSb (491; 492) and FeMnSb (493), see Fig. 37. Due to these nonquasiparticle states, the polarisation is reduced at finite temperatures if electronic correlations are strong, see left part of Fig. 37. Since the emerging non-Fermi-liquid physics is related to magnons, which can only be described very rudimentary by the local DMFT, the inclusion of non-local correlations is necessary for a more accurate description. The nonquasiparticle states lead to a reduced polarisation which is a severe disadvantage for spintronic sources which optimally would be fully polarised. Other candidates for half-metallic ferromagnetism which have been studied by LDA+DMFT are $\text{Ga}_{1-x}\text{Mn}_x\text{As}$ (494; 495), VAs (496), CrAs (497) and CrO_2 (498; 499).

6.4.2 Superconductivity in A_xC_{60} . Synthesized fullerenes display a variety of unusual properties, including superconductivity up to relatively high temperatures, e.g. 33K for $\text{Cs}_x\text{Rb}_y\text{C}_{60}$ (500). Such superconducting alkali-doped

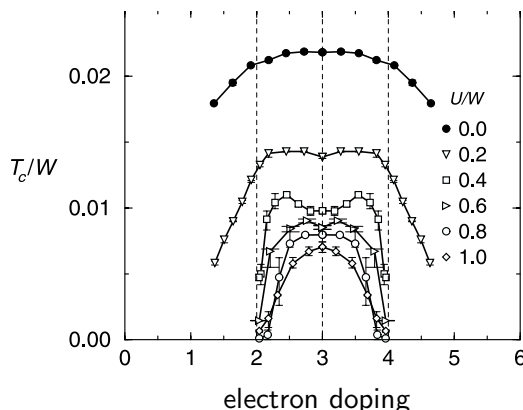


Figure 38. T_c as a function of electron doping in C_{60} fullerenes for different values of the ratio Coulomb interaction over band-width U/W (phonon frequency $\omega_{ph} = 0.24W$; electron-phonon coupling strength $\lambda = 0.6$ (reproduced from (114))).

fullerenes A_xC_{60} are molecular solids with a low bandwidth so that both the phonon frequencies and the Coulomb interaction are comparable to the bandwidth, and the dimensionless electron-phonon coupling is of order 1. Hence, it is important to treat the electron-phonon coupling and the Coulomb interaction on an equal footing which is possible through DMFT. Such realistic DMFT calculations have been carried out by Capone *et al.* (113; 501) and by Han *et al.* (114). These authors found that the superconductivity mediated by electron-phonon coupling is surprisingly resistant to the Coulomb interaction. Together with the strong electron-phonon coupling this hence explains the high superconducting transition temperatures, without the need for a new electronic mechanism for superconductivity. Furthermore, Coulomb interaction and Jahn-Teller coupling tend to localise the electrons at the fillings $n = 2, 4$, which explains why fillings close to $n = 3$ are most favorable for superconductivity, see Fig. 38. This correlation effect is beyond Eliashberg theory and explains the experimentally observed (502) change of T_c with doping.

6.4.3 Mott-insulating zeolites. Zeolites loaded with alkali metals such as $K_nAl_{12}Si_{12}O_{48}$ are at first glance an unlikely candidate for strong electronic correlations. These materials however form ‘superatoms’, see Fig. 39, which act like hydrogen atoms with well defined s and p orbitals. The superatoms in turn crystallise, see central panel of Fig. 39, with a controllable tunneling from superatom to superatom. Since this tunneling is rather weak, these systems then indeed belong to the class of strongly correlated materials, despite the ingredients being K, Al, Si and O atoms. As Arita *et al.* (503) showed by means of LDA and DMFT calculations, $K_nAl_{12}Si_{12}O_{48}$ is Mott-Hubbard insulating even when the nominal doping level (averaged n) is fractional, which explains

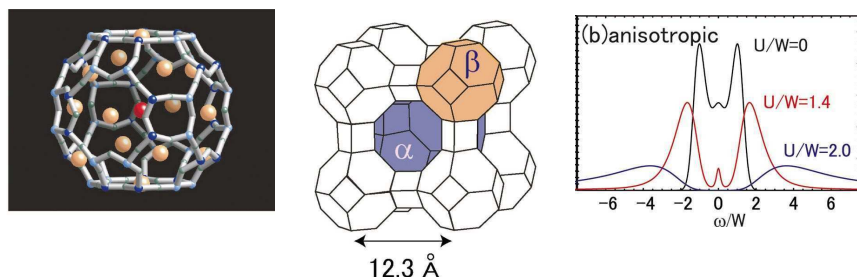


Figure 39. Left: ‘Superatom’ (α cage) of the undoped zeolite (dark blue: Si, light blue: Al, dark green: oxygen, orange and red: K); middle: crystallisation of the cages; right: DMFT spectrum for realistic (anisotropic) hopping parameters showing Mott-insulating behavior for realistic U values. (reproduced from (503))

the experimental fact that K-doped zeolites are insulators (504; 505). Zeolites and fullerenes show that also materials with s and p valence electrons can be strongly correlated because of a reduced hopping. Tehn interesting many-body physics emerges.

7 Summary and outlook

The physics of materials with strong electronic correlations such as transition metal oxides and heavy Fermion systems is characterised by renormalised quasiparticles or Mott-insulating behaviour. Conventional electronic structure calculations, for example, in the LDA or GW approximation, cannot capture this kind of physics and the corresponding energy scales. This became possible by incorporating DMFT into realistic material calculations, merging the strength of LDA (or GW) as an *ab initio* approach with that of DMFT to deal with local electronic correlations between d or f electrons. LDA+DMFT proved to be a breakthrough and is by now a standard approach, albeit standardised program packages are still imperative and self-consistent calculations where the LDA bands are renormalised due to the DMFT correlations are still rare. Also the calculation of physical quantities other than the electronic spectrum, the quantity inherently obtained as the Weiss field in DMFT, is not yet standard. Since in principle all physical quantities can be obtained, there are many opportunities for future work. One should be cautious however that non-local correlations, which are neglected in DMFT, are not particularly important for the physical quantity at hand.

So far, LDA+DMFT has been successfully applied to many materials, with the focus naturally on those with strong electronic correlations. Among others, the volume, the electronic and the phonon spectrum of Pu, the changes of physical properties in Ce through the volume collapse, and the ferromagnetism of Fe and Ni, including the famous 6 eV in Ni, have been calculated. Most work was devoted to transition metal oxides. Here, the Mott-Hubbard metal-insulator transition in V_2O_3 was investigated and the filling of the Mott-Hubbard gap with increasing temperature predicted. The gap in VO_2 was identified as a spin-Peirls gap, and the origin of the colossal magnetoresistance in manganites understood: the paramagnetic phase is insulating-like because of the localisation of electrons as lattice polaron, assisted by strong electronic correlations. Even the, at first glance, simple system $SrVO_3$ was found to show interesting physics, i.e. ‘kinks’. In contrast to the calculations for transition metals and f electron systems, those for transition metal oxides were restricted to the d orbitals crossing the Fermi energy, except for one recent calculation on NiO (480).

A severe drawback of most calculations was that the Coulomb interaction has been used as a free parameter or was chosen ad hoc. This is against the spirit of *ab-initio* calculations which, as a matter of principle, should be parameter-free. Encouraging in this respect are the calculations for the prototypical $4f$ and $3d$ materials Ce and $SrVO_3$ which show that parameter-free LDA+DMFT calculations are possible if the constrained LDA method is employed for determining the Coulomb interaction. In the case of GW+DMFT, the Coulomb interaction is even inherently obtained from GW. Here, the challenge is to do DMFT calculations with a frequency-dependent (screened) interaction.

One should always keep in mind that LDA+DMFT is an approximation for solving the solid state Hamiltonian. The starting point, LDA, is already an approximation even for the extended s and p orbitals. The second approximation involved is the selection of the ‘interacting’ orbitals which by principle is basic dependent. Because of this also the determination of the Coulomb interaction has a considerable uncertainty, less so for well localized $4f$ orbitals but more for $3d$ and particularly $4d$ orbitals. Similarly, the underlying spectral density functional theory is basis dependent, in very contrast to standard density functional theory. Thirdly, DMFT is a many-body approximation for dealing with strongly correlated electron systems. It neglects non-local correlations. Moreover, the solution of the DMFT impurity problem involves possibly a fourth approximation if for example the non-crossing or iterated perturbation theory is employed. While numerically exact quantum Monte Carlo (QMC) simulations are also possible, they are restricted to temperatures at or above (roughly) room temperature since they become too expensive in terms of CPU time at lower temperatures. In this respect density matrix renormalization group cal-

culations, continuous-time and projective quantum Monte Carlo simulations are promising alternatives for zero (or low) temperature.

A major challenge for the future will be to go beyond DMFT, i.e. taking into account non-local correlations on top of the local DMFT correlations in electronic structure calculations. In this respect, cluster extensions of DMFT have already been applied intensively to the two-dimensional Hubbard model with a focus on unconventional superconductivity. The numerical effort restricts these cluster extensions to short range correlations within a (relatively small) cluster. Realistic multi-band calculations were hitherto even restricted to only two sites. This puts particular importance onto the correlation within this pair of sites and is hence naturally only appropriate for particular systems such as VO_2 where such pair correlations dominate. Many important phenomena in correlated electron systems on the other hand stem from long range correlations, e.g. magnons, the interplay between antiferromagnetic fluctuations and unconventional superconductivity, quantum critical points, and critical behavior in general. How these phenomena arise is quite well understood diagrammatically for weak coupling, which as a matter of course is not the proper starting point for strongly correlated electrons. But if we replace the bare Coulomb interaction of the weak coupling perturbation theory by the local (fully irreducible) vertex, we generate a set of diagrams which includes both the local DMFT diagrams and the dominant diagrams for long-range correlations. This is the very idea of the dynamical vertex approximation which has been introduced most recently along with alternative approaches. Another long term goal for electronic structure calculations with DMFT is the calculation of the ionic positions hitherto taken from experiment, the inclusion of lattice dynamics, and eventually molecular dynamics on the basis of LDA+DMFT.

Continuing the fruitful cooperation between bandstructure and many-body physicists, we can optimistically face these challenges in the future. Electronic structure calculations employing DMFT or its diagrammatic and cluster extensions will be a prospering area of research. In particular, such approaches will further improve our understanding of systems with strongly correlated electrons. The advances in electronic structure calculations through DMFT put our ability to predict physical quantities of such strongly correlated materials onto a similar level as conventional electronic structure calculations for weakly correlated materials — at last.

Acknowledgments

This review has benefited from discussions with too many people to list. But I would like to take the opportunity to thank my collaborators O. K. Andersen,

V. I. Anisimov, R. Arita, N. Blümer, M. Feldbacher, A. Katanin, G. Keller, M. Kollar, A. K. McMahan,, W. Metzner, I. A. Nekrasov, Th. Pruschke, R. T. Scalettar, A. Toschi, M. Ulmke, D. Vollhardt, A. Yamasaki and Y.-F. Yang. Moreover, I apologise to those whose work could not be discussed in more detail due to restrictions of time and length. Financially, this work was supported by the Deutsche Forschungsgemeinschaft through the Emmy Noether program.

References

- [1] M. Born and R. Oppenheimer, Ann. Phys. (Leibzig) **84** 457 (1927).
- [2] P. Hohenberg and W. Kohn, Phys. Rev. **136** B864 (1964).
- [3] R. O. Jones and O. Gunnarsson, Rev. Mod. Phys. **61** 689 (1989).
- [4] W. A. Harrison, *Electronic structure and the properties of solids* (Dover, New York, 1989).
- [5] R. M. Dreizler and E. K. U. Gross, *Density functional theory* (Springer, Heidelberg, 1990).
- [6] R. M. Martin, *Electronic Structure: Basic Theory and Practical Methods* (Cambridge University Press, 2004).
- [7] T. C. Leung, X. W. Wang and B. N. Harmon, Phys. Rev. B **37** 384 (1988).
- [8] J. Zaanen, O. Jepsen, O. Gunnarsson, A. T. Paxton and O. K. Andersen, Physica C **153** 1636 (1988).
- [9] W. E. Pickett, Rev. Mod. Phys. **61** 433 (1989).
- [10] L. F. Mattheiss, Phys. Rev. B **5** 290 (1972).
- [11] L. F. Mattheiss, Phys. Rev. B **5** 306 (1972).
- [12] N. F. Mott, Proc. Phys. Soc. A **62** 416 (1949).
- [13] N. F. Mott, Rev. Mod. Phys. **40** 677 (1968).
- [14] F. Gebhard, *The Mott metal-insulator transition* (Springer-Verlag, Berlin, 1997).
- [15] J. Hubbard, Proc. Roy. Soc. London A **276** 238 (1963).
- [16] J. P. Perdew and A. Zunger, Phys. Rev. B **23** 5048 (1981).
- [17] A. Svane and O. Gunnarsson, Phys. Rev. Lett **65** 1148 (1990).
- [18] Z. Szotek, W. M. Temmerman and H. Winter, Phys. Rev. B **47** 4029 (1993).
- [19] V. I. Anisimov, J. Zaanen and O. K. Andersen, Phys. Rev. B **44** 943 (1991).
- [20] W. F. Brinkman and T. M. Rice, Phys. Rev. B **2** 4302 (1970).
- [21] L. N. Bulaevskii, E. L. Nagaev and D. L. Khomskii, Sov. Phys. JETP **27** 838 (1968).
- [22] K. J. von Szczepanski, P. Horsch, W. Stephan and M. Ziegler, Phys. Rev. B **41** 2017 (1990).

- [23] G. Martínez and P. Horsch, Phys. Rev. B **44** 317 (1991).
- [24] E. Cappelluti and S. Ciuchi, Phys. Rev. B **66** 165102 (2002).
- [25] G. Sangiovanni, A. Toschi, E. Koch, K. Held, M. Capone, C. Castellani, O. Gunnarsson, S.-K. Mo, J. W. Allen, H.-D. Kim, A. Sekiyama, A. Yamasaki, S. Suga and P. Metcalf, Phys. Rev. B **73** 205121 (2006).
- [26] R. Strack and D. Vollhardt, Phys. Rev. B **46** 13852 (1992).
- [27] W. Metzner and D. Vollhardt, Phys. Rev. Lett. **62** 324 (1989).
- [28] E. Müller-Hartmann, Z. Phys. B **74** 507 (1989).
- [29] A. Georges and G. Kotliar, Phys. Rev. B **45** 6479 (1992).
- [30] M. Jarrell, Phys. Rev. Lett. **69** 168 (1992).
- [31] V. I. Anisimov, A. I. Poteryaev, M. A. Korotin, A. O. Anokhin and G. Kotliar, J. Phys. Cond. Matter **9** 7359 (1997).
- [32] A. I. Lichtenstein and M. I. Katsnelson, Phys. Rev. B **57** 6884 (1998).
- [33] K. Held, I. Nekrasov, N. Blümer, V. Anisimov and D. Vollhardt, Int. J. Mod. Phys. B **15** 2611 (2001).
- [34] K. Held, I. Nekrasov, G. Keller, V. Eyert, N. Blümer, A. McMahan, R. Scalettar, T. Pruschke, V. Anisimov and D. Vollhardt, In *NIC Series 10, "Quantum Simulations of Complex Many-Body Systems: From Theory to Algorithms"*, edited by J. Grotendorst, D. Marx and A. Muramatsu (2002), p. 175, [cond-mat/0112079].
- [35] K. Held, I. A. Nekrasov, G. Keller, V. Eyert, N. Blümer, A. McMahan, R. Scalettar, T. Pruschke, V. I. Anisimov and D. Vollhardt, Psi-k Newsletter **56** 65 (2003), http://psi-k.dl.ac.uk/newsletters/News_56/Highlight_56.pdf [published as phys. stat. sol. (B) **243** 2599 (2006)].
- [36] A. I. Lichtenstein, M. I. Katsnelson and G. Kotliar, In *Electron Correlations and Materials Properties 2*, edited by A. Gonis (Kluwer, New York, 2004).
- [37] G. Kotliar and S. Savrasov, In *New Theoretical Approaches to Strongly Correlated Systems*, edited by A. M. Tsvelik (Kluwer, New York, 2001).
- [38] V. Oudovenko, G. Palsson, K. Haule, S. Y. Savrasov and G. Kotliar (2004), cond-mat/0409527.
- [39] A. Georges, In *Lectures on the Physics of Highly Correlated Electron Systems VIII: Eighth Training Course*, edited by A. Avella and F. Mancini (American Institute of Physics, 2004), volume 717, p. 3.
- [40] G. Kotliar, S. Y. Savrasov, K. Haule, V. S. Oudovenko, O. Parcollet and C. A. Marianetti, Rev. Mod. Phys. **78** 865 (2006).
- [41] L. Hedin, Phys. Rev. A **139** 796 (1965).
- [42] S. Biermann, F. Aryasetiawan and A. Georges, Phys. Rev. Lett. **90** 086402 (2003).
- [43] S. Biermann, F. Aryasetiawan and A. Georges, In *Proceedings of the NATO Advanced Research Workshop on "Physics of Spin in Solids:*

- Materials, Methods, and Applications*" (Kluwer, New York, 2004), cond-mat/0401653.
- [44] F. Aryasetiawan, S. Biermann and A. Georges, In *Proceedings of the conference on "Coincidence Studies of Surfaces, Thin Films and Nanostructures"*, edited by A. Gonis (Wiley, New York, 2004).
 - [45] O. K. Andersen, Phys. Rev. B **12** 3060 (1975).
 - [46] O. K. Andersen, T. Saha-Dasgupta, R. W. Tank, C. Arcangeli, O. Jepsen and G. Krier, In *Lecture notes in Physics*, edited by H. Dreysse (Springer, Berlin, 1999).
 - [47] O. K. Andersen, T. Saha-Dasgupta, S. Ezhov, L. Tsetseris, O. Jepsen, R. W. Tank and C. A. G. Krier, Psi-k Newsletter # **45** 86 (2001), http://psi-k.dl.ac.uk/newsletters/News_45/Highlight_45.pdf.
 - [48] G. H. Wannier, Phys. Rev. **52** 191 (1937).
 - [49] N. Marzari and D. Vanderbilt, Phys. Rev. B **56** 12847 (1997).
 - [50] I. Souza, N. Marzari and D. Vanderbilt, Phys. Rev. B **65** 035109 (2001).
 - [51] W. Ku, H. Rosner, W. E. Pickett and R. T. Scalettar, Phys. Rev. Lett. **89** 167204 (2002).
 - [52] I. Schnell, G. Czycholl and R. C. Albers, Phys. Rev. B **65** 075103 (2002).
 - [53] I. Schnell, G. Czycholl and R. C. Albers, Phys. Rev. B **68** 245102 (2003).
 - [54] V. I. Anisimov, D. E. Kondakov, A. V. Kozhevnikov, I. A. Nekrasov, Z. V. Pchelkina, J. W. Allen, S.-K. Mo, H.-D. Kim, P. Metcalf, S. Suga, A. Sekiyama, G. Keller, I. Leonov, X. Ren and D. Vollhardt, Phys. Rev. B **71** 125119 (2005).
 - [55] F. Lechermann, A. Georges, A. Poteryaev, S. Biermann, M. Posternak, A. Yamasaki and O. K. Andersen, Phys. Rev. B **74** 125120 (2006).
 - [56] A. Georges, G. Kotliar, W. Krauth and M. Rozenberg, Rev. Mod. Phys. **68** 13 (1996).
 - [57] F. Aryasetiawan and O. Gunnarsson, Rep. Prog. Phys. **61** 237 (1998).
 - [58] A. J. Millis, P. B. Littlewood and B. I. Shraiman, Phys. Rev. Lett. **74** 5144 (1995).
 - [59] M. Levy, Proc. Natl. Acad. Sci. (USA) **76** 6062 (1979).
 - [60] W. Kohn and L. J. Sham, Phys. Rev. **140** A1133 (1965).
 - [61] L. Hedin and B. Lundqvist, J. Phys. C: Solid State Phys. **4** 2064 (1971).
 - [62] U. von Barth and L. Hedin, J. Phys. C: Solid State Phys. **5** 1629 (1972).
 - [63] D. M. Ceperley and B. J. Alder, Phys. Rev. Lett. **45** 566 (1980).
 - [64] D. Vanderbilt, Phys. Rev. B **41** 7892 (1990).
 - [65] E. Müller-Hartmann, Int. J. Mod. Phys. B **3** 2169 (1989).
 - [66] E. Müller-Hartmann, Z. Phys. B **76** 211 (1989).
 - [67] L. M. Falicov and J. C. Kimball, Phys. Rev. Lett. **22** 997 (1969).
 - [68] U. Brandt and C. Mielsch, Z. Phys. B **75** 365 (1989).
 - [69] U. Brandt and C. Mielsch, Z. Phys. B **79** 295 (1990).
 - [70] U. Brandt and C. Mielsch, Z. Phys. B **82** 37 (1991).

- [71] P. G. J. van Dongen and D. Vollhardt, Phys. Rev. Lett. **65** 1663 (1990).
- [72] P. G. J. van Dongen, Phys. Rev. B **45** 2267 (1992).
- [73] J. K. Freericks and V. Zlatić, Rev. Mod. Phys. **75** 1333 (2003).
- [74] N. Furukawa, J. Phys. Soc. Jap. **63** 3214 (1994).
- [75] N. Furukawa, In *Physics of Manganites*, edited by T. A. Kaplan and S. D. Mahanti (Kluwer, New York, 1999).
- [76] V. Janiš, Z. Phys. B **83** 227 (1991).
- [77] V. Janiš and D. Vollhardt, Int. J. Mod. Phys. B **6** 731 (1992).
- [78] F. J. Ohkawa, J. Phys. Soc. Jap. **60** 3218 (1991).
- [79] F. J. Ohkawa, Prog. Theor. Phys. Supp. **106** 95 (1991).
- [80] P. W. Anderson, In *Moment formation in solids*, edited by W. J. L. Buyers (Plenum Press, New York, 1984), p. 313.
- [81] A. C. Hewson, *The Kondo Problem to Heavy Fermions* (Cambridge University Press, Cambridge, 1993).
- [82] H. Schweitzer and G. Czycholl, Phys. Rev. Lett. **67** 3724 (1991).
- [83] M. Jarrell and T. Pruschke, Z. Phys. B **90** 187 (1993).
- [84] M. Jarrell and T. Pruschke, Phys. Rev. B **49** 1458 (1993).
- [85] T. Pruschke, D. L. Cox and M. Jarrell, Phys. Rev. B **47** 3553 (1993).
- [86] T. Pruschke, D. L. Cox and M. Jarrell, Europhys. Lett. **21** 593 (1993).
- [87] M. J. Rozenberg, X. Y. Zhang and G. Kotliar, Phys. Rev. Lett. **69** 1236 (1992).
- [88] A. Georges and W. Krauth, Phys. Rev. Lett. **69** 1240 (1992).
- [89] M. Caffarel and W. Krauth, Phys. Rev. Lett. **72** 1545 (1994).
- [90] O. Sakai and Y. Kuramoto, Solid State Commun. **89** 307 (1994).
- [91] R. Bulla, A. C. Hewson and T. Pruschke, J. Phys.: Condens. Matter **10** 8365 (1998).
- [92] G. Kotliar and D. Vollhardt, Physics Today **March** 53 (2004).
- [93] W. Metzner, Phys. Rev. B **43** 8549 (1991).
- [94] A. A. Abrikosov, L. P. Gorkov and I. E. Dzyaloshinski, *Methods of Quantum Field Theory in Statistical Physics* (Dover, New York, 1963).
- [95] W. Negele and H. Orland, *Quantum Many-Particle Systems* (Addison-Wesley, New York, 1987).
- [96] J. C. Slater, Phys. Rev. **82** 538 (1951).
- [97] W. Heisenberg, Z. Phys. **49** 619 (1928).
- [98] K. Held, M. Ulmke and D. Vollhardt, Mod. Phys. Lett. B **10** 203 (1996).
- [99] K. Held, M. Ulmke, N. Blümer and D. Vollhardt, Phys. Rev. B **56** 14469 (1997).
- [100] M. Ulmke, Eur. Phys. J. B **1** 301 (1998).
- [101] J. Wahle, N. Blümer, J. Schlipf, K. Held and D. Vollhardt, Phys. Rev. B **58** 12749 (1998).
- [102] K. Held and D. Vollhardt, Euro. Phys. J. B **5** 473 (1998).
- [103] V. Janiš, M. Ulmke and D. Vollhardt, Europhys. Lett. **24** 287 (1993).

- [104] M. Ulmke, V. Janiš and D. Vollhardt, Phys. Rev. B **51** 10411 (1995).
- [105] V. Dobrosavljević and G. Kotliar, Phys. Rev. Lett. **71** 3218 (1993).
- [106] V. Dobrosavljević and G. Kotliar, Phys. Rev. B **50** 1430 (1994).
- [107] J. K. Freericks, M. Jarrell and D. J. Scalapino, Phys. Rev. B **48** 6302 (1993).
- [108] J. K. Freericks, Phys. Rev. B **50** 403 (1994).
- [109] J. K. Freericks and M. Jarrell, Phys. Rev. B **50** 6939 (1994).
- [110] A. J. Millis, B. I. Shraiman and R. Mueller, Phys. Rev. Lett. **77** 175 (1996).
- [111] A. J. Millis, R. Mueller and B. I. Shraiman, Phys. Rev. B **54** 5405 (1996).
- [112] B. Michaelis and A. J. Millis, Phys. Rev. B **68** 115111 (2003).
- [113] M. Capone, M. Fabrizio, C. Castellani and E. Tosatti, Science **296** 2364 (2002).
- [114] J. E. Han, O. Gunnarsson and V. H. Crespi, Phys. Rev. Lett. **90** 167006 (2003).
- [115] T. Maier, M. Jarrell, T. Pruschke and M. H. Hettler, Rev. Mod. Phys. **77** 1027 (2005).
- [116] G. Kotliar, S. Y. Savrasov, G. Pálsson and G. Biroli, Phys. Rev. Lett. **87** 186401 (2001).
- [117] A. I. Lichtenstein and M. I. Katsnelson, Phys. Rev. B **62** 9283 (R) (2000).
- [118] M. Potthoff, M. Aichhorn and C. Dahnken, Phys. Rev. Lett. **91** 206402 (2003).
- [119] M. Capone, M. Civelli, S. S. Kancharla, C. Castellani and G. Kotliar, Phys. Rev. B **69** 195105 (2004).
- [120] A. I. Poteryaev, A. I. Lichtenstein and G. Kotliar, Phys. Rev. Lett. **93** 086401 (2004).
- [121] V. V. Mazurenko, A. I. Lichtenstein, M. I. Katsnelson, I. Dasgupta, T. Saha-Dasgupta and V. I. Anisimov, Phys. Rev. B **66** 081104 (R) (2002).
- [122] S. Biermann, A. Poteryaev, A. I. Lichtenstein and A. Georges, Phys. Rev. Lett. **94** 026404 (2005).
- [123] M. H. Hettler, A. N. Tahvildar-Zadeh and M. Jarrell, Phys. Rev. B **58** 7475 (R) (1998).
- [124] C. Gros and R. Valenti, Phys. Rev. B **48** 418 (1993).
- [125] M. Potthoff, Eur. Phys. J. B **32** 429 (2003).
- [126] M. Potthoff and M. Balzer (2006), `cond-mat/0610217`.
- [127] R. Kikuchi Phys. Rev. **81** 988 (1951).
- [128] T. Maier, M. Jarrell, T. Pruschke and J. Keller, Phys. Rev. Lett. **85** 1524 (2000).
- [129] M. Capone and G. Kotliar (2006), `cond-mat/0603227`.

- [130] M. Civelli, M. Capone, S. S. Kancharla, O. Parcollet and G. Kotliar, Phys. Rev. Lett. **95** 106402 (2005).
- [131] T. A. Maier, M. Jarrell, T. C. Schulthess, P. R. C. Kent and J. B. White, Phys. Rev. Lett. **95** 237001 (2005).
- [132] R. Arita and K. Held, Phys. Rev. B **73** 064515 (2006).
- [133] K. Aryanpour, M. H. Hettler and M. Jarrell, Phys. Rev. B **67** 085101 (2003).
- [134] J. P. Hague, M. Jarrell and T. C. Schulthess, Phys. Rev. B **69** 165113 (2004).
- [135] N. E. Bickers, D. J. Scalapino and S. R. White, Phys. Rev. Lett. **62** 961 (1989).
- [136] A. Schiller and K. Ingersent, Phys. Rev. Lett. **75** 113 (1995).
- [137] G. Zaránd, D. L. Cox and A. Schiller, Phys. Rev. B **62** 16227 (R) (2000).
- [138] A. Toschi, A. A. Katanin and K. Held (2006), `cond-mat/0603100`.
- [139] H. Kusunose, `cond-mat/0602451` (2006).
- [140] C. Slezak, M. Jarrell, T. Maier and J. Deisz (2006), `cond-mat/0603421`.
- [141] E. Z. Kuchinskii, I. A. Nekrasov and M. V. Sadovskii, Sov. Phys. JETP Lett. **82** 98 (2005).
- [142] M. V. Sadovskii, I. A. Nekrasov, E. Z. Kuchinskii, T. Pruschke and V. I. Anisimov, Phys. Rev. B **72** 155105 (2005).
- [143] E. Z. Kuchinskii, I. A. Nekrasov and M. V. Sadovskii (2006), `cond-mat/0609404`.
- [144] E. Z. Kuchinskii, I. A. Nekrasov and Z. V. P. M. V. Sadovskii (2006), `cond-mat/0606651`.
- [145] T. Saso, J. Phys. Soc. Jap. **68** 3941 (1999).
- [146] C. J. Bolech, D. D. Kancharia and G. Kotliar, Phys. Rev. B **67** 75110 (2003).
- [147] A. N. Rubtsov, M. I. Katsnelson and A. I. Lichtenstein, `cond-mat/0612196`.
- [148] H. Hafermann, S. Brener, A. N. Rubtsov, M. I. Katsnelson and A. I. Lichtenstein, `cond-mat/0707.4022`.
- [149] K. Held, *Untersuchungen korrelierter Elektronensysteme im Rahmen der Dynamischen Molekularfeldtheorie*, Ph.D. thesis, Universität Augsburg (1999).
- [150] S. Y. Savrasov and G. Kotliar (2001), `cond-mat/0106308`.
- [151] P. H. Dederichs, S. Blügel, R. Zeller and H. Akai, Phys. Rev. Lett. **53** 2512 (1984).
- [152] A. K. McMahan, R. M. Martin and S. Satpathy, Phys. Rev. B **38** 6650 (1988).
- [153] O. Gunnarsson, O. K. Andersen, O. Jepsen and J. Zaanen, Phys. Rev. B **39** 1708 (1989).
- [154] K. Held, A. K. McMahan and R. T. Scalettar, Phys. Rev. Lett. **87**

- 276404 (2001).
- [155] A. Sekiyama, H. Fujiwara, S. Imada, S. Suga, H. Eisaki, S. I. Uchida, K. Takegahara, H. Harima, Y. Saitoh, I. A. Nekrasov, G. Keller, D. E. Kondakov, A. V. Kozhevnikov, Th. Pruschke, K. Held, D. Vollhardt and V. I. Anisimov, Phys. Rev. Lett. **93** 156402 (2004).
 - [156] J. C. Slater, *Quantum Theory of Molecules and Solids*, volume 4 (McGraw-Hill, New York, 1974).
 - [157] J. F. Janak, Phys. Rev. B **18** 7165 (1978).
 - [158] A. I. Lichtenstein, M. I. Katsnelson and G. Kotliar, Phys. Rev. Lett. **87** 67205 (2001).
 - [159] I. A. Nekrasov, K. Held, N. Blümer, A. I. Poteryaev, V. I. Anisimov and D. Vollhardt, Eur. Phys. J. B **18** 55 (2000).
 - [160] O. K. Andersen and O. Jepsen, Phys. Rev. Lett. **53** 2571 (1984).
 - [161] I. Solovyev, N. Hamada and K. Terakura, Phys. Rev. B **53** 7158 (1996).
 - [162] J. S. Griffith, *The Theory of transition-metal ions* (Cambridge University Press, Cambridge, 1971).
 - [163] J. Sugar and C. Corliss, J. Phys. Chem. Ref. Data **14** Supplement No. 2 (1985).
 - [164] R. Chitra and G. Kotliar, Phys. Rev. B **62** 12715 (2000).
 - [165] S. Y. Savrasov, G. Kotliar and E. Abrahams, Nature **410** 793 (2001).
 - [166] J. M. Luttinger and J. C. Ward, Phys. Rev. **118** 1417 (1960).
 - [167] G. Baym and L. P. Kadanoff, Phys. Rev. **124** 287 (1961).
 - [168] G. Baym, Phys. Rev. **127** 1391 (1962).
 - [169] V. Janiš, Czech. J. Phys. B **36** 1107 (1986).
 - [170] V. Janiš, Phys. Rev. B **40** 11331 (1989).
 - [171] R. Fukuda, T. Kotani and S. Yokojima, Prog. Theory Phys. **92** 833 (1994).
 - [172] R. Fukuda, M. Komachiya, S. Yokojima, K. Okumura, Y. Suzuki and T. Inagaki, Prog. Theory Phys. Suppl. **121** 1 (1996).
 - [173] D. R. Hartree, Proc. Camb. Phil. Soc. **24** 11, 89 (1928).
 - [174] P. Weiss, J. de Phys. **6** (4) 661 (1907).
 - [175] J. L. Smith and Q. Si, Europhys. Lett. **45** 228 (1996).
 - [176] Q. Si and J. L. Smith, Phys. Rev. Lett. **77** 3391 (1996).
 - [177] R. Chitra and G. Kotliar, Phys. Rev. Lett. **84** 3678 (2000).
 - [178] R. Chitra and G. Kotliar, Phys. Rev. B **63** 115110 (2001).
 - [179] O. Parcollet and A. Georges, Phys. Rev. B **59** 5341 (1999).
 - [180] J. C. Slater, Phys. Rev. **35** 210 (1930).
 - [181] V. Fock, Z. Phys. **61** 126 (1930).
 - [182] M. Stadelé, J. A. Majewski, P. Vogl and A. Gorling, Phys. Rev. Lett. **79** 2089 (1997).
 - [183] F. Aryasetiawan, M. Imada, A. Georges, G. Kotliar, S. Biermann and A. I. Lichtenstein, Phys. Rev. B **70** 195104 (2004).

REFERENCES

111

- [184] P. Sun and G. Kotliar, Phys. Rev. B **66** 85120 (2002).
- [185] P. Sun and G. Kotliar, Phys. Rev. Lett. **92** 196402 (2004).
- [186] H. Kajueter, Ph.D. thesis, Rutgers University (1996).
- [187] J. Hubbard, Proc. Roy. Soc. London A **281** 401 (1964).
- [188] M. Jarrell and J. E. Gubernatis, Physics Reports **269** 133 (1996).
- [189] M. Feldbacher, K. Held and F. F. Assaad, Phys. Rev. Lett. **93** 136405 (2004).
- [190] K. G. Wilson, Rev. Mod. Phys. **47** 773 (1975).
- [191] M. Capone, L. de' Medici and A. Georges, cond-mat/0512484 (2005).
- [192] R. Bulla, Phys. Rev. Lett. **83** 136 (1999).
- [193] R. Bulla, T. A. Costi and D. Vollhardt, Phys. Rev. B **64** 45103 (2001).
- [194] R. Bulla, T. A. Costi and T. Pruschke, cond-mat/0701105 (2007).
- [195] M. Potthoff, Phys. Rev. B **64** 165114 (2001).
- [196] S. R. White, Phys. Rev. Lett. **69** 2863 (1992).
- [197] E. Jeckelmann, Phys. Rev. B **66** 045114 (2002).
- [198] U. Schollwöck, Rev. Mod. Phys. **77** 259 (2005).
- [199] F. Gebhard, E. Jeckelmann, S. Mahler, S. Nishimoto and R. M. Noack, Eur. Phys. J. B **36** 491 (2003).
- [200] C. Raas, G. S. Uhrig and F. B. Anders, Phys. Rev. B **69** 041102 (R) (2004).
- [201] S. Nishimoto, F. Gebhard and E. Jeckelmann, J. Phys.: Condens. Matter **16** 613 (2004).
- [202] D. J. Garcia, K. Hallberg and M. J. Rozenberg, cond-mat/0403169 (2004).
- [203] C. Raas and G. S. Uhrig, Eur. Phys. J. B **45** 293 (2005).
- [204] M. Karski, C. Raas and G. S. Uhrig, Phys. Rev. B **72** 113110 (R) (2005).
- [205] W. Metzner, Z. Phys. B **77** 253 (1989).
- [206] W. Metzner, Z. Phys. B **82** 183 (1991).
- [207] F. Gebhard, Phys. Rev. B **41** 9452 (1990).
- [208] M. C. Gutzwiller, Phys. Rev. Lett. **10** 159 (1963).
- [209] M. C. Gutzwiller, Phys. Rev. **134** A 923 (1964).
- [210] M. C. Gutzwiller, Phys. Rev. **137** A 1726 (1965).
- [211] F. Gebhard, Phys. Rev. B **44** 992 (1991).
- [212] G. Kotliar and A. Ruckenstein, Phys. Rev. Lett. **57** 1362 (1986).
- [213] S. Florens and A. Georges, Phys. Rev. B **66** 165111 (2002).
- [214] L. de' Medici, A. Georges and S. Biermann, cond-mat/0503764 (2005).
- [215] R. Strack and D. Vollhardt, J. Low Temp. Phys. **84** 357 (1991).
- [216] R. Strack and D. Vollhardt, Mod. Phys. Lett. B **5** 1377 (1991).
- [217] Z. Gulácsi, R. Strack and D. Vollhardt, Phys. Rev. B **47** 8594 (1993).
- [218] J. Bünemann and W. Weber, Physica B **230** 412 (1997).
- [219] J. Bünemann, F. Gebhard and W. Weber, J. Phys. Cond. Matter **9** 7343 (1997).

- [220] J. Bünemann, W. Weber and F. Gebhard, Phys. Rev. B **57** 6896 (1998).
- [221] W. Weber, J. Bünemann and F. Gebhard, In *Lecture Notes in Physics*, edited by K. Baberschke, M. Donath and W. Nolting (Springer, Berlin, 2001), volume 580.
- [222] G. Stollhoff and P. Thalmeier, Z. Phys. B **43** 13 (1981).
- [223] A. M. Oleś, Phys. Rev. B **23** 271 (1981).
- [224] A. M. Oleś and G. Stollhoff, Phys. Rev. B **29** 314 (1984).
- [225] V. I. Anisimov, F. Aryasetiawan and A. I. Lichtenstein, J. Phys. Cond. Matter **9** 767 (1997).
- [226] E. C. Stoner, J. de Phys. et Ra. **12** 372 (1951).
- [227] L. Néel, Ann. Phys. (Leibzig) **18** 5 (1932).
- [228] C. Gros, Phys. Rev. B **50** 7295 (1994).
- [229] A. K. McMahan, K. Held and R. T. Scalettar, Phys. Rev. B **67** 75108 (2003).
- [230] M. Cyrot, Phys. Rev. Lett. **25** 871 (1970).
- [231] M. Cyrot, Phil. Mag. **24** 1031 (1972).
- [232] M. Cyrot, Journ. de Physique **33** 125 (1972).
- [233] A. Kawabata, Prog. Theor. Phys. **48** 1793 (1972).
- [234] D. M. Edwards, A. C. M. Green and K. Kubo, J. Phys. Cond. Matter **11** 9107 (1999).
- [235] D. M. Edwards, Adv. Phys. **51** 1259 (2002).
- [236] D. Meyer, C. Santos and W. Nolting, J. Phys. Cond. Matter **13** 2531 (2001).
- [237] A. C. M. Green, Phys. Rev. B **63** 205110 (2001).
- [238] P. Soven, Phys. Rev. **156** 809 (1967).
- [239] D. W. Taylor, Phys. Rev. **156** 1017 (1967).
- [240] B. Velický, S. Kirkpatrick and H. Ehrenreich, Phys. Rev. **175** 747 (1968).
- [241] R. J. Elliot, J. A. Krumhansl and P. L. Leath, Rev. Mod. Phys. **46** 465 (1974).
- [242] B. L. Gyorffy, Phys. Rev. B **2382** 5 (1972).
- [243] J. Kudrnovský, V. Drchal and J. Mašek, Phys. Rev. B **35** 2487 (1987).
- [244] L. Schwartz and E. Siggia, Phys. Rev. B **5** 383 (1972).
- [245] V. Janiš and D. Vollhardt, Z. Phys. B **91** 317 (1993).
- [246] V. Janiš, J. Mašek and D. Vollhardt, Z. Phys. B **91** 325 (1993).
- [247] W. Nolting and A. Oleś, phys. stat. sol. (b) **104** 563 (1981).
- [248] W. Nolting and W. Borigiel, Phys. Rev. B **39** 6962 (1989).
- [249] S. Bei der Kellen, W. Nolting and G. Borstel, Phys. Rev. B **42** 447 (1990).
- [250] M. Potthoff and W. Nolting, J. Phys. Cond. Matter **8** 4937 (1996).
- [251] J. Beenen and D. M. Edwards, Phys. Rev. B **52** 13636 (1995).
- [252] B. Mehlig, H. Eskes, R. Hayn and M. B. J. Meinders, Phys. Rev. B **52** 2463 (1995).

- [253] C. Lacroix, J. Phys. F **11** 2389 (1981).
- [254] T. A. Costi, J. Phys. C **19** 5665 (1986).
- [255] H. O. Jeschke and G. Kotliar, Phys. Rev. B **71** 085103 (2005).
- [256] B. Menge and E. Müller-Hartmann, Z. Phys. B **82** 237 (1991).
- [257] K. Yosida and K. Yamada, Prog. Theor. Phys. **46** 244 (1970).
- [258] K. Yosida and K. Yamada, Prog. Theor. Phys. **53** 1286 (1975).
- [259] V. Zlatić, B. Horvatić and D. Šokčević, Z. Phys. B **59** 151 (1985).
- [260] X. Y. Zhang, M. J. Rozenberg and G. Kotliar, Phys. Rev. Lett. **70** 1666 (1993).
- [261] D. M. Edwards and J. A. Hertz, Physica B **163** 527 (1990).
- [262] D. M. Edwards, J. Phys. Cond. Matter **5** 161 (1993).
- [263] H. Kajueter and G. Kotliar, Phys. Rev. Lett. **77** 131 (1996).
- [264] H. Kajueter and G. Kotliar, Int. J. Mod. Phys. **11** 729 (1997).
- [265] M. Potthoff, T. Wegner and W. Nolting, Phys. Rev. B **55** 16132 (1997).
- [266] M. Potthoff, T. Herrmann, T. Wegner and W. Nolting, phys. stat. sol. (b) **210** 199 (1998).
- [267] V. S. Oudovenko, K. Haule, S. Savrasov, D. Villani and G. Kotliar, Phys. Rev. B **71** 115117 (2005).
- [268] S. Y. Savrasov, V. Oudovenko, K. Haule, D. Villani and G. Kotliar, Phys. Rev. B **71** 115117 (2005).
- [269] D. E. Logan, M. P. Eastwood and M. A. Tusch, Phys. Rev. Lett. **76** 4785 (1996).
- [270] D. E. Logan, M. P. Eastwood and M. Tusch, J. Phys. Cond. Matter **9** 4211 (1997).
- [271] D. E. Logan and M. T. Glossop, J. Phys. Cond. Matter **12** 985 (2000).
- [272] N. E. Bickers and D. J. Scalapino, Ann. Phys. **193** 206 (1989).
- [273] L. Chioncel, L. Vitos, I. A. Abrikosov, J. Kollár, M. I. Katsnelson and A. I. Lichtenstein, Phys. Rev. B **67** 235106 (2003).
- [274] V. Drchal, V. Janiš and J. Kudrnovský, Phys. Rev. B **60** 15664 (1999).
- [275] V. Drchal, V. Janiš, J. Kudrnovský, V. S. Oudovenko, X. Dai, K. Haule and G. Kotliar, J. Phys. Cond. Matter **17** 61 (2005).
- [276] H. Keiter and J. C. Kimball, Phys. Rev. Lett. **25** 672 (1970).
- [277] N. E. Bickers, D. L. Cox and J. W. Wilkins, Phys. Rev. B **36** 2036 (1987).
- [278] E. Müller-Hartmann, Z. Phys. B **57** 281 (1984).
- [279] M. B. Zöhl, T. Pruschke, J. Keller, A. I. Poteryaev, I. A. Nekrasov and V. I. Anisimov, Phys. Rev. B **61** 12810 (2000).
- [280] M. B. Zöhl, I. A. Nekrasov, T. Pruschke, V. I. Anisimov and J. Keller, Phys. Rev. Lett. **87** 276403 (2001).
- [281] T. Pruschke and N. Grewe, Z. Phys. B **74** 439 (1989).
- [282] K. Haule, S. Kirchner, J. Kroha and P. Wölfle, Phys. Rev. B **64** 155111 (2001).

- [283] K. Haule, V. S. Oudovenko, S. Y. Savrasov and G. Kotliar, Phys. Rev. Lett. **94** 036401 (2005).
- [284] S. Kirchner, J. Kroha and P. Wölfle, Phys. Rev. B **70** 165102 (2004).
- [285] X. Dai, K. Haule and G. Kotliar, Phys. Rev. B **72** 045111 (2005).
- [286] J. E. Hirsch and R. M. Fye, Phys. Rev. Lett. **56** 2521 (1986).
- [287] A. N. Rubtsov and A. I. Lichtenstein, JETP Lett. **80** 61 (2004).
- [288] A. N. Rubtsov, V. V. Savkin and A. I. Lichtenstein, Phys. Rev. B **72** 035122 (2005).
- [289] P. Werner, A. Comanac, L. De Medici, M. Troyer and A. J. Millis, Phys. Rev. Lett. **97** 076405 (2006).
- [290] P. Werner and A. J. Millis, Phys. Rev. B **74** 155107 (2006).
- [291] K. Haule, Phys. Rev. B **75** 155113 (2007).
- [292] S. Sakai, R. Arita, K. Held and K. Aoki, Phys. Rev. B **74** 155102 (2006).
- [293] N. Metropolis, A. Rosenbluth, M. Rosenbluth, A. Teller and E. Teller, J. Chem. Phys. **21** 1087 (1953).
- [294] M. Suzuki, Prog. Theor. Phys. **56** 1454 (1976).
- [295] Y. Motome and M. Imada, J. Phys. Soc. Jap. **66** 1872 (1997).
- [296] S. Sakai, R. Arita and H. Aoki, Phys. Rev. B **70** 172504 (2004).
- [297] J. E. Han, Phys. Rev. B **70** 054513 (2004).
- [298] F. F. Assaad and T. C. Lang (2007), [cond-mat/0702455](#).
- [299] M. Jarrell, In *Numerical Methods for Lattice Quantum Many-Body Problems*, edited by D. J. Scalapino (Addison Wesley, Reading, 1997).
- [300] S. R. White, D. J. Scalapino, R. L. Sugar, E. Y. Loh, J. E. Gubernatis and R. T. Scalettar, Phys. Rev. B **40** 506 (1989).
- [301] F. F. Assaad and M. Imada, Phys. Rev. Lett. **74** 3868 (1995).
- [302] R. Blankenbecler, D. J. Scalapino and R. L. Sugar, Phys. Rev. D **24** 2278 (1981).
- [303] P. W. Anderson, Phys. Rev. Lett. **18** 1049 (1967).
- [304] P. W. Anderson, Phys. Rev. B **164** 352 (1967).
- [305] M. I. Katsnelson, Phys. Rev. Lett. **96** 139701 (2006).
- [306] M. Feldbacher, K. Held and F. F. Assaad, Phys. Rev. Lett. **96** 139702 (2006).
- [307] D. A. MacLean, H.-N. Ng and J. E. Greedan, J. Solid State Chem. **30** 35 (1979).
- [308] M. Eitel and J. E. Greedan, Journal of the Less-Common Metals **116** 95 (1986).
- [309] J. P. Gopel, J. E. Greedan and D. A. MacLean, J. Solid State Chem. **43** 244 (1981).
- [310] E. Pavarini, S. Biermann, A. Poteryaev, A. I. Lichtenstein, A. Georges and O. K. Andersen, Phys. Rev. Lett. **92** 176403 (2004).
- [311] E. Pavarini, A. Yamasaki, J. Nuss and O. K. Andersen, New J. Phys. **7** 188 (2005).

- [312] L. Craco, M. S. Laad, S. Leoni and E. Müller-Hartmann, Phys. Rev. B **70** 195116 (2004).
- [313] W. Heindl, T. Pruschke and J. Keller, J. Phys. – Condens. Matter **12** 2245 (2000).
- [314] S. Y. Savrasov and G. Kotliar, Phys. Rev. B **69** 245101 (2004).
- [315] X. Dai, S. Y. Savrasov, G. Kotliar, A. Migliori, H. Ledbetter and E. Abrahams, Science **300** 953 (2003).
- [316] J. Wong, M. Krisch, D. L. Farberand, F. Occelliand, A. J. Schwartzand, T.-C. Chiangand, M. Walland, C. Boro and R. Xu, Science **301** 1078 (2003).
- [317] L. V. Pourovskii, M. I. Katsnelson, A. I. Lichtenstein, L. Havela, T. Gouder, F. Wastin, A. B. Shick, V. Drchal and G. H. Lander, Europhys. Lett. **74** 479 (2006).
- [318] S. Y. Savrasov, K. Haule and G. Kotliar, Phys. Rev. Lett. **96** 036404 (2006).
- [319] L. V. Pourovskii, M. I. Katsnelson and A. I. Lichtenstein, Phys. Rev. B **73** 060506 (R) (2006).
- [320] L. V. Pourovskii, M. I. Katsnelson and A. I. Lichtenstein, Phys. Rev. B **72** 115106 (2005).
- [321] A. Shick, J. Kolorenc, L. Havela, V. Drchal and T. Gouder (2006), cond-mat/0610794.
- [322] A. K. McMahan, Phys. Rev. B **72** 115125 (2005).
- [323] B. Amadon, S. Biermann, A. Georges and F. Aryasetiawan, Phys. Rev. Lett. **96** 066402 (2006).
- [324] D. G. Koskimaki and K. A. G. Jr, In *Handbook on the Physics and Chemistry of Rare Earths*, edited by K. A. Gschneidner Jr. and L. R. Eyring (North-Holland, Amsterdam, 1978), p. 337.
- [325] U. Benedict, J. Alloys Comp. **193** 88 (1993).
- [326] W. B. Holzapfel, J. Alloys Comp. **223** 170 (1995).
- [327] A. K. McMahan, C. Huscroft, R. T. Scalettar and E. L. Pollock, J. Comput.-Aided Mater. Design **5** 131 (1998).
- [328] J. W. van der Eb, A. B. Kuz'menko and D. van der Marel, Phys. Rev. Lett. **86** 3407 (2001).
- [329] G. Eliashberg and H. Capellmann, Sov. Phys. JETP **67** 125 (1998).
- [330] A. V. Nikolaev and K. H. Michel, Eur. Phys. J. B **9** 619 (1999).
- [331] A. V. Nikolaev and K. H. Michel, Eur. Phys. J. B **17** 12 (2000).
- [332] L. Pauling, J. Am. Chem. Soc. **69** 542 (1947).
- [333] W. H. Zachariasen, unpublished (1949), Cited by A. W. Lawson and T. Y. Tang, Phys. Rev. **76**, 301 (1949).
- [334] B. Johansson, Philos. Mag. **30** 469 (1974).
- [335] B. Johansson, I. A. Abrikosov, M. Aldén, A. V. Ruban and H. L. Skriver, Phys. Rev. Lett. **74** 2335 (1995).

- [336] A. Svane, J. Trygg, B. Johansson and O. Eriksson, Phys. Rev. B **56** 7143 (1997).
- [337] A. Svane, Phys. Rev. Lett. **72** 1248 (1994).
- [338] Z. Szotek, W. M. Temmerman and H. Winter, Phys. Rev. Lett. **72** 1244 (1994).
- [339] I. S. Sandalov, O. Hjortstam, B. Johansson and O. Eriksson, Phys. Rev. B **51** 13987 (1995).
- [340] A. B. Shick, W. E. Pickett and A. I. Liechtenstein, J. Electron Spectrosc. **114** 753 (2001).
- [341] O. Eriksson, M. S. S. Brooks and B. Johansson, Phys. Rev. B **41** 7311 (1990).
- [342] P. Söderlind, Phys. Rev. B **65** 115105 (2002).
- [343] J. W. Allen and R. M. Martin, Phys. Rev. Lett. **49** 1106 (1982).
- [344] M. Lavagna, C. Lacroix and M. Cyrot, Phys. Lett. **90A** 210 (1982).
- [345] L. Z. Liu, J. W. Allen, O. Gunnarson, N. E. Christensen and O. K. Andersen, Phys. Rev. B **45** 8934 (1992).
- [346] N. Sivan and Z. Zinamon, Phys. Rev. B **37** 5535 (1988).
- [347] J. Lægsgaard and A. Svane, Phys. Rev. B **59** 3450 (1999).
- [348] K. Held, C. Huscroft, R. T. Scalettar and A. K. McMahan, Phys. Rev. Lett. **85** 373 (2000).
- [349] K. Held and R. Bulla, Eur. Phys. J. B **17** 7 (2000).
- [350] L. de' Medici, A. Georges, G. Kotliar and S. Biermann, Phys. Rev. Lett. **95** 066402 (2005).
- [351] D. M. Wieliczka, C. G. Olson and D. W. Lynch, Phys. Rev. B **29** 3028 (1984).
- [352] E. Wuilloud, H. R. Moser, W. D. Schneider and Y. Baer, Phys. Rev. B **28** 7354 (1983).
- [353] K. Held, G. Keller, V. Eyert, V. I. Anisimov and D. Vollhardt, Phys. Rev. Lett. **86** 5345 (2001).
- [354] S. V. Vonsovsky, *Magnetism*, volume 2 (John Wiley, New York, 1974).
- [355] K. N. Altmann, D. Y. Petrovykh, G. J. Mankey, N. Shannon, N. Gilman, M. Hochstrasser, R. F. Willis and F. J. Himpsel, Phys. Rev. B **61** 15661 (2000).
- [356] J. Minár, L. Chioncel, A. Perlov, H. Ebert, M. I. Katsnelson and A. I. Lichtenstein, Phys. Rev. B **72** 045125 (2005).
- [357] J. Minár, H. Ebert, C. D. Nadaï, N. B. Brookes, F. Venturini, G. Ghiringhelli, L. Chioncel, M. I. Katsnelson and A. I. Lichtenstein, Phys. Rev. Lett. **95** 166401 (2005).
- [358] A. Grechnev, I. D. Marco, M. I. Katsnelson, A. I. Lichtenstein, J. Wills and O. Eriksson (2006), `cond-mat/0610621`.
- [359] J. Bünemann, F. Gebhard, T. Ohm, R. Umstaetter, S. Weiser, W. Weber, R. Claessen, D. Ehm, A. Harasawa, A. Kakizaki, A. Kimura,

- G. Nicolay, S. Shin and V. N. Strocov, *Europhys. Lett.* **61** 667 (2003).
- [360] T. Ohm, S. Weiser, R. Umstätter, W. Weber and J. Bünemann, *J. Low Temp. Phys.* **126** 1081 (2002).
- [361] L. Chioncel and A. I. Lichtenstein (2004), [cond-mat/0403685](#).
- [362] K. Held (2002), <http://online.itp.ucsb.edu/online/cem02/held>.
- [363] L. Craco, S. Leoni and E. Müller-Hartmann, *Phys. Rev. B* **74** 155128 (2006).
- [364] G. Khaliullin and S. Maekawa, *Phys. Rev. Lett.* **85** 3950 (2000).
- [365] G. Khaliullin, *Phys. Rev. B* **64** 212405 (2001).
- [366] M. Takizawa, H. Wadati, K. Tanaka, M. Hashimoto, T. Yoshida, A. Fujimori, A. Chikamatsu, H. Kumigashira, M. Oshima, K. Shibuya, T. Mihara, T. Ohnishi, M. Lippmaa, M. Kawasaki, H. Koinuma, S. Okamoto and A. J. Millis, *Phys. Rev. Lett.* **97** 057601 (2006).
- [367] D. B. McWhan and J. P. Remeika, *Phys. Rev. B* **2** 3734 (1970).
- [368] D. B. McWhan, A. Menth, J. P. Remeika, W. F. Brinkman and T. M. Rice, *Phys. Rev. B* **7** 1920 (1973).
- [369] G. Keller, K. Held, V. Eyert, D. Vollhardt and V. I. Anisimov, *Phys. Rev. B* **70** 205116 (2004).
- [370] M. Schramme, Ph.D. thesis, Universität Augsburg (2000).
- [371] J.-H. Park, L. H. Tjeng, A. Tanaka, J. W. Allen, C. T. Chen, P. Metcalf, J. M. Honig, F. M. F. de Groot and G. A. Sawatzky, *Phys. Rev. B* **61** 11506 (2000).
- [372] S.-K. Mo, J. D. Denlinger, H.-D. Kim, J.-H. Park, J. W. Allen, A. Sekiyama, A. Yamasaki, K. Kadono, S. Suga, Y. Saitoh, T. Muro, P. Metcalf, G. Keller, K. Held, V. Eyert, V. I. Anisimov and D. Vollhardt, *Phys. Rev. Lett.* **90** 186403 (2003).
- [373] S.-K. Mo, H.-D. Kim, J. D. Denlinger, J. W. Allen, J.-H. Park, A. Sekiyama, A. Yamasaki, S. Suga, Y. Saitoh, T. Muro and P. Metcalf, *Phys. Rev. B* **74** 165101 (2006).
- [374] K. Held, J. W. Allen, V. I. Anisimov, V. Eyert, G. Keller, H.-D. Kim, S.-K. Mo and D. Vollhardt, *Physica B* **359-361** 642 (2005).
- [375] F. Lechermann, S. Biermann and A. Georges, *Phys. Rev. Lett.* **94** 166402 (2005).
- [376] O. Müller, J. P. Urbach, E. Goering, T. Weber, R. Barth, H. Schuler, M. Klemm, S. Horn and M. L. denBoer, *Phys. Rev. B* **56** 15056 (1997).
- [377] S.-K. Mo, H. S. Suga, P. Metcalf and K. Held, *Phys. Rev. Lett.* **93** 76404 (2004).
- [378] P. Limelette, A. Georges, D. Jérôme, P. Wzietek, P. Metcalf and J. M. Honig, *Science* **302** 89 (2003).
- [379] G. Kotliar, E. Lange and M. J. Rozenberg, *Phys. Rev. Lett.* **84** 5180 (2000).
- [380] M. S. Laad, L. Craco and E. Müller-Hartmann, *Phys. Rev. Lett.* **91**

- 156402 (2003).
- [381] M. S. Laad, L. Craco and E. Müller-Hartmann, *Phys. Rev. B* **73** 045109 (2006).
 - [382] A.I. Poteryaev, J.M. Tomczak, S. Biermann, A. Georges, A.I. Lichtenstein, A.N. Rubtsov, T. Saha-Dasgupta and O.K. Andersen (2007), *cond-mat/0701263*.
 - [383] G. Panaccione M. Altarelli, A. Fondacaro, A. Georges, S. Huotari, P. Lacovig, A. Lichtenstein, P. Metcalf, G. Monaco, F. Offi, L. Paolasini, A. Poteryaev, O. Tjernberg and M. Sacchi, *Phys. Rev. Lett.* **97** 116401 (2006).
 - [384] O. Parcollet, G. Biroli and G. Kotliar, *Phys. Rev. Lett.* **92** 226402 (2004).
 - [385] G. Kotliar, *Science* **302** 67 (2003).
 - [386] S. R. Hassan, A. Georges and H. R. Krishnamurthy, *Phys. Rev. Lett.* **94** 036402 (2005).
 - [387] V. Eyert, *Ann. Phys. (Leipzig)* **11** 650 (2002).
 - [388] M. S. Laad, L. Craco and E. Müller-Hartmann, *Phys. Rev. B* **73** 195120 (2006).
 - [389] T. C. Koethe, Z. Hu, M. W. Haverkort, C. Schüßler-Langeheine, F. Venturini, N. B. Brookes, O. Tjernberg, W. Reichelt, H. H. Hsieh, H.-J. Lin, C. T. Chen and L. H. Tjeng *Phys. Rev. Lett.* **97** 116402 (2006).
 - [390] A. Liebsch and A. Lichtenstein, *Phys. Rev. Lett.* **84** 1591 (2000).
 - [391] V. I. Anisimov, I. A. Nekrasov, D. E. Kondakov, T. M. Rice and M. Sigris, *Euro. Phys. J. B* **25** 191 (2002).
 - [392] Z. V. Pchelkina, I. A. Nekrasov, T. Pruschke, A. Sekiyama, S. Suga, V. I. Anisimov and D. Vollhardt (2006), *cond-mat/0601507*.
 - [393] A. Liebsch, *Europhys. Lett.* **63** 97 (2003).
 - [394] A. Liebsch, *Phys. Rev. Lett.* **91** 226401 (2003).
 - [395] A. Koga, N. Kawakami, T. M. Rice and M. Sigris, *Phys. Rev. Lett.* **92** 216402 (2004).
 - [396] A. Liebsch, *Phys. Rev. B* **70** 165103 (2005).
 - [397] A. Koga, K. Inaba and N. Kawakami, *Prog. Theo. Phys. Suppl.* **160** 253 (2005).
 - [398] A. Koga, N. Kawakami, T. M. Rice and M. Sigris, *Phys. Rev. B* **72** 045128 (2005).
 - [399] K. Inaba, A. Koga, S. I. Suga and N. Kawakami, *J. Phys. Soc. Jap.* **74** 2393 (2005).
 - [400] K. Inaba, A. Koga, S. I. Suga and N. Kawakami, *Phys. Rev. B* **72** 085112 (2005).
 - [401] S. Biermann, L. de' Medici and A. Georges, *Phys. Rev. Lett.* **95** 206401 (2005).
 - [402] L. de' Medici, A. Georges and S. Biermann, *Phys. Rev. B* **72** 205124

- (2005).
- [403] R. Arita and K. Held, Phys. Rev. B **72** 201102(R) (2005).
- [404] C. Knecht, N. Blümer and P. G. J. van Dongen, Phys. Rev. B **72** 081103 (R) (2005).
- [405] A. Liebsch, Phys. Rev. Lett. **95** 116402 (2005).
- [406] P. G. J. van Dongen, C. Knecht and N. Blümer, Phys. Stat. Sol. B **243** 116 (2006).
- [407] M. Ferrero, F. Becca, M. Fabrizio and M. Capone, Phys. Rev. B **72** 205126 (2005).
- [408] A. Liebsch and T. A. Costi (2006), `cond-mat/0603548`.
- [409] N. Blümer, C. Knecht, K. Pozgajcic and P. van Dongen (2006), `cond-mat/0609758`.
- [410] A. Liebsch (2006), `cond-mat/0610482`.
- [411] T. Pruschke and R. Bulla, Eur. Phys. J. B **44** 217 (2005).
- [412] X. Dai, G. Kotliar and Z. Fang (2006), `cond-mat/0611075`.
- [413] A. Fujimori, I. Hase, H. Namatame, Y. Fujishima, Y. Tokura, H. Eisaki, S. Uchida, K. Takegahara and F. M. F. de Groot, Phys. Rev. Lett. **69** 1796 (1992).
- [414] Y. Aiura, F. Iga, Y. Nishihara, H. Ohnuki and H. Kato, Phys. Rev. B **47** 6732 (1993).
- [415] I. H. Inoue, I. Hase, Y. Aiura, A. Fujimori, Y. Haruyama, T. Maruyama and T. Nishihara, Phys. Rev. Lett. **74** 2539 (1995).
- [416] I. H. Inoue, O. Goto, H. Makino, N. E. Hussey and M. Ishikawa, Phys. Rev. B **58** 4372 (1998).
- [417] K. Morikawa, T. Mizokawa, K. Kobayashi, A. Fujimori, H. Eisaki, S. Uchida, F. Iga and Y. Nishihara, Phys. Rev. B **52** 13711 (1995).
- [418] M. J. Rozenberg, I. H. Inoue, H. Makino, F. Iga and Y. Nishihara, Phys. Rev. Lett. **76** 4781 (1996).
- [419] I. A. Nekrasov, G. Keller, D. E. Kondakov, A. V. Kozhevnikov, T. Pruschke, K. Held, D. Vollhardt and V. I. Anisimov, Phys. Rev. B **72** 155106 (2005).
- [420] I. A. Nekrasov, K. Held, G. Keller, D. E. Kondakov, T. Pruschke, M. Kollar, O. K. Andersen, V. I. Anisimov and D. Vollhardt, Phys. Rev. B **73** 155112 (2006).
- [421] K. Maiti, D. D. Sarma, M. J. Rozenberg, H. M. I. H. Inoue, O. Goto, M. Pedio and R. Cimino, Europhys. Lett. **55** 246 (2001).
- [422] A. Sekiyama, H. Fujiwara, S. Imada, H. Eisaki, S. I. Uchida, K. Takegahara, H. Harima, Y. Saitoh and S. Suga (2002), `cond-mat/0206471`.
- [423] I. A. Nekrasov, G. Keller, D. E. Kondakov, A. V. Kozhevnikov, T. Pruschke, K. Held, D. Vollhardt and V. I. Anisimov (2002), `cond-mat/0211508`.
- [424] A. Liebsch, Phys. Rev. Lett. **90** 096401 (2003).

- [425] H. Ishida, D. Wortmann and A. Liebsch, Phys. Rev. B **73** 245421 (2006).
- [426] A. Lanzara, P. V. Bogdanov, S. A. K. X. J. Zhou, D. L. Feng, E. D. Lu, T. Yoshida, H. Eisaki, A. Fujimori, K. Kishio, J.-I. Shimoyama, T. Noda, S. U. Z. Hussain and Z.-X. Shen, Nature **421** 510 (2001).
- [427] T. Yoshida, K. Tanaka, H. Yagi, A. Ino, H. Eisaki, A. Fujimori and Z.-X. Shen, Phys. Rev. Lett. **95** 146404 (2005).
- [428] K. Byczuk, M. Kollar, K. Held, Y.-F. Yang, I. A. Nekrasov, T. Pruschke and D. Vollhardt, Nature Physics **3** 168 (2007).
- [429] K. Takada, H. Sakurai, E. Takayama-Muromachi, F. Izumi, R. A. Dillanian and T. Sasaki, Nature **422** 53 (2003).
- [430] W. Koshibae and S. Maekawa, Phys. Rev. Lett. **91** 257003 (2003).
- [431] D. J. Singh, Phys. Rev. B **61** 13397 (2000).
- [432] C. A. Marianetti, G. Kotliar and G. Ceder, Phys. Rev. Lett. **92** 196405 (2004).
- [433] M. D. Johannes and D. J. Singh, Phys. Rev. B **70** 14507 (2004).
- [434] R. Arita, Phys. Rev. B **71** 132503 (2005).
- [435] F. Lechermann, S. Biermann and A. Georges, Prog. Theor. Phys. Supp. **160** 233 (2005).
- [436] P. Zhang, W. Luo, M. L. Cohen and S. G. Louie, Phys. Rev. Lett. **93** 236402 (2004).
- [437] H. Ishida, M. D. Johannes and A. Liebsch, Phys. Rev. Lett. **94** 196401 (2005).
- [438] C. A. Perroni, H. Ishida and A. Liebsch (2006), [cond-mat/0609702](#).
- [439] J. Merino, B. J. Powell and R. H. McKenzie, Phys. Rev. B **73** 235107 (2006).
- [440] C. A. Marianetti, K. Haule and O. Parcollet (2006), [cond-mat/0612606](#).
- [441] C. A. Marianetti and G. Kotliar (2006), [cond-mat/0605177](#).
- [442] I. A. Nekrasov, Z. V. Pchelkina, G. Keller, T. Pruschke, K. Held, A. Krimmel, D. Vollhardt and V. I. Anisimov, Phys. Rev. B **67** 085111 (2003).
- [443] V. I. Anisimov, M. A. Korotin, M. Zöfl, T. Pruschke, K. L. Hur and T. M. Rice, Phys. Rev. Lett. **83** 364 (1999).
- [444] M. S. Laad, L. Craco and E. Müller-Hartmann, Phys. Rev. B **67** 033105 (2003).
- [445] C. Lacroix, Can. J. Phys. **79** 1469 (2001).
- [446] N. Shannon, Eur. Phys. J. B **27** 527 (2001).
- [447] P. Fulde, A.N. Yaresko, A.A. Zvyagin and Y. Grin, Europhys. Lett. **54** 779 (2001).
- [448] S. Burdin, D. R. Grempel, and A. Georges, Phys. Rev. B **66** 045111 (2002).
- [449] J. Hopkinson and P. Coleman, Phys. Rev. Lett. **89** 267201 (2002).
- [450] S. Fujimoto, Phys. Rev. B **65** 155108 (2002).

- [451] H. Tsunetsugu, J. Phys. Soc. Jpn **71** 1845 (2002).
- [452] Y. Yamashita and K. Ueda, Phys. Rev. B **67** 195107 (2003).
- [453] R. Arita, K. Held, A. V. Lukoyanov, V. I. Anisimov, Phys. Rev. Lett. **98** 166402 (2007).
- [454] A. Shimoyamada, S. Tsuda, K. Ishizaka, T. Kiss, T. Shimojima, T. Togashi, S. Watanabe, C. Q. Zhang, C. T. Chen, Y. Matsushita, H. Ueda, Y. Ueda and S. Shin, Phys. Rev. Lett. **96** 026403 (2006).
- [455] R. von Helmolt, J. Wecker, B. Holzapfel, L. Schultz and K. Samwer, Phys. Rev. Lett. **71** 2331 (1993).
- [456] S. Jin, T. H. Tiefel, M. McCormack, R. A. Fastnacht, R. Ramesh and L. H. Chen, Science **264** 413 (1994).
- [457] M. Rozenberg, Eur. Phys. J. B **2** 457 (1998).
- [458] P. Benedetti and R. Zeyher, Phys. Rev. B **59** 9923 (1999).
- [459] K. Held and D. Vollhardt, Phys. Rev. Lett. **84** 5168 (2000).
- [460] T. Pruschke and M. B. Zöfl, Adv. in Solid State Phys. **40** 251 (2001).
- [461] M. S. Laad, L. Craco and E. Müller-Hartmann, New J. Phys. **6** 157 (2004).
- [462] T. V. Ramakrishnan, H. R. Krishnamurthy, S. R. Hassan and G. Venkateswara Pai, Phys. Rev. Lett. **92** 157203 (2004).
- [463] A. Yamasaki, M. Feldbacher, Y.-F. Yang, O. K. Andersen and K. Held, Phys. Rev. Lett. **96** 166401 (2006).
- [464] Y.-F. Yang and K. Held (2006), `cond-mat/0603553`.
- [465] I. Loa, P. Adler, A. Grzechnik, K. Syassen, U. Schwarz, M. Hanfland, G. K. Rozenberg, P. Gorodetsky and M. P. Pasternak, Phys. Rev. Lett. **87** 125501 (2001).
- [466] A. E. Bocquet, T. Mizokawa, T. Saitoh, H. Namatame and A. Fujimori, Phys. Rev. B **46** 3771 (1992).
- [467] A. Chainani, M. Mathew and D. D. Sarma, Phys. Rev. B **47** 15397 (1993).
- [468] J.-H. Park, C.-T. Chen, S.-W. Cheong, W. Bao, G. Meigs, V. Chakarian and Y. U. Idzerda, Phys. Rev. Lett. **76** 4215 (1996).
- [469] T. Saitoh, A. Sekiyama, K. Kobayashi, T. Mizokawa, A. Fujimori, D. D. Sarma, Y. Takeda and M. Takano, Phys. Rev. B **56** 8836 (1997).
- [470] Y. Okimoto, T. Katsufuji, T. Ishikawa, A. Urushibara, T. Arima and Y. Tokura, Phys. Rev. Lett. **75** 109 (1995).
- [471] M. Quijada, J. Černe and J. R. Simpson, H. D. Drew, K. H. Ahn, A. J. Millis, R. Shreekala, R. Ramesh, M. Rajeswari and T. Venkatesan, Phys. Rev. B **58** 16093 (1998).
- [472] J. H. Jung, K. H. Kim, T. W. Noh, E. J. Choi and J. Yu, Phys. Rev. B **57** 11043 (1998).
- [473] K. Takenaka, K. Iida, Y. Sawaki, S. Sugai, Y. Moritomo and A. Nakamura, J. Phys. Soc. Jap. **68** 1828 (1999).

- [474] N. N. Kovaleva, A. V. Boris, C. Bernhard, A. Kulakov, A. Pimenov, A. M. Balbashov, G. Khaliullin and B. Keimer, Phys. Rev. Lett. **93** 147204 (2004).
- [475] L. Craco, M. S. Laad and E. Müller-Hartmann, Phys. Rev. Lett. **90** 237203 (2003).
- [476] M. S. Laad, L. Craco and E. Müller-Hartmann, Phys. Rev. B **64** 214421 (2003).
- [477] R. Arita, A. Yamasaki, K. Held, J. Matsuno and K. Kuroki (2006), `cond-mat/0611698`.
- [478] S. Y. Savrasov and G. Kotliar, Phys. Rev. Lett. **90** 056401 (2003).
- [479] X. Ren, I. Leonov, G. Keller, M. Kollar, I. A. Nekrasov and D. Vollhardt, Phys. Rev. B **74** 195114 (2006).
- [480] J. Kunes, V. I. Anisimov, A. V. Lukoyanov and D. Vollhardt), `cond-mat/0612116`.
- [481] X. Wan, Q. Yin and S. Y. Savrasov (2006), `cond-mat/0609006`.
- [482] T. Saha-Dasgupta, A. I. Lichtenstein and R. Valenti, Phys. Rev. B **71** 153108 (2005).
- [483] L. Craco, M. S. Laad and E. Müller-Hartmann (2004), `cond-mat/0410472`.
- [484] L. Craco, C. I. Ventura, A. N. Yaresko and E. Müller-Hartmann, Phys. Rev. B **73** 094432 (2006).
- [485] E. M.-H. L. Craco, M. S. Laad, Phys. Rev. B **74** 064425 (2006).
- [486] S. A. Wolf, D. D. Awschalom, R. A. Buhrman, J. M. Daughton, S. von Molnár, M. L. Roukes, A. Y. Chtchelkanova and D. M. Treger, Science **294** 1488 (2001).
- [487] I. Žutić, J. Fabian and S. das Sama, Rev. Mod. Phys. **76** 323 (2004).
- [488] D. M. Edwards and J. A. Hertz, Physica F **3** 2191 (1973).
- [489] V. Y. Irkhin and M. I. Katsnelson, Sov. Phys. Solid State **25** 1947 (1994).
- [490] V. Y. Irkhin, M. I. Katsnelson and A. I. Lichtenstein, Proceedings of Berlin/Wandlitz Workshop 2004 (2004), [`cond-mat/0406487`].
- [491] L. Chioncel, M. I. Katsnelson, R. A. de Groot and A. I. Lichtenstein, Phys. Rev. B **68** 144425 (2003).
- [492] S. Chadov, J. Minar, H. Ebert, A. Perlov, L. Chioncel, M. I. Katsnelson and A. I. Lichtenstein, Phys. Rev. B **74** 140411 (R) (2006).
- [493] L. Chioncel, E. Arrigoni, M. I. Katsnelson and A. I. Lichtenstein, Phys. Rev. Lett. **96** 137203 (2006).
- [494] L. Craco, M. S. Laad and E. Müller-Hartmann, Phys. Rev. B **68** 233310 (2003).
- [495] K. Aryanpour, J. Moreno, M. Jarrell and R. S. Fishman, Phys. Rev. B **72** 045343 (2005).
- [496] L. Chioncel, P. Mavropoulos, M. Lezaić, S. Blügel, E. Arrigoni, M. I.

REFERENCES

123

- Katsnelson and A. I. Lichtenstein, Phys. Rev. Lett. **96** 197203 (2006).
- [497] L. Chioncel, M. I. Katsnelson, G. A. de Wijs, R. A. de Groot and A. I. Lichtenstein, Phys. Rev. B **71** 085111 (2005).
- [498] A. Yamasaki, L. Chioncel, A. I. Lichtenstein and O. K. Andersen, Phys. Rev. B **74** 024419 (2006).
- [499] L. Chioncel, Allmaier, A. Yamasaki, M. Daghofer, E. Arrigoni, M. I. Katsnelson and A. I. Lichtenstein (2006), `cond-mat/0609060`.
- [500] K. Tanigaki, T. W. Ebbesen, S. Saito, J. Mizuki, J. S. Tsai, Y. Kubo and S. Kuroshima, Nature **352** 222 (1991).
- [501] M. Capone, M. Fabrizio, P. Giannozzi and E. Tosatti, Phys. Rev. B **62** 7619 (2000).
- [502] T. Yildirim, L. Barbedette, J. E. Fischer, C. L. Lin, J. Robert, P. Petit and T. T. M. Palstra, Phys. Rev. Lett. **77** 167 (1996).
- [503] R. Arita, T. Miyake, T. Kotani, M. van Schilfgaarde, T. Oka, K. Kuroki, Y. Nozue and H. Aoki, Phys. Rev. B **69** 195106 (2004).
- [504] T. Nakano, Y. Ikemoto and Y. Nozue, Eur. Phys. J. D **9** 505 (1999).
- [505] T. Nakano, Y. Ikemoto and Y. Nozue, Physica B **281-282** 688 (2000).